8-2017

Battery Energy Storage Emulation for Power System Applications

Jessica Danielle Boles
University of Tennessee, Knoxville, jboles@vols.utk.edu

To the Graduate Council:

I am submitting herewith a thesis written by Jessica Danielle Boles entitled "Battery Energy Storage Emulation for Power System Applications." I have examined the final electronic copy of this thesis for form and content and recommend that it be accepted in partial fulfillment of the requirements for the degree of Master of Science, with a major in Electrical Engineering.

Leon Tolbert, Major Professor

We have read this thesis and recommend its acceptance:

Fred Wang, Kevin Tomsovic, Daniel Costinett

Accepted for the Council:
Dixie L. Thompson

Vice Provost and Dean of the Graduate School

(Original signatures are on file with official student records.)

Battery Energy Storage Emulation for Power System Applications

A Thesis Presented for the

Master of Science

Degree

The University of Tennessee, Knoxville

Jessica Danielle Boles

August 2017

To Dad, Mom, Ashlee, and Alex. Thank you for your endless love and support.

Acknowledgements

First, I want to acknowledge my major professor and advisor for the past six years, Dr. Leon Tolbert. I sincerely appreciate your mentorship, instruction, and the many opportunities you have opened for me throughout my undergraduate and graduate education. I also want to express gratitude for my other committee members, Dr. Fred Wang, Dr. Daniel Costinett, and Dr. Kevin Tomsovic, as well as Dr. Burak Ozpineci at Oak Ridge National Laboratory, for guiding me throughout this work and other research pursuits. Thank you all for investing in me, challenging me, and encouraging me as a young power electronics student.

"If the result of today is that I get to work on a different problem tomorrow, I am making progress."

Abstract

The concept of energy storage for power systems has received increasingly more attention in recent decades, and the growing penetration of renewable energy sources has only escalated demand for it. Energy storage systems are excellent for balancing generation and load, for suppressing power fluctuations, and for providing other ancillary services to the grid. The Hardware Testbed (HTB) is a novel converter-based grid emulator created for studying the needs associated with high renewable penetration, but the system currently lacks a battery storage emulator. Thus, this work documents the development of a battery energy storage system (BESS) emulator for the HTB.

The BESS emulator includes internal battery models for Lithium Ion, Lead Acid, and Vanadium redox flow battery technologies. The emulated BESS contains a two-stage power electronics interface using a DC-DC converter and a boost rectifier separated by a DC link. Controllers for active power output, reactive power output, and DC link voltage are designed for the power electronics interface, and application-specific control loops for primary frequency regulation, inertia emulation, and voltage support are also added. The models and control for this emulated BESS are implemented on a digital signal processor that controls one voltage source inverter on the HTB as if it were the BESS's boost rectifier. Consequently, the voltage source inverter mimics the behavior of a BESS at its point of common coupling with the HTB's power system.

The BESS emulator is simulated and then tested experimentally on the HTB, and all of its control functions demonstrate correct operation. The BESS emulator's primary frequency regulation and inertia emulation functions nearly eliminate the system frequency swing following a step change in load, and the voltage support keeps the BESS terminal voltage at a safer

level following the disturbances. These three support functions are concluded to be capable of simultaneous operation, which allows the BESS emulator to support the HTB's power system in multiple ways at the same time. In the future, the BESS emulator can be used on the HTB to study how battery storage can be used to support renewables and other dynamic power system needs.

Table of Contents

Nomenclature

A	Battery exponential zone amplitude (V)
a	Curve-fitting coefficient
B	Battery exponential zone time constant (1/Ah)
C	Capacitance (F)
c	Concentration of active species in electrolyte (mol/L)
C_1	R-C pair capacitance (F)
C_b	Half-bridge converter capacitance (F)
C_{dc}	DC link capacitance (F)
d	DC-DC converter duty cycle
d_{abc}	Vector of three-phase duty cycles, d_a, d_b, and d_c
d_{dq}	Vector of three-phase direct and quadrature duty cycles, d_d and d_q
E_0	Standard electrode potential (V)
E_{ocv}	Open-circuit potential (V)
$Exp(t)$	Exponential zone potential (V)
F	Faraday constant (96487 C/mol)

f	Power system frequency (Hz)
G	Gas constant (8.314 J/(mol°K))
i_L	Inductor current (A)
i_{abc}	Vector of three-phase currents, i_a, i_b, and i_c (A)
i_{batt}	Battery terminal current (A)
i_{dc1}	DC link current before capacitance (A)
i_{dc2}	DC link current after capacitance (A)
i_{dc}	DC current (A)
i_{diff}	Diffusion current (A)
i_{dq}	Vector of three-phase direct and quadrature currents, i_d and i_q (A)
i_{int}	Internal cell current not considering diffusion (A)
i_{shunt}	Shunt current (A)
J	Battery capacity (Ah)
K	Battery polarization constant (Ω or V/Ah)
L	Inductance (H)
L_0	Series inductance (H)
L_b	Half-bridge converter inductance (H)
L_f	Filter inductance (H)
M	DC-DC converter modulation index
P	Active power output (W)

P_f	Active power output between AC-DC converter and output filter (W)
Q	Reactive power output (VAR)
R	Resistance (Ω)
R_0	Series resistance (Ω)
R_1	R-C pair resistance (Ω)
s	Boolean variable where 0 denotes low-side switch on and 1 denotes high-side switch on
s_{abc}	Vector of boolean variables s_a, s_b, and s_c where 0 denotes low-side switch on and 1 denotes high-side switch on
S_{rating}	Apparent power rating of BESS converter interface (VA)
SOC_{cell}	Apparent cell SOC (%)
SOC_{tank}	SOC of electrolyte tank (%)
T	Temperature (°C or °K)
T_s	Sampling period (s)
U	Electrolyte flow rate (L/min)
$u(t)$	Boolean variable where 0 denotes discharging and 1 denotes charging
v_1	Voltage across R-C pair (V)
v_n	Three-phase neutral point voltage (V)
v_{batt}	Battery terminal voltage (V)
v_C	Capacitor voltage (V)
v_{dc}	DC link voltage (V)

$v_{f(abc)}$	Vector of three-phase voltages between AC-DC converter and output filter, v_{fa}, v_{fb}, and v_{fc} (V)
$v_{t(abc)}$	Vector of three-phase voltages at BESS terminal, v_{ta}, v_{tb}, and v_{tc} (V)
$v_{t(rms)}$	RMS value of BESS terminal voltage (V)
W	Electrolyte tank volume (L)
x	DSP control cycle number
Y	Transformation matrix from *abc* to *dq* coordinates
Z	Impedance (Ω)
$\int idt$	Total charge discharged from battery (C)
η_{diff}	Self-discharge loss (%)
ω	Power system frequency (rad/s)
τ	Filter time constant (s)
$\bar{}$	Denotes the average value of a variable
Δ	Denotes the error of a variable
*	Denotes the reference value for a variable
^{T}	Denotes the transform of a matrix
$_{LPF}$	Denotes the value of a variable after it passes through a low-pass filter

Chapter 1

Introduction and Background

Renewable energy technologies have gained significant traction in recent years due to environmental and sustainability concerns on a global scale. By the end of 2016, the average levelized cost of electricity for some non-hydro technologies such as wind and solar had reached grid parity in approximately 30 countries, even without subsidies [1]. Traditionally, coal and nuclear generators are scheduled to cover the base load during generation planning, and natural gas combustion turbines are used to cover seasonal peaks and follow load fluctuations throughout the day. If these are replaced by inverter-based resources such as wind and solar, flexible energy capacity is needed for meeting peak demand and compensating for fluctuations [2].

Generation and load are typically balanced using technologies such as fast-ramping gas or diesel plants, energy storage, interconnection with other regions, and demand response [3]. The grid can absorb fluctuations for renewable penetration up to 10%, but continuing to increase these variable, non-dispatchable sources makes balancing generation and load more challenging. To accommodate more renewables, the grid can be strengthened through upgrades, expansion, increased traditional dispatchable power, more precise demand-side management, and energy storage [4]. Energy storage effectively decouples generation and load by shifting power delivery across time, which is excellent for managing fluctuations. Implementing storage can improve the operating capabilities of the grid, lower energy costs, increase generation efficiency, increase grid reliability, and defer and/or reduce infrastructure investments [3, 5, 6, 7].

Increased penetration levels of renewables, the dropping cost of solar, regulations that value frequency response, and increasing electricity retail rates are all expected to be drivers for energy storage in the near future [8]. Increased wind penetration will put downward pressure on already-low prices during off-peak times of the day, which presents a major opportunity for arbitrage. Higher solar penetration on distribution systems will require reactive power support and short-term load variation at the local level. The challenges associated with integrating renewables is predicted to increase nonlinearly after 20% penetration is reached [9].

1.1 Energy Storage for Grid Applications

1.1.1 Applications

Energy storage applications can be categorized according to bulk energy management, power balancing, and power quality and reliability. Eleven applications are arranged in Table 1.1 according to these categories, and they are described in detail below.

Energy Arbitrage

Arbitrage involves purchasing energy during off-peak periods when prices are low and storing it so that it can be used or sold during peak times. Peak shaving, which refers to smoothing out the daily peak demand, falls into this category, as does time-shift on larger scales such as seasonal and diurnal energy storage. Arbitrage also includes storage of excess energy for use when needed later, which is commonly used with renewables [10]. Energy storage used for arbitrage must be

Table 1.1: Energy Storage Applications for Power Systems

Bulk Energy Management	Power Balancing	Power Quality/Reliability
Energy Arbitrage	Renewable Smoothing	Power Quality
Generation Upgrade Deferral	Load Following	Voltage Support
T&D Upgrade Deferral	Frequency Regulation	UPS
	Inertia Emulation	
	Reserves	

able to support long term charge/discharge cycles with large capacity and very little self-discharge [4, 8]. Since this application relies on the monetary benefit of time-shifting energy, its value is very sensitive to operating costs and efficiency [10].

Capacity Upgrade Deferral and Congestion Relief

Energy storage can be used to defer or delay the need to add generation, transmission, or distribution capacity to a power system by time-shifting energy so that existing capacity requirements are met. The highest loads only occur for a few hours or days per year, which storage can easily support without needing to be cycled very often. This improves asset utilization and can also extend system lifetime by reducing stress on generation, transmission, and distribution [4, 10].

Congestion can occur in transmission systems when demand outgrows transmission capacity and available energy cannot be transmitted to loads that need it. This can lead to the implementation of transmission access charges, congestion charges, or local marginal pricing. Eventually, it often becomes more economical to install energy storage electrically "downstream" from the congested line so it can store energy when there is no congestion and release it during peak demands [10].

Generation and line upgrades are designed to account for 15-20 year growth projections, so part of each investment is unused for most of its lifetime. Delaying upgrades by installing energy storage allows more time for evaluating growth projections and helps to minimize the risk that expected growth does not occur. The return on investment for storage used to defer upgrades can be realized more quickly if the system can be moved from place to place, which is most feasible for distribution-level storage. Storage for deferring capacity upgrades or relieving congestion can also be used for a variety of other applications when existing systems are not at capacity [10].

Renewable Smoothing and Load Following

Non-hydroelectric renewable sources like wind and solar photovoltaic (PV) have natural power fluctuations that can change every several minutes [10]. A large cloud can cause PV power output to fall by up to 90%, which becomes a serious issue as PV penetration levels rise. These short-term

fluctuations require smoothing, which can be accomplished by storage at the generation site before the power is exported to the grid [8, 10]. This requires a storage type with fast response time so that the variations can be closely traced [4].

Load following is similar to renewable smoothing in terms of tracing a fluctuating profile, but load following is conducted for load variation instead of generation. It can be controlled in response to system frequency, timeline loading, or how those relate to each other as necessary to match the scheduled frequency or scheduled interchange with different areas. Generators can conduct load following by increasing or decreasing output, but this requires them to operate at partial load. Operating at partial load necessitates more fuel per MWh generated, which decreases the generator's efficiency, and varying generator output results in more frequent maintenance needs. Thus, since many energy storage types can operate well at partial power and can respond very quickly, storage is an excellent alternative for load following. Also, storage systems used for load following can be used for other applications at the same time if charging and discharging are coordinated [10].

Reserves and Black Start

Reserves are kept in power systems for cases in which generation units are lost. They are typically at least the size of the largest generation unit or 15-20% of the supply capacity. There are three types of reserves: spinning, non-spinning, and supplemental. Spinning reserves are synchronized but not loaded, and they must respond within 10 minutes of an outage. Non-spinning reserves are not synchronized and may be offline or just a section of interruptible loads, but they must also respond within 10 minutes. Supplemental reserves serve as back-up to both of these and must respond to a disturbance within one hour if needed [10].

If generating units are used for reserve purposes, they must be online and at partial load so that they are ready to respond at any time. Energy storage can also serve as reserve, and it does not need to be charging or discharging in order to be ready. After major failures, energy storage can be also used to energize lines and to provide stations with power for black starts and restoring the system [10].

Frequency Regulation

The frequency of a power system deviates from its nominal value when there is an imbalance between generation and load [11, 12]. Frequency regulation compensates for short-lived differences between the two so that the frequency stays at its nominal or scheduled value [11]. Synchronous generators can provide regulating services by varying power output, but this causes them to degrade more quickly and incurs higher maintenance costs. Energy storage can provide more freedom for regulation since it is bidirectional and can offer its whole positive and negative capacity for the service [8, 10]. Also, several storage technologies have faster response times than conventional power plants, and fast response is crucial for effective regulation. Energy storage to be used for frequency regulation must have at least minute-duration storage capacity and should be capable of frequent but short charge/discharge cycles [4, 8].

Primary frequency control is the first reaction to system frequency changes and begins within seconds of a disturbance, as shown in Fig. 1.1. Its purpose is to momentarily stabilize the frequency by filling the discrepancy between generation and load, but it does not return the frequency to its nominal value [8, 11, 13]. It reacts in shorter time periods to system needs than other levels of frequency regulation, which is particularly important for sudden loss of generation or transmission lines. Primary frequency control is usually conducted by a synchronous generator's governor, which adjusts the mechanical energy input into the generator shaft as necessary. It can also be conducted by interrupting predefined loads or by using energy storage to compensate for a power imbalance [8, 10, 11]. Primary frequency control capabilities in the Eastern Interconnect as a whole have decreased in the past three decades, which is detrimental for maintaining system stability after frequency disturbances [11].

Secondary frequency control is the second reaction to a frequency disturbance and usually begins within a minute of the event. It is specifically responsible for returning the frequency back to its scheduled value after the primary frequency control has stabilized it. Secondary frequency control is usually conducted by automatic generation control (AGC) [10, 11, 13], using power resources available in reserves when necessary [11]. Tertiary control is the final action taken after a disturbance and must be manually activated around fifteen minutes after the event [13]. It involves

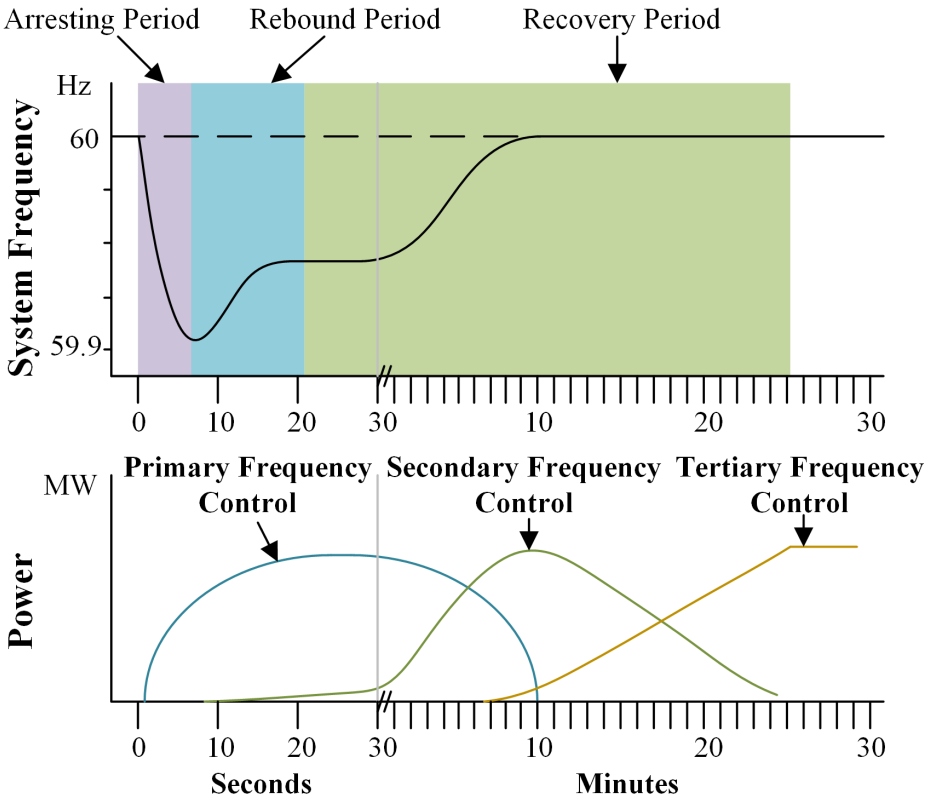

Figure 1.1: Frequency regulation following a disturbance [5, 10].

rearranging resources to handle the current and potential future situations, which may require deploying and restoring reserves [11]. These three levels of frequency regulation are visualized in Fig. 1.1 [5, 10].

Inertia Emulation

The rate at which frequency changes in a power system as a result of power imbalance is directly proportional to the system's aggregate inertia [10, 14]. Inertia is determined by rotating masses in the system such as synchronous generators, and high amounts of inertia slow the rate of change of frequency during a disturbance [8]. Rotational speed and electrical frequency are closely coupled for synchronous generators, so slowing the rate of change of frequency is accomplished through their absorption and release of kinetic energy [14].

Renewable sources such as wind and PV are tied to power systems with converters, which decouple generator motion from grid frequency. Because of this, they contribute little or no inertia to the system, so replacing traditional generation with renewables leads to lower system-wide inertial response [14, 15]. However, converter interfaces can be controlled to mimic inertial response and other synchronous generator characteristics. The necessary power reserve for this can be added with energy storage or virtually added by partially unloading renewable sources [14].

Energy storage can be controlled to quickly charge or discharge in reaction to sudden changes in frequency, which slows the subsequent change in frequency and therefore emulates inertia in the system. The location of the storage with respect to generation, transmission and loads in the system is key for its effectiveness, but systems greater than 20 MW are capable of providing synthetic inertia twice as effectively as conventional fossil fuel generators [10]. Inertia emulation requires storage types with fast reaction times and the ability to discharge high amounts of power in short periods of time [8].

Voltage Support

In power systems, voltage levels fluctuate with power transfer and line impedance but must be kept within specified limits [16]. If more power is generated than consumed on a feeder, for example, power flow reverses and causes the voltage at the end of the feeder to rise substantially [17]. This necessitates the management of system reactance, which is done by injecting and absorbing reactive power as needed. Power plants can be used to inject and absorb reactive power, but strategically-placed compensators or assets with reactive power support capability can be more effective [10].

Voltage disturbances are categorized according to magnitude and duration. A voltage sag is defined as an root-mean-squared (rms) voltage drop to between 0.1 and 0.9 per unit (pu) for up to one minute, and a voltage swell is a voltage rise to more than 1.1 pu for up to one minute. A voltage sag that lasts longer than one minute is then considered undervoltage, and a voltage swell lasting longer than one minute is known as overvoltage. Problems with voltage can be either man-made or

due to natural causes [18, 19]. Motor loads, control instrumentation, data-processing equipment, and lighting loads are particularly sensitive to voltage sags [19].

AC-DC converters in power conditioning systems are limited by their apparent power ratings [20], so capacity that is not used for active power can be used for injecting and absorbing reactive power [21]. This requires the power conditioning system for the storage to operate at a non-unity power factor but can be excellent for providing voltage support [10].

Power Quality and Reliability

Energy storage can be used to protect loads from poor power quality. Examples of power quality issues include voltage magnitude variation, primary frequency (60 Hz) variation, harmonics, low power factor, and short interruptions. To improve power quality, the energy storage discharges to smooth power quality problems so that the load remains unaffected [10].

Energy storage can also be used for reliability purposes, which involves supporting individual loads during utility power disruptions. Storage systems and loads can be designed to detach from the larger power system during outages and then re-synchronize when power is restored. Storage can also be used as uninterruptible power supply (UPS) systems to protect sensitive loads like industrial processes, data centers, and health care facilities [4, 10].

1.1.2 Technologies

Energy storage technologies can be classified into five categories: mechanical, electrochemical, electric, chemical, and thermal. Mechanical, electrochemical, and electric technologies store energy in an intermediary form and then convert it back to electricity for release. Thermal and chemical storage technologies release energy in other forms such as heat or fuel, so they are not discussed in this work [4]. The most well-known types of mechanical, electrochemical, and electrical energy storage technologies for grid applications are described in detail below and displayed in Fig. 1.2 according to their typical power ratings and discharge durations.

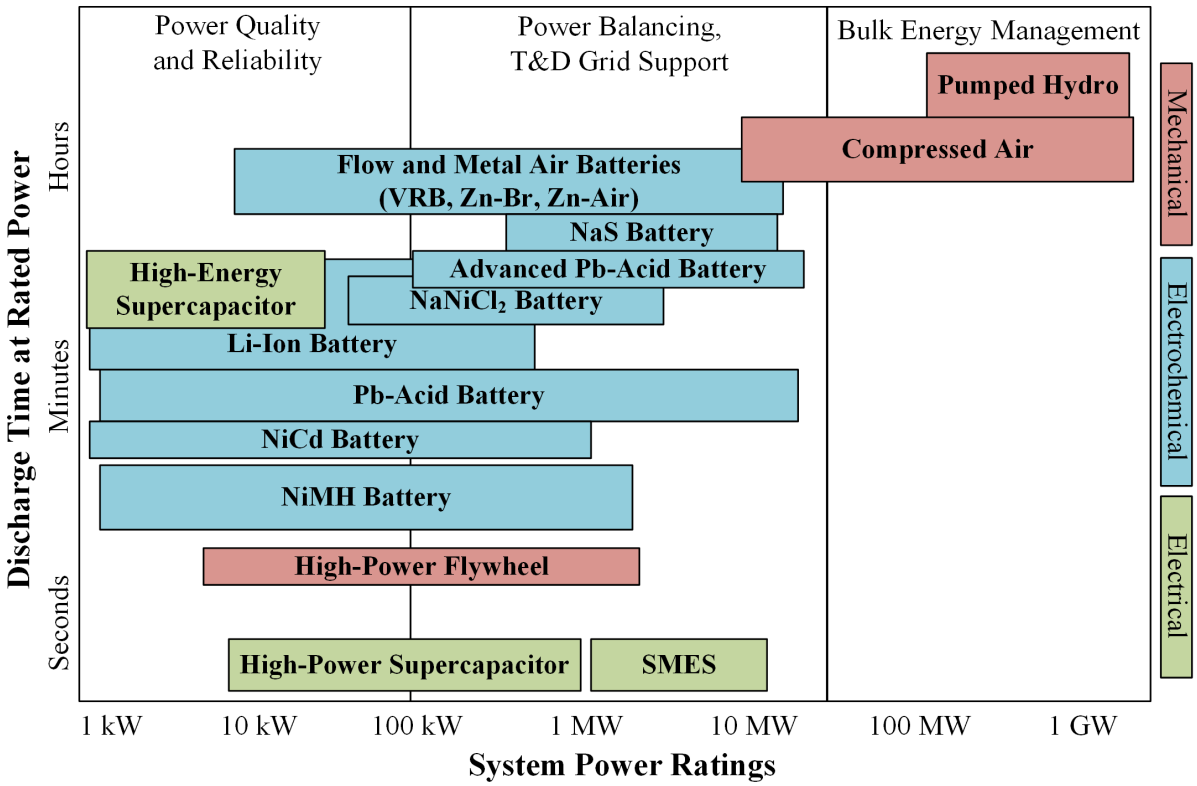

Figure 1.2: Discharge time vs. power rating of energy storage technologies [6, 9, 22, 23, 24, 25].

Pumped Hydroelectric Energy Storage

The first pumped hydroelectric energy storage (PHES) plants were built in the 1920s [10], and now almost 95% of energy storage capacity in the United States is PHES [22]. PHES is the least energy-dense storage technology, but low costs and low losses have propelled its widespread implementation for large-scale grid applications [24].

PHES requires two reservoirs of significant height difference with pipes and turbomachinery connecting them [4]. The turbomachinery consists of motor pumps and turbine generators that are often combined into the same bi-directional machine [4, 25]. PHES systems typically pump during off-peak times and release during periods of high demand [9, 22]. The water system used can be either open-loop, as with natural lakes and rivers, or closed-loop [6].

PHES stores electricity as potential energy due to gravity, which is directly proportional to mass times height. Its energy capacity is proportional to the volume of water stored and the height

difference between the reservoirs, and its power rating is dictated by the flow rate of the pipe system connecting them [4, 6, 25].

Some new designs of PHES systems use underground reservoirs directly below above-ground reservoirs so that environmental impact and friction are significantly reduced. Other methods involve using the sea as a lower reservoir since coastline is abundant [25].

Compressed Air Energy Storage

Compressed air energy storage (CAES) is the only commercialized bulk storage technology besides PHES [6, 10]. CAES stores energy by compressing air during off-peak periods, cooling it to reduce its volume, and storing it in a reservoir at 4 to 8 MPa. To release the energy, the air undergoes heating and expansion and then travels through a turbine generator [4, 6, 9, 22, 25]. The reservoir used can be an existing cavern underground, which requires specific geology but is more cost-effective, or above-ground in the form of a tank [5, 9, 22].

Existing systems use diabatic CAES, in which the heat removed during compression is lost and natural gas combustion engines heat the air during expansion [4, 9, 10, 22, 25]. With this method, systems can generate up to three times more energy than the amount required for heating [22].

Adiabatic CAES harvests the heat extracted during compression and uses it to re-heat the air during expansion, which requires thermal storage but theoretically removes the need for external fuel [4, 9, 25]. Isothermal CAES uses a different compression process that requires less heat storage, and it usually involves spraying water through air to absorb heat during compression and spraying the same warm water through the air again for expansion. Underwater CAES involves storing bags of compressed air under bodies of water so that the hydrostatic pressure helps with storage, and this can be combined with either adiabatic or isothermal CAES to further improve efficiency [4].

Flywheel Energy Storage

Flywheel energy storage (FES) systems store kinetic energy in a spinning rotor made of high-strength materials [6, 9]. These systems typically contain a rotor, a motor-generator, low-friction

bearings, and a strong enclosure that can be filled with either low-friction gas or a vacuum [4, 10, 22]. Low speed FES systems (10,000 RPMs or less) usually use rotors made of heavy steel discs and either mechanical or magnetic bearings, while high speed FES systems (10,000-100,000 RPMs) most commonly use composites for rotor materials and magnetic bearings [4, 25]. Low speed FES can be five times less expensive than high speed FES due to cheaper rotor materials and less motor-generator requirements [4].

To store and release energy, the FES system's rotor speed increases and decreases, respectively. An FES system's power rating is dictated by its motor-generator characteristics and power electronics limitations, while its energy capacity is determined by of rotor shape, material, and speed [4]. Low speed systems usually have high power capacities for short periods of time while high speed systems have low power capacities but can discharge for longer periods of time. The efficiency of FES is maximized if energy is released almost immediately after being stored due to self-discharge [6]. FES is modular and can be scaled up by adding additional flywheel units [5, 9, 10], and systems can be built underground if necessary [4].

Conventional Battery Energy Storage

A conventional battery contains two electrodes referred to as the cathode and the anode, and each electrode contains active materials for an oxidation-reduction (redox) reaction. Between the electrodes is an electrolyte that allows positive ions to flow through it from one electrode to the other during the reaction. Electrons must travel through an external wire to reach the other electrode, so neither electrons nor positive ions can move (and no reaction can occur) without an external circuit connection since space charge neutrality must be maintained [22, 26]. Batteries can be categorized as either primary (not rechargeable) or secondary (rechargeable), and they can be connected in series and in parallel until a desired capacity is achieved [25, 26, 27].

Lead Acid (Pb-Acid) is the oldest and the most commercially mature of all rechargeable battery technologies [9, 10]. A fully-charged Pb-Acid battery contains lead dioxide at its cathode, metallic lead at its anode, and a sulfuric acid solution as its electrolyte [4, 6, 10, 25]. During discharge,

both the lead and the lead dioxide electrodes react with the electrolyte to form lead sulfate, and the electrolyte's sulfuric acid concentration decreases. Charging reverses this [4, 28].

There are several types of traditional Pb-Acid batteries, and the most common types are flooded/vented and valve-regulated [8, 25]. Valve-regulated Pb-Acid (VRLA) batteries use either a gel or an absorbed glass mat to retain electrolyte [4]. Flooded Pb-Acid batteries are less expensive but require frequent refilling of distilled water and venting [8]. Traditional Pb-Acid batteries have a nonlinear power output dependent on several factors, and they necessitate float charging when idle to prevent self-discharge [25, 28]. Their lifetime has a heavy dependence on discharge rate, depth of discharge (DoD), and number of deep discharge cycles [28].

New Pb-Acid battery designs add carbon to one or both electrodes to improve power performance and reduce negative behaviors at partial state of charge (SOC) [6, 10, 29]. The added carbon minimizes sulfation, a process through which sulfate crystals grow on the anode and do not completely dissolve during charging [8]. As a result, these batteries have higher discharge capabilities, a faster recharge process, a longer cycle life, and minimal maintenance in comparison to traditional Pb-Acid [10]. Advanced Lead Acid batteries use carbon in one or both electrodes and often a supercapacitor implemented inside of the battery to further improve performance and lifetime, especially at partial SOC [8].

Lithium-Ion (Li-Ion) batteries were already common in consumer electronics and electric vehicles, and they now dominate the market for grid energy storage deployment [10, 28]. Li-Ion batteries are preferred in so many applications because of their energy and power density, efficiency, calendar life, and cost compared to competing technologies [8]. The ions in Li-Ion batteries undergo intercalation, which is the insertion of an external atom into a solid host without disrupting its lattice structure, from one electrode to the other. During charging, Lithium ions break away from the cathode and intercalate into the anode [4, 28]. The charging and discharging processes are visualized in Fig. 1.3.

Possible materials for the Li-Ion cathode include metal chalcogenides, transition metal oxides, and polyanion compounds, and some popular examples of each are lithium titanium disulfide, lithium cobalt oxide, and lithium iron phosphate, respectively [4, 7, 8, 26]. Lithium can be used for

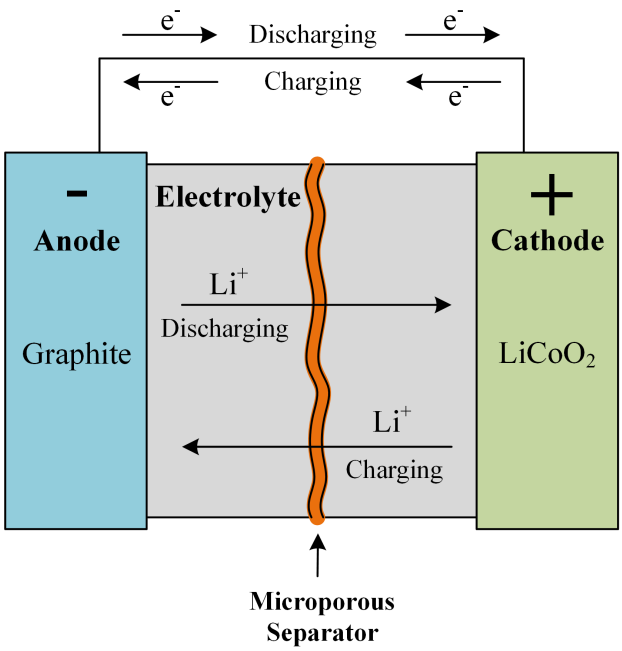

Figure 1.3: Li-Ion battery cell diagram [4, 10].

the anode, but safety concerns over the formation of lithium dendrites has led to the use of carbon-based, lithium titanate-based, silicon-based, or tin-based anodes instead [4, 6, 7]. The electrolyte of an Li-Ion battery can be made of liquid or gel, both of which contain dissolved lithium salts [4, 25].

Nickel-Cadmium (NiCd) technology was dominant for rechargeable batteries in the 1990s [6], but it has since been displaced by Li-Ion [24]. An uncharged NiCd battery has a nickel hydroxide cathode, a cadmium hydroxide anode, and an alkaline electrolyte. When it charges, the cathode is converted to metallic cadmium and the anode becomes nickel oxyhydroxide [4, 6].

Nickel-metal hydride (NiMH) batteries were used in portable electronics and the first generation of hybrid electric cars, but they have since been displaced by Li-Ion [24, 26]. They have the same contents as a NiCd battery except their anode consists of a metal alloy bonded with hydrogen [4, 24]. Without cadmium, NiMH is significantly more environmentally friendly than NiCd and has a higher energy density, but it also has a reduced cycle life and higher self-discharge in comparison [4]. Other nickel-based battery technologies include Nickel-Iron and Nickel-Zinc,

but there has not been much development of these since Pb-Acid and Li-Ion displaced them in the market [24].

Most conventional batteries have fast response, but they are sensitive to ambient temperature, discharge rate, and DoD [4, 8, 24]. Also, it is very difficult to measure the SOC of these batteries since they are completely enclosed [24].

Molten Salt Battery Energy Storage

Sodium Sulfur (NaS) battery technology is the most proven so far for MW-scale battery storage [4]. Molten sulfur and molten sodium compose the charged NaS cathode and anode, respectively, and the electrolyte is a solid beta alumina ceramic that only permits the passage of positive sodium ions [4, 6, 28]. When NaS batteries discharge, sodium is oxidized at the interface between the anode and the electrolyte and Na^+ ions are formed, which pass through the electrolyte to combine with sulfur being reduced at the cathode. Thus, sodium pentasulfide is formed at the cathode, which cannot mix with sulfur, so a two-phase liquid mixture exists at the cathode until all remaining sulfur is consumed [6, 10].

NaS batteries require very high operating temperatures, usually between 300 and 350 degrees Celsius (°C) [4, 5, 6, 8, 10, 24, 28]. The charging and discharging processes are endothermic and exothermic, respectively, which result in a slight temperature decrease during charging and a high temperature increase during discharging when ohmic losses are considered. Since discharging releases more heat than what is gained during charging, the battery can maintain its own high temperature with close to no self-discharge if it has frequent charge/discharge cycles. During standby, heaters are necessary for maintaining the battery's temperature at 290-300 °C, which causes a self-discharge of up to 20% per day [4]. NaS batteries are capable of long discharge cycles as well as pulse power delivery [4]. Their internal resistance varies greatly with SOC [28].

Sodium Nickel Chloride ($NaNiCl_2$) batteries have been designed primarily for electric and hybrid electric vehicle applications [6, 24], and similar to NaS, they require high operating temperatures of 270-350 °C [4, 6, 10, 24]. Like NaS batteries, the charged $NaNiCl_2$ has a molten sodium anode and a beta alumina ceramic electrolyte, but its cathode consists of solid $NiCl_2$ instead

of molten sulfur [4, 6, 10]. Also, a second electrolyte of molten sodium chloroaluminate ($NaAlCl_4$) is added to the cathode side of the ceramic [4]. When discharging, chloride ions are released from the $NiCl_2$ and combine with sodium ions to produce nickel and NaCl with no side reaction [6, 10]. If the solid electrolyte fails and the molten sodium reacts with molten sodium chloroaluminate, two non-hazardous materials are produced [4].

Metal Air Battery Energy Storage

Metal air batteries contain porous cathodes so that oxygen from the air can be used to react with an electropositive metal serving as the battery's anode [4, 6, 10]. During discharge, hydroxyl ions are formed at the cathode and travel through the electrolyte to react with the metal at the anode, which then releases electrons [24]. Rechargeability has been demonstrated for zinc-air, sodium-air, and lithium-air cells but not yet for magnesium or aluminum cells [4]. Since metal air batteries only have one traditional electrode, their theoretical specific energy is the highest of all battery types [4].

Flow Battery Energy Storage

Flow batteries are different from other battery types in that one or both active materials is contained in the electrolyte solution [6, 10]. The flow battery system contains stacks of cells, two electrolyte storage tanks, and two pumping systems [30]. The stacks are connected in series and/or parallel, and each stack contains two electrodes and a proton-exchange membrane as shown in Fig. 1.4 [4, 10]. The electrolyte solutions are pumped from the storage tanks to the stacks to fill the gaps between the membrane and the electrodes [8]. For the system to begin operating, the pumps must ramp up and flood the stacks with electrolyte material, and during operation, the electrolyte(s) are circulated in separate closed-loop system(s). When operation is complete, the electrolyte solution(s) are drained off of the stacks to prevent self-discharge [4, 29].

One unique advantage of flow batteries is the independence of their power and energy ratings due to external storage of their active materials. The power rating of a flow battery system is a function of the active area of the stack and the number of stacks connected in series and parallel

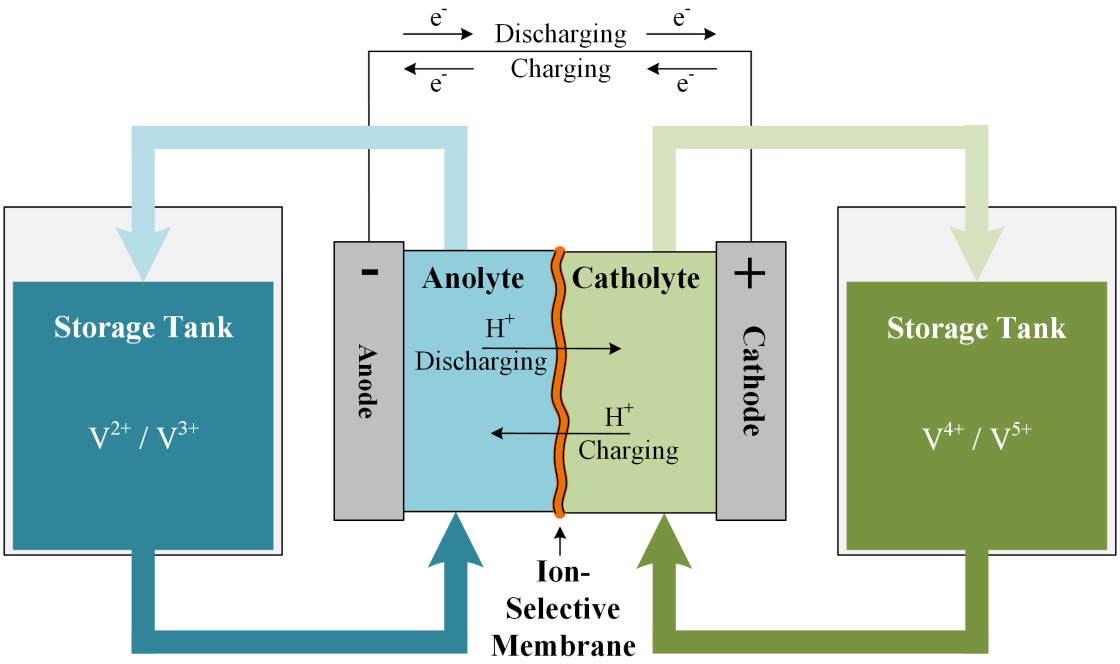

Figure 1.4: Flow battery cell diagram [4, 6, 10].

[4, 8]. The energy rating is dependent on the external storage tank size. Due to this unique feature, reduction and oxidation (redox) flow batteries will likely find a niche in large-scale energy storage, as they already have several advantages over the mature Lead Acid technology [7, 31]. Also, their architecture allows for easy replacement of individual stacks when necessary [28].

The vanadium redox (VRB) battery is the most mature flow battery technology [9, 24], and its design utilizes the reduction and oxidation of vanadium. VRB batteries contain two external electrolyte storage tanks that contain different oxidation states of vanadium dissolved in sulfuric acid solutions [4, 10, 24]. When the VRB battery charges, $V4^+$ ions at the cathode release electrons to become $V5^+$ ions, and these electrons are paired with $V3^+$ ions at the anode to form $V2^+$ ions [4, 6, 10].

Zinc-bromine (ZnBr) flow batteries are also based on redox reactions [4, 28]. Like VRB, ZnBr systems contain two separate electrolyte storage tanks and flow streams, which are aqueous solutions of zinc bromide in different oxidation states [6]. During charging, metallic zinc is plated on the anode and elemental bromine gathers near the cathode, combines with other agents to create polybromine, and eventually circulates back to the storage tank [6, 10]. Circulation of both tanks

helps to remove polybromine from the cathode and zinc dendrites on the anode [10, 28]. Additional types of flow batteries include polysulfide bromide, iron chromium, and cerium zinc [4, 6, 10, 24].

Supercapacitor Energy Storage

Supercapacitors (SES) are also known as ultra-capacitors, electrochemical capacitors, and electric double layer capacitors [6]. They are a merge between pure capacitors and batteries in that an electrolyte solution replaces the solid dielectric but energy is still stored in an electric field [6, 24, 25, 26]. The added electrolyte gives the capacitor a larger capacitance and energy density but still allows it to charge and discharge very quickly [6, 25]. The electrodes of a supercapacitor can be composed of either the same material or different materials [24], and they often consist of nanotubes that increase their surface areas [25]. Like battery cells, supercapacitors can be arranged in parallel and in series to garner the desired capacity [4].

There are three primary types of supercapacitors: the electrochemical double-layer capacitor (EDLC), the pseudocapacitor, and the asymmetric or hybrid capacitor. In EDLCs, the surface of each electrode accumulates charge and attracts ions of opposite charge in the electrolyte, which results in a double layer of charge at each electrode. Pseudocapacitors contain redox reactions on electrode surfaces like batteries, forcing charge to pass through the double layer of charge for electrochemical storage and thus improving energy density. Asymmetric or hybrid supercapacitors have two different electrode devices, two different electrode materials, or both [4].

Superconducting Magnetic Energy Storage

Superconducting magnetic energy storage (SMES) stores energy in a magnetic field resulting from a direct electric current flowing through a superconducting coil [25]. The current flowing through the coil increases during charging and decreases during discharging [6]. SMES systems contain the superconducting coil, cryogenic refrigeration, a containment vessel, and a power conditioning system [6, 24]. Coils for SMES can be made of either low temperature or high temperature superconductors, and they can be solenoidal or toroidal in shape. SMES coils must be cooled below their superconducting critical temperatures [6], which is usually done with cryogenic liquids

[4]. Since the coil is superconducting, the system's only substantial energy losses can be attributed to the cooling system [25].

Technology Comparisons

A summary of each storage technology's applications, advantages, and disadvantages is shown in Table 1.2. PHES and Pb-Acid are the most mature storage technologies, and CAES, FES, Li-Ion, NaS, $NaNiCl_2$, VRB, SES, and SMES have been demonstrated and are commercially available. Mechanical energy storage types tend to have the longest calendar lifetimes, and batteries tend to have the shortest calendar lifetimes due to chemical deterioration. PHES and CAES are suitable for long term storage while FES, SES, and SMES are only practical for short-duration applications. This coincides well with FES, SES, and SMES having the fastest response times (milliseconds) [6].

Metal air batteries have the highest energy density, which is close to that of many carbon-based fuels. Other batteries and CAES have moderate energy densities while PHES, FES, SES, and SMES have the lowest. In terms of efficiency, Li-Ion batteries, FES, SES, and SMES have the highest (greater than 90%), while metal air batteries have the lowest (less than 50%). PHES, CAES, and Zn-air batteries have the lowest capital cost per kWh, and FES, SES, and SMES have high capital costs per kWh. However, FES, SES, and SMES have low capital costs per cycle, which makes them suitable for short-duration applications [6]. Advanced Pb-Acid, Li-Ion, and flow batteries are expected to further decrease in cost, while NaS and traditional Pb-Acid are relatively mature and will likely not see much more significant reduction in price [8].

In terms of capacity, PHES and CAES are typically used for large-scale grid applications, and molten salt and flow batteries could be additional contenders for large-scale applications if their costs are reduced. Smaller scale applications are dominated by batteries, especially Li-Ion and molten salt. Metal air technologies could also compete for small-scale systems, but their cycle life and maximum discharge rate must be improved first [24].

Li-Ion batteries are the fastest-growing technology at this time due to their high energy density, high power, high efficiency, and low self-discharge [22]. Other technologies that are likely to

Table 1.2: Applications, Advantages, and Disadvantages of Energy Storage Technologies

Technology	Applications	Advantages	Disadvantages
PHES [4, 5, 9, 25]	Energy arbitrage Capacity upgrade deferral Reserves Frequency and voltage regulation	Most cost-effective Highest capacity capability Fast response Long discharge duration Long calendar lifetime Minimal maintenance	Geographically limited (requires close land areas with high elevation difference) High environmental impact due to reservoir construction and varying water levels High capital cost Low energy density Significant lead time necessary
CAES [4, 5, 25]	Energy arbitrage Renewable smoothing Load following Reserves	High power and capacity capability Long discharge duration Long calendar lifetime Standard combustion turbine is easy to integrate into power system	Geographically limited (except for above-ground systems) Some environmental impact due to combustion emissions Low efficiency
FES [4, 5, 6, 9, 10, 22, 26]	Renewable smoothing Load leveling Frequency regulation Transient stability Power quality UPS	Very fast response High power density Very long cycle life, independent of DoD High efficiency Low maintenance Wide operating temperatures and conditions Little environmental effects (produces noise)	High self-discharge due to friction Scalability for large-scale applications is difficult
Pb-Acid [3, 4, 6, 8, 9, 10, 24, 25, 28]	Energy arbitrage Renewable smoothing Load leveling Black start Power quality UPS	Low cost Fast response Wide operating temperatures and conditions Low self-discharge Recyclable	Low cycle life Low energy density Low DoD capability due to sulfation and hydration Electrodes vulnerable to corrosion Contains toxic lead and corrosive sulfuric acid Produces explosive gases (hydrogen and oxygen) when charging Most types require refilling with water due to hydrolysis (except for VRLA)

Table 1.2, continued.

Technology	Applications	Advantages	Disadvantages
Carbon or Advanced Pb-Acid [4, 6, 8, 24, 25, 28]	Energy arbitrage Renewable smoothing Load leveling Frequency regulation Transient stability	*Compared to traditional Pb-Acid:* Better performance at partial SOC Higher cycle life Faster recharge Lower maintenance Hydrolysis occurs less frequently Faster response Still low cost	*Compared to traditional Pb-Acid:* Still limited DoD Still low energy density Electrodes still vulnerable to corrosion
Li-Ion [4, 5, 6, 8, 9, 10, 24, 25, 27, 28, 32]	Renewable smoothing Load leveling Reserves Frequency regulation Transient stability Power quality UPS	High power density High energy density Very high efficiency High DoD capability Long cycle life Low self-discharge Tolerant of low temperatures No memory effect	High cost Fire risk due to the combustibility of lithium Very sensitive to overcharge, overdischarge, high temperatures, and internal pressure buildup Some electrode and electrolyte materials are toxic Availability of lithium is limited
NiCd [4, 6, 24]	*Generally displaced by Li-Ion for grid applications*	Long cycle life High DoD capability Wide operating temperature range Low maintenance Fast recharge	High cost Exhibits memory effect Cadmium is toxic
NiMH [4, 5]	*Generally displaced by Li-Ion for grid applications*	Long cycle life High energy density Wide operating temperature range No maintenance Fast recharge	High cost Exhibits memory effect
NaS [4, 5, 6, 8, 9, 10, 24, 28]	Energy arbitrage Capacity upgrade deferral Congestion relief Renewable smoothing Load leveling Reserves Power quality UPS	High power and energy density Long cycle life Long discharge duration (6+ hours) High efficiency Fast response Low self-discharge Low material cost Low maintenance Capable of temporary discharge above rated power	High operating temperature required (needs thermal management) Molten salts are corrosive and metallic sodium is highly combustible High cost

Table 1.2, continued.

Technology	Applications	Advantages	Disadvantages
$NaNiCl_2$ [4, 24]	Energy arbitrage Capacity upgrade deferral Renewable smoothing Load leveling Reserves Power quality UPS	Long cycle life High efficiency Lower operating temperature than NaS Lower environmental risk than NaS Low maintenance	High operating temperature required (although slightly lower than NaS) Molten salts are corrosive High cost
Zn-Air [6, 10, 24]	*Still in development for grid applications*	Very high energy density Low cost Little environmental impact	Short cycle life Low efficiency Very sensitive to ambient air conditions and contaminants Poor fast discharge capability Fabrication of air electrode is difficult
VRB [4, 6, 9, 10, 24, 31, 33]	Energy arbitrage Capacity upgrade deferral Renewable smoothing Load leveling Reserves Frequency regulation Voltage support Power quality UPS	Capacity and power rating are independent Very long cycle life, independent of DoD High DoD capability No self-discharge Safe materials Fast response Both electrolytes are same material Electrodes do not undergo physical or chemical changes Tolerant of overcharge and overdischarge Capable of temporary discharge above rated power Low maintenance	Low energy density due to low solubility of vanadium High cost Need for pumps, sensors, and external containment Membranes susceptible to premature degradation
ZnBr [10, 24, 28]	Energy arbitrage Capacity upgrade deferral Renewable smoothing Reserves Frequency regulation Power quality UPS	Capacity and power rating are independent Very long cycle life, independent of DoD High DoD capability No self-discharge High efficiency Inexpensive materials Electrodes do not undergo physical or chemical changes Tolerant of overcharge and overdischarge Low maintenance	Low energy density High cost Bromine is corrosive and toxic Need for pumps, sensors, and external containment Membranes susceptible to premature degradation

Table 1.2, continued.

Technology	Applications	Advantages	Disadvantages
SES [4, 5, 6, 24, 25]	Frequency regulation Transient stability Power quality	Very fast discharge capability Fast response Very high cycle life Wide operating temperature range Minimal environmental impact	High cost Low energy density High parasitic losses High self-discharge
SMES [4, 5, 6, 24, 25]	Frequency regulation Transient stability Power quality	Very fast discharge capability Fast response Very high cycle life High efficiency Low environmental impact (produces large magnetic field)	High cost Low energy density Requires cryogenic cooling system Difficulty of power conditioning and control

see growth are CAES, molten salt batteries, flow batteries, and SES [24, 26]. Significant growth for PHES and CAES will likely be hindered by political, geographical, and environmental factors [26, 28].

1.1.3 Economics

Economic analysis of energy storage has several facets, most of which are dependent on the technology used and the anticipated application. Costs and benefits can be either static, such as construction costs, or dynamic, such as operational costs. Dynamic costs and benefits depend heavily on charging algorithm and discharge pattern. Profit is earned by selling power (or discharging) when prices are high and buying power (or charging) when prices are low. The optimal timing of this depends on market price fluctuations, other nearby energy sources, and load demand [34].

Reservoir-based storage costs depend heavily on the geographical setting of the reservoir and its design. The costs for electrochemical energy storage technologies depend more on whether their intended application is for integrating renewables or providing T&D support. Operation and maintenance costs are dependent on siting and operational hours for reservoir-based systems and chemistry-specific battery requirements for electrochemical systems.

Systems with the highest revenues often provide benefits that span multiple types of applications. The highest value applications are often frequency regulation, power quality and reliability, T&D upgrade deferral, and adding to local or system capacity [9]. For these applications, the payback period for advanced batteries can be as short as four years [8].

1.1.4 Current Status

Energy storage projects in the United States have increased by 105% between 2013 and 2016 [22]. The United States is the global market leader for battery storage deployment, which has been accelerated by a federal stimulus package implemented in 2009, regulations that value energy storage services, grid reliability issues, state-level storage mandates, and renewable support programs. Other grid-scale battery storage leaders include Japan, Germany, Italy, and China [8, 35].

As of August 2016, the United States has more than 24 GW of energy storage installed, and more than 90% of that capacity is provided by PHES. Electrochemical storage systems constitute more than half of these storage installations but only 0.57 GW of capacity [35, 36]. Operational battery storage systems around the world contain Pb-Acid, Li-Ion, Nickel-based, molten salt, and flow battery technologies [22].

The primary barriers for widespread energy storage deployment today are the need for cost-competitive technologies, validated reliability and safety, an equitable regulatory environment, and industry acceptance [5]. Research must be conducted on ways to improve the cost, efficiency, manufacturability, and reliability of these systems, and standards for performance and grid interfacing need to be set [5, 6, 8].

1.2 The Hardware Testbed

In recent years, a converter-based grid emulator referred to as the Hardware Testbed (HTB) has been developed for studying future power system scenarios with high penetration levels of renewables. Inside the HTB, voltage source inverters are controlled to emulate the behaviors of

power system components [37, 38, 39, 40]. The bandwidth of these converters can be designed to be several kHz depending on topology, requirements, loading conditions, and switching capabilities of the devices [40]. Thus, the output current and voltage characteristics of each emulator imitate the power system component's actual dynamics.

1.2.1 Motivations and Advantages

Simulation software like PSSE and hardware tools like RTDS can be used to analyze power system scenarios, but these tend to focus on either small-scale transients or large scale behaviors [41]. Digital simulations can have numerical oscillations due to discontinuities and improper interpolation, and they often ignore or oversimplify imperfections like measurement error, time delay, non-linearity, and electromagnetic interference [42]. Users of digital simulation tools typically oversimplify the scenarios and conditions they are testing, so experimental results are generally still more credible than simulation results. However, important characteristics of some power system components are changed when scaled down to laboratory settings, such as the inertia of a rotating machine. Combining digital simulations and physical tests greatly improves the effectiveness of testing but still retains the flexibility of digital simulations [43].

Converters can be controlled to emulate both broad and detailed dynamics, so the useful time scale of the HTB can range from milliseconds to hours [41]. Thus, it can emulate all electromechanical phenomena and some electromagnetic phenomena in power systems as permitted by the converter switching frequency. The HTB also utilizes real-time communication, protection, control, and cybersecurity, and it can perform long experiments in real time with detailed system information [42]. It is also designed so that power is circulated between generation-emulating converters and load-emulating converters, so the only losses in the system are in the converters themselves [37, 38].

The HTB provides an excellent platform for designing and testing new technologies for power system monitoring, control, actuation, and visualization. It also allows for the study of renewables, responsive loads, and energy storage, as well as new architectures like HVDC. The converters used

as emulators are modular and reconfigurable, so the system is flexible in terms of the scenarios it can emulate [37, 38].

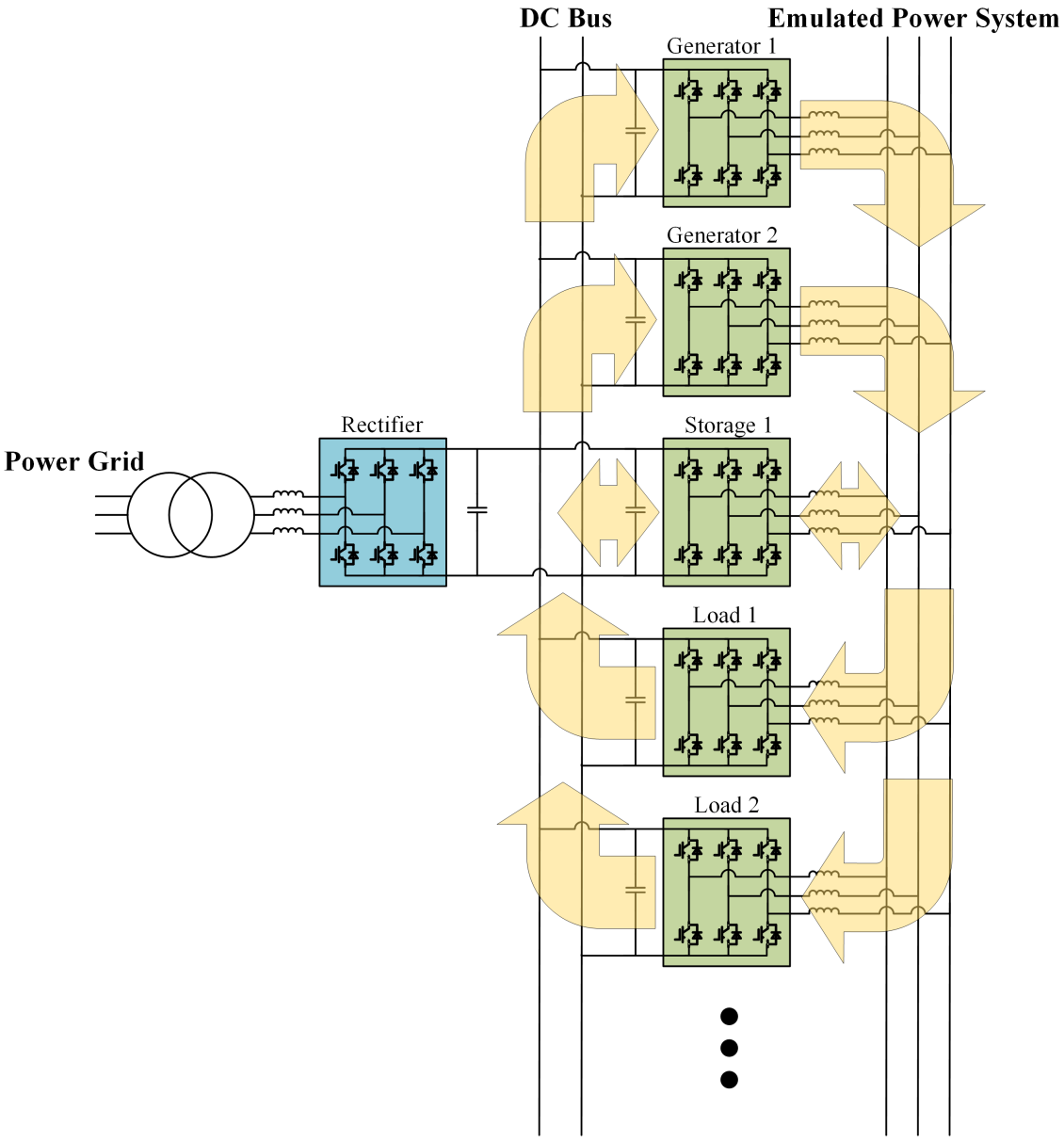

Figure 1.5: Power circulation within the HTB.

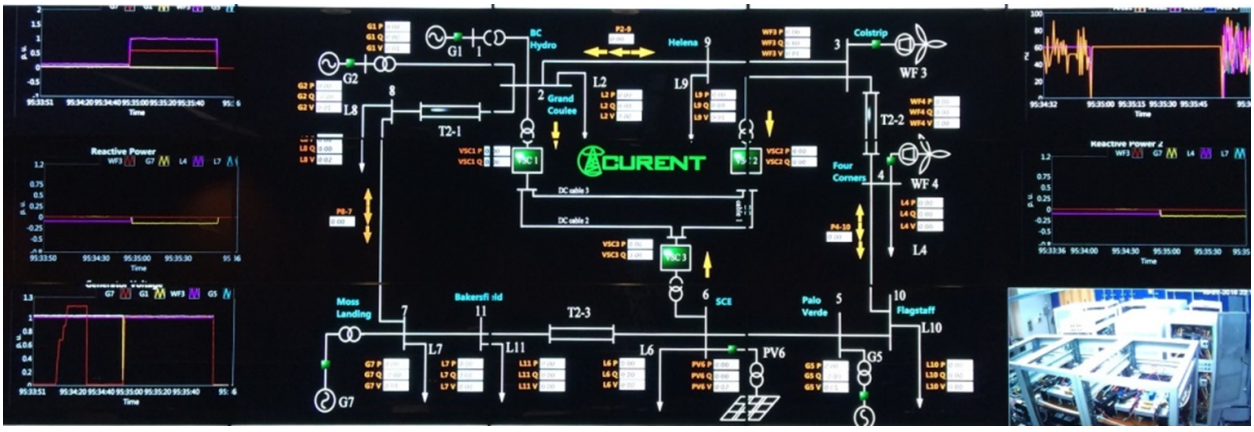

Figure 1.6: Visualization screen for the HTB.

1.2.2 Construction and Operation

The HTB is arranged so that all converters (75 kVA Vacon drives, p/n 70SC000418) are connected to a single DC link on one side and the three-phase HTB power system on the other, as shown in Fig. 1.5. The system connects to the actual grid using a transformer and an active rectifier to supply the DC link voltage [38, 44]. During operation, power flows from the DC link to the three-phase power system for generating emulators and the opposite direction for consuming emulators, so power circulates between the inverters. Synchronization is achieved using active power and frequency droop [37, 42].

Dynamic models for the emulated power system components are implemented on TMS320F28335 digital signal processors (DSPs), and each DSP uses its assigned model to control one of the converters on the HTB. Power system components that establish voltage and frequency are typically modeled as voltage sources and other components are modeled as current sources [42]. Each current source model contains a fast inner current control loop for the inverter and an outer voltage control loop that supplies a dynamic current reference to the inner current loop [37].

A visualization screen that imitates a control center (Fig. 1.6) is realized through LabVIEW, which gathers data from PMUs and FDRs and relays it to the control screen through Ethernet. The control screen is updated with active power, reactive power, frequency, and voltage data with a frequency of 10 Hz [42].

1.2.3 Existing Emulators

The HTB contains emulators for several different power system components. The three-phase synchronous generator emulator mimics the behavior of a steam turbine and contains realistic droop control and exciter control [37, 38]. A full-converter wind turbine emulator behaves like a variable-speed wind turbine with a permanent magnet synchronous generator, and it contains pitch control and frequency support control [45, 46]. A solar photovoltaic array emulator is implemented with a realistic two-stage power electronics interface and contains a maximum power point tracking mode and a reserve power mode [39].

For loads, the HTB contains a conventional load emulator that combines constant impedance, constant current, and constant power (ZIP) loads together. Other load emulators include a nonlinear load emulator as well as a three-phase induction motor load emulator that mimics the dynamics of a large squirrel cage system [38, 40, 41, 47, 48]. The HTB is currently capable of only one type of energy storage emulation, which is for flywheel energy storage [49]. Long AC transmission lines and HVDC can also be emulated, as well short-circuit faults [50, 51, 52].

1.3 Project Description

Prior to this project, flywheels were the only type of energy storage that could be emulated on the HTB. As described in section 1.1.2, flywheels are only suitable for high power, short duration applications. They have very fast response times and a long cycle life, but they have high self-discharge and are difficult to scale to large capacities. Thus, the HTB lacked emulation capability for longer duration and higher capacity energy storage. As apparent in Fig. 1.2, battery storage is intuitively the next technology to emulate on the HTB if longer duration and higher capacity storage are desired. Thus, this project entails the development, testing, and utilization of a converter-based battery energy storage emulator for the HTB.

Since numerous battery technologies exist for grid applications, three were chosen for implementation in the emulator. Li-Ion was selected for its efficiency, short-term dexterity, dominance in the current energy storage market, and overall prevalence. Pb-Acid was selected for

its maturity, low cost, and current prevalence even though new installations are limited. The VRB flow battery was chosen for its high energy capacity capability, maturity among flow batteries, and expected prevalence in the near future [53].

The battery storage emulator contains an internal model for the battery itself, models for the typical electrical interface between a BESS and the grid, and all high-level control capabilities of a typical BESS. Each of these reflects realistic dynamic behavior, and the ultimate control outputs are current references for a voltage source inverter on the HTB [53].

The emulator also contains outer control loops for various power system applications for use on the HTB. Frequency regulation, inertia emulation, and voltage support were selected for their support capabilities of power systems with high renewable penetration. The battery storage emulator is now capable of operating all three of these functions simultaneously.

1.4 Thesis Structure

In Chapter 1, power systems applications for energy storage have been introduced, along with several types of energy storage technologies. Also, the HTB project and the desired specifications for the new BESS emulator have been described. In Chapter 2, a literature review is conducted on previous battery emulation, BESS structure, internal battery modeling, power conditioning system modeling and control, and application-specific control for BESSs. Chapter 3 includes a detailed description of the BESS emulator design process including modeling, control design, discrete implementation, and verification via simulation. Chapter 4 describes the experiment process on the HTB for each of the BESS emulator's control functions and discusses in detail the responses observed. Finally, Chapter 5 summarizes the conclusions of this work and provides recommendations for future work using the BESS emulator.

Chapter 2

Literature Review

A literature review is conducted for material applicable to the BESS emulator development, beginning with previous battery emulation. Then, the structure, control, and converter interface options for typical BESSs are described. Internal battery model options are explained in detail, along with power conditioning system modeling and control techniques. Methods for controlling storage to support the system's frequency and voltage are also reviewed.

2.1 Previous Battery Emulation

Battery storage emulation has been used extensively for electric vehicle testing, as demonstrated in several publications [27, 54, 55, 56, 57, 58, 59, 60]. Testbeds for electric vehicle powertrains require large capital costs as well as a large amounts of space with controlled environmental conditions [27, 55]. The battery is the most expensive part of an electric vehicle powertrain [57], and it requires pre-conditioning such as charging and heating prior to experiments [54, 59]. Also, battery degradation due to cycling and/or age prevents repetition of exactly the same test conditions for multiple experiments [27, 54, 59]. Real batteries require maintenance and eventual replacement, and exposing them to some test conditions such as overcharging could create safety hazards [57, 58].

A battery emulator imitates the terminal voltage and current of a battery in real time for experimental testing, and it usually demonstrates the battery's capability to provide power as well as its dynamic behavior [57, 59]. Thus, using a battery emulator for experimental testing presents several advantages, with the most prominent being reduced cost [27, 57]. It also provides increased flexibility since the battery's states can be changed immediately without pre-conditioning and those exact experimental states can be reproduced later [27, 54, 57]. Battery emulation is beneficial for studying DC bus voltage stability in the powertrain, and it is also useful for powertrain tests during early stages of development or before battery prototypes are available [54, 57]. Battery emulators can usually mimic a wide range of battery types with good accuracy for both static and dynamic states [27, 55].

Battery emulation can be conducted using controllable voltage supplies, programmable power supplies and electronic loads [55, 60], or power converters [54, 56, 57, 59] to mimic a battery's behavior at its terminals. All of these methods use an internal battery model that produces terminal voltage and/or current values based on programmed and measured states [58, 59]. The physical emulator is then controlled with a digital signal processor, a computer, or a microcontroller to mimic the computed terminal behavior [27, 58]. Bi-directional DC-DC converters are particularly suitable for battery emulation because they can be controlled so that their output voltages are constant regardless of input or load variations [27]. The dynamic behavior of a battery is far slower than the typical switching frequency range of a converter [59].

Battery emulation with power electronics requires a converter that can deliver very high voltage and current levels without compromising dynamic response, and the dynamic nature of the hardware itself must not interfere with the BESS behavior being emulated. Also, an accurate battery model that can be used in real time computation is required, along with a controller that can mimic the battery's behavior even through sudden load changes [54].

The same motivation for battery emulation can be applied to larger power system applications such as the electric grid. Large-scale battery energy storage systems (BESSs) are too costly, bulky, and inflexible to be used in system-level experimental testing. A BESS emulator for grid applications would allow simple testing for battery storage size and location within the power

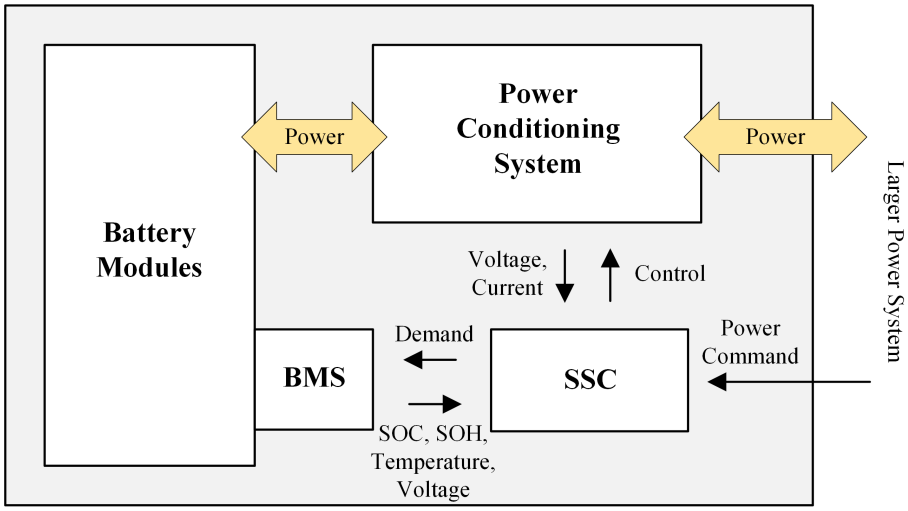

Figure 2.1: BESS diagram [8].

system with actual hardware, which is particularly useful for test systems like the HTB. However, there does not yet exist a BESS emulator in literature specifically for grid applications.

2.2 Battery Energy Storage Systems

BESSs have become significantly more popular for grid applications in recent years as a result of their versatility, modularity, fast response time, high energy density, and efficiency [7, 35]. They can respond to the needs of power systems close to instantaneously, but they can also provide services that require long discharge durations [7]. A typical BESS contains the battery itself, monitoring and control systems, and a power conversion system that connects the BESS to the utility or larger power system [7, 8, 15, 61]. Flow battery systems also have external electrolyte storage tanks and pumping systems that circulate the electrolytes through the reaction stacks [8]. A typical BESS is arranged as shown in Fig. 2.1.

2.2.1 Battery Configuration

For conventional batteries, cells are connected in series and/or parallel to form modules, which are then organized into battery packs [7, 8, 56]. Additional packs are added until the system

has enough capacity for its intended applications. A single system may have several independent sections of battery packs and power conditioning systems, which are known as power blocks [7]. Large BESS's are typically connected to lower distribution networks at medium voltage levels [62, 63].

Battery cells tend to have small variations in their characteristics as a result of imperfect manufacturing and uneven operating conditions. These differences cause varying rates of cell aging and capacity fade, and cells with the lowest capacity levels limit the charging and discharging capabilities of entire series-connected strings by stopping current flow when they reach their individual cut-off voltage levels. Thus, in order to fully utilize the capacities of all cells in a string, special circuits should be installed to compensate for state of charge (SOC) differences [63].

Strategies for balancing SOC levels between cells can be either passive or active. In active balancing, unneeded energy is rerouted to other cells using auxiliary storage devices like capacitors and inductors. Passive balancing circuits usually consist of shunt resistors that dissipate energy as necessary. Although energy loss is involved, passive balancing is more common due to its simplicity and low cost [63].

If protection measures are not implemented, a single cell failure in a series-connected string can cause an entire pack to fail. Thus, intelligent battery packs often incorporate bypass systems that contain two MOSFETs per cell, one in series and one in parallel. This is not always practical for large systems, so similar bypass circuits can be installed on the module level as well. These circuits can also be used for active cell balancing by controlling the duty cycles of the switches [63].

For BESSs with high power and energy ratings, constructing large monolithic battery packs can be avoided by arranging several complete power blocks in parallel. With this configuration, failure of a single cell will result in loss of only its string instead of a larger string in a monolithic system. However, it should be noted that this configuration loses the economies of scale intrinsic in a monolithic system, and it requires that the total DC current be higher since the total DC voltage is lower [63].

There are three common design approaches for BESSs. The first consists of simple battery packs that contain a low number of cells in series (usually 200-300) and a passive balancing scheme. Several power blocks are arranged in parallel and the power conditioning system steps up their DC bus voltage (usually 600 V) for use with the larger power system. The second approach utilizes a larger intelligent battery pack that contains numerous cells in series, and it connects to the larger power system with only a converter and no step-up device. The third common approach uses a cascaded H-bridge multilevel converter (CHB), which will be explained in more detail in section 2.2.3 [63].

2.2.2 Monitoring and Control System

A large-scale BESS contains a battery monitoring system (BMS) for the batteries and a system supervisory control (SSC) for the whole system. Together, the BMS and SSC manage how the storage is used in order to maintain safety and optimal performance [7]. They oversee the charge and discharge processes, optimizing charge/discharge patterns to prevent battery degradation, and they keep estimates of the system's SOC and state of health (SOH) [7, 8]. The BMS also balances the SOC of cells for closed-cell systems and controls the electrolyte flow rate of flow battery systems. In terms of safety, the BMS and SSC are also responsible for thermal management, adherence to current and voltage limits, and shutdown during faults [7].

The BMS directly monitors battery conditions, and the SSC serves as an interface between the BMS and the larger power system. The BMS sends information about battery pack states such as SOC, SOH, temperature, and voltage levels to the SSC, and the SSC makes decisions about charging and/or discharging based on these states and the power system's needs. The BMS consists of low-level processors installed for monitoring and cell balancing within single modules, and another layer of processors monitors their data and actions. Then, a top-level processor serves as a liaison between the mid-level processors and the SSC, communicating the needs of the batteries to the SSC and distributing the SSC's commands. Detailed information about the system is distributed among low-level processors, and only essential information is relayed up to the top-level controller.

This architecture greatly reduces the amount of information traffic and is therefore significantly more scalable [7].

Flow batteries are open systems that allow for simple measurement of the electrolyte's active material concentration for SOC estimation. Since conventional batteries tend to be closed-loop systems, estimating their SOC and SOH can be difficult. The only directly-measurable battery states for closed battery systems are voltage, current, and temperature. SOC can be estimated by counting the flow of charge over time, but this does not account for variable losses in the battery, self-discharge, series string balancing, or side reactions. SOC can also be estimated using the battery's open-circuit voltage, but this does not consider capacity fade and some batteries have a very flat voltage-vs-SOC curve. SOH is most commonly estimated by measuring the battery's equivalent DC resistance but can also be calculated more accurately from a complete charge-discharge cycle under controlled conditions [7].

A simple BMS can be used for basic charge/discharge functions, but model-based BMSs can help reduce degradation and further improve performance. Physics-based models allow BMSs to closely estimate several internal states that give it a thorough understanding of battery SOC and SOH. Implementing these models requires advanced architecture and power electronics, and the algorithms used must be efficient enough to satisfy model nonlinearities, constraints, and objectives in real time [7].

2.2.3 Power Conditioning System

The power conditioning system is the electrical interface between the battery assembly and the larger power system [4]. Standard power conditioning systems contain two-port four-quadrant AC-DC power converter systems and often a transformer [7, 23]. The power conditioning system controls power flow between the BESS and the greater power system, and it ensures that interconnection requirements and grid codes are met during operation [8, 62]. Typical topologies for the power electronics used in power conditioning systems are described as follows.

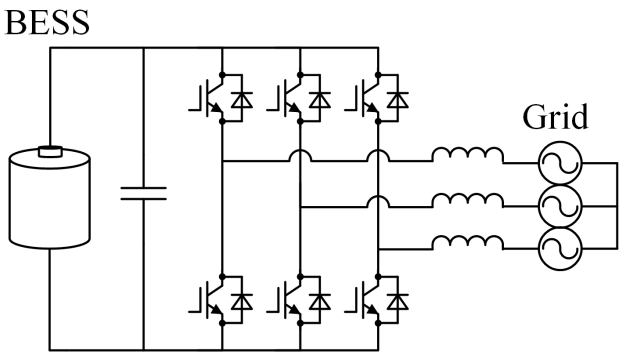

Figure 2.2: VSI topology for BESS interface [23].

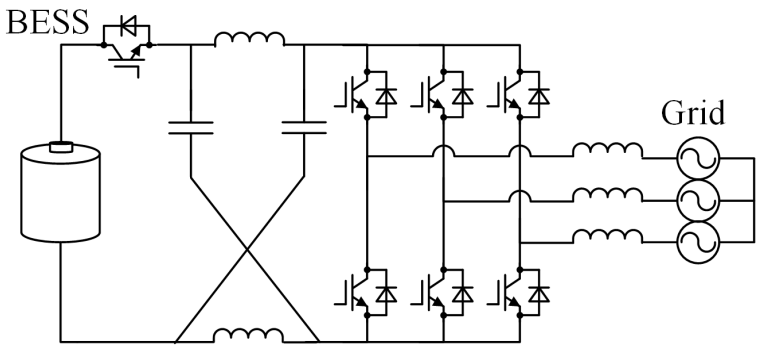

Figure 2.3: ZSI topology for BESS interface [23].

Single-Stage Topologies

Single-stage topologies consist of one non-isolated AC-DC converter that contains all necessary charging/discharging control for the battery system. The simplest and most efficient single-stage converter is the voltage source inverter (VSI), which is shown in Fig. 2.2. The VSI uses the battery bus as its DC input, so their AC output limit is the battery bus's DC voltage. VSIs are sensitive to shoot-through, so its switches must be programmed with a dead time long enough to prevent cross conduction even though it distorts the waveform. The Z-source inverter (ZSI) is a slight alteration of the VSI that utilizes shoot-through states to provide boost function, and it is shown in Fig. 2.3. The ZSI has more regulation freedom and therefore allows for better utilization of the batteries [23].

The bidirectional matrix converter contains six four-quadrant switches, each of which can be realized using pairs or groups of devices. It does not require passive components other than those

used in filters, and it allows for control of voltage and current in either direction. If a Z-source network is added at its DC side, the matrix-Z-source inverter is derived and can boost voltage just like a normal ZSI. The matrix-Z-source inverter can handle variable-voltage-variable-frequency AC input and output with no additional control or energy storage [23].

Single-stage topologies are simple and have lower device counts, lower costs, and less losses than multiple-stage systems. However, all battery modules are typically connected in series to create a high bus voltage, so the whole system is compromised if only one module fails. To reduce this risk, single stage topologies may also contain a transformer to boost the AC voltage up to the line voltage so that the battery strings can be shorter [23, 62].

Double-Stage Topologies

In double-stage topologies, a DC-DC converter conducts charging/discharging control for the BESS and boosts its voltage up to a common DC link so that an AC-DC converter can serve as a direct interface between the DC link and the larger power system [23]. The DC-DC converter absorbs all variations in the battery bus voltage so that the AC-DC converter can be optimally designed for a single operating point at a constant DC link voltage [62]. Double-stage topologies can be either isolated or non-isolated [23].

The bidirectional half-bridge has the advantages of simplicity and high efficiency, and it is widely used for these reasons [23, 62]. The half-bridge has two transistors and one inductor as shown in Fig. 2.4, which are arranged to buck the voltage during charging and boost it during discharging. Its low component count and simplicity allow for high reliability and low cost [23].

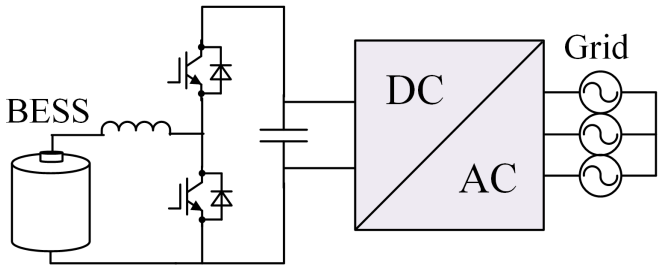

Figure 2.4: Half-bridge topology for BESS interface [23, 27].

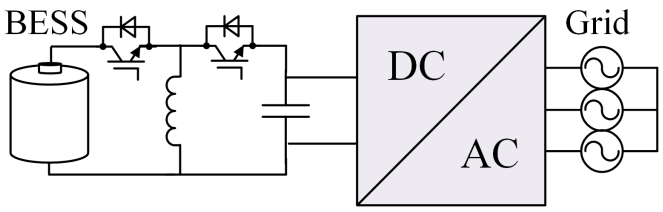

Figure 2.5: Buck-boost topology for BESS interface [23].

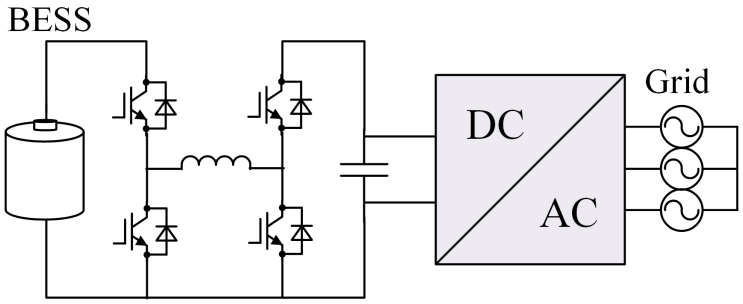

Figure 2.6: Buck-boost cascaded topology for BESS interface [23, 27].

The bidirectional buck-boost converter in Fig. 2.5 is similar to the traditional buck-boost in that it can step up or step down voltage in either direction. Its topology is simple and it has a low component count like the half-bridge, but it also has an inverted output voltage like the traditional buck-boost. The bidirectional buck-boost cascade converter consists of the traditional buck and boost topologies cascaded together as shown in Fig. 2.6, and it also bucks or boosts voltage in either direction. It has more components than the bidirectional buck-boost, but the components experience less stress, the inductors and capacitors can be smaller, and the output voltage is not inverted [23].

The bidirectional Ćuk converter (Fig. 2.7) likewise provides both step up and step down capability, and offers continuous input and output current with reduced ripple. However, its inductors and transfer capacitor must be large, and its output voltage is inverted. The SEPIC/Luo converter (Fig. 2.8) functions like a SEPIC during charging and a Luo during discharging, and it has similar step up and step down functionality without an inverted output voltage. Its passive devices are also comparatively large, and its output current is discontinuous [23].

A dual-active bridge (DAB) is the most common isolated topology, and it can be cascaded with a buck-boost converter to optimize its operating point. The DAB provides galvanic isolation

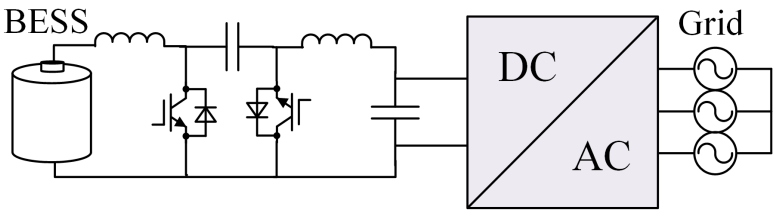

Figure 2.7: Ćuk topology for BESS interface [23, 27].

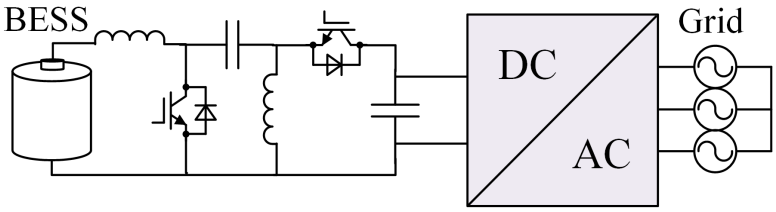

Figure 2.8: SEPIC/Luo topology for BESS interface [23, 27].

between the batteries and the DC link using a small, high frequency transformer that can also be used to provide extra boost capability, as shown in Fig. 2.9. The bi-directional buck-boost keeps the DAB input voltage constant so that the DAB can work at a single operating point with maximum efficiency [23]. Although it has several more components than other topologies, industrial standards may require topologies with isolation in the future since batteries are sensitive to overcurrent [23, 27, 62]. One alternative to the DAB is the dual half-bridge (DHB) (Fig. 2.10), which uses half as many devices as the DAB but requires higher device current ratings and large DC capacitors [23].

Double stage topologies have several advantages over single stage topologies. The addition of a DC-DC converter is beneficial in that it boosts the battery bus voltage up to the necessary grid voltage, which allows the battery strings to be lower voltage and therefore shorter. A DC-DC converter stage also allows for a distributed configuration of storage elements connected to the same DC bus, which is beneficial for independent control of each element and compensation for impedance differences in each. Also, the DC-DC converter can serve as a protection device for the batteries and can help prevent low-order harmonics from reaching them. The primary disadvantage of double stage topologies is an increased number of circuit devices and complexity [23, 62].

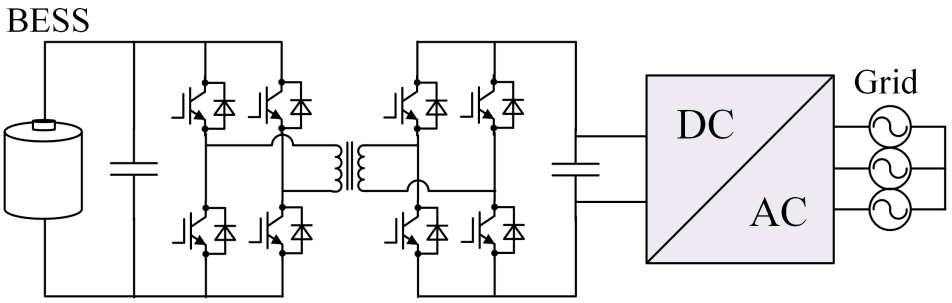

Figure 2.9: DAB topology for BESS interface [23].

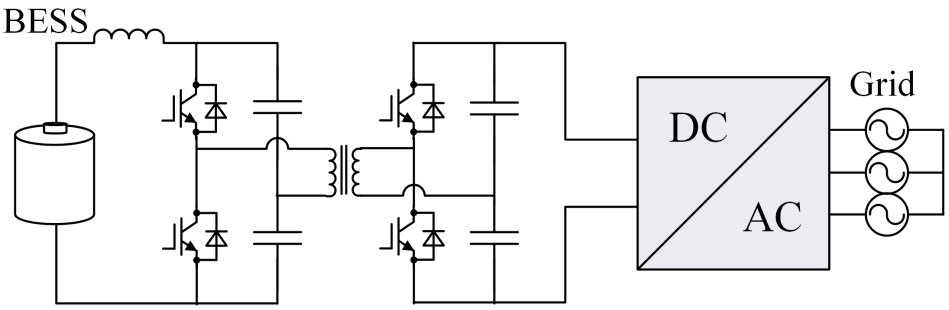

Figure 2.10: DHB topology for BESS interface [23].

Multilevel Topologies

Multilevel converters create desired AC voltage waveforms by combining multiple levels of DC voltages, and they are very common in high voltage applications since the voltage blocking requirement of devices is significantly reduced [23]. This configuration works well with battery storage because different battery strings can compose each voltage level.

Cascaded H-bridge converters (CHB) are composed of series-connected units, and each unit contains its own H-bridge converter and DC source as shown in Fig. 2.11. This nearly eliminates the reliability concerns associated with series-connected battery strings, as strings are very short in CHBs even if multiple battery modules are used in the same unit for large systems. Each phase leg of the CHB adds up to the line voltage of the greater power system, so no transformer is required. The power electronics in each cell regulate the power flow to and from their attached battery modules, and a common zero sequence voltage can be used to transfer energy between phase legs. CHBs can be used to implement fault tolerant control as well as SOC balancing of battery modules [23, 62]. The H-bridge in each cell can be single stage, double stage, or isolated

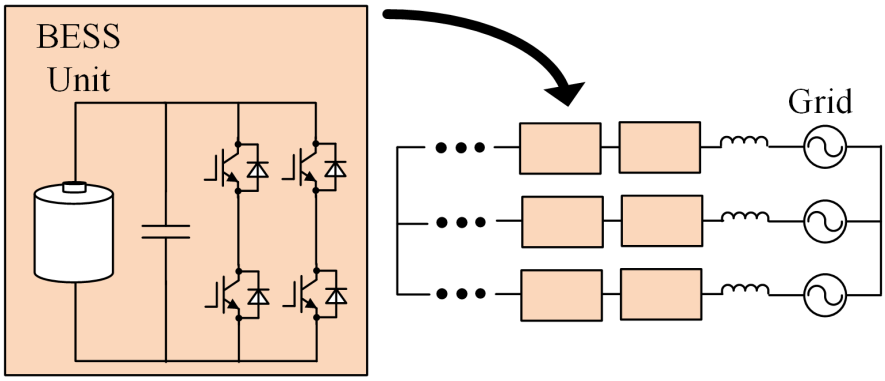

Figure 2.11: CHB topology for BESS interface [62].

like any centralized converter for BESSs. [23]. The CHB's advantages include use of low-voltage switches, use of a low switching frequency, and high output voltage quality resulting in minimal filtering requirements. However, it requires a high number of switches, and their inherent cost, power losses, and reliability issues are disadvantageous in comparison to conventional converters [63].

In a traditional neutral point clamped converter (NPC), the battery voltage is divided into multiple layers by a series-connected string of diodes. These diodes need voltage balancing, so active switches are often used instead of diodes so that the switching sequence can be optimized for even loss distribution. Flying capacitor converters (FC) are similar to NPCs but use capacitors to divide the DC voltage instead of switches [23, 62].

The modular multilevel converter (MMC) is a merge between the CHB and the FC, and it is displayed in Fig. 2.12. It uses the same distributed approach as the CHB, and its units typically contain a half-bridge and an inductor. In a MMC, the battery modules can be connected to a central DC link or they can be distributed with circulating current between phase legs that can be used for SOC balancing. Like the CHB, the converters in each unit can be single stage, double stage, or isolated. However, the MMC constitutes added complexity compared to the CHB since it has six arms instead of three, so the CHB is typically more suitable for BESSs than the MMC [23, 62].

The CHB and the MMC are both modular, which gives them excellent management of large-scale systems in terms of bypassing certain battery modules when necessary. However, they both have a very high number of devices, and they do not prevent harmonics in the current ripple from

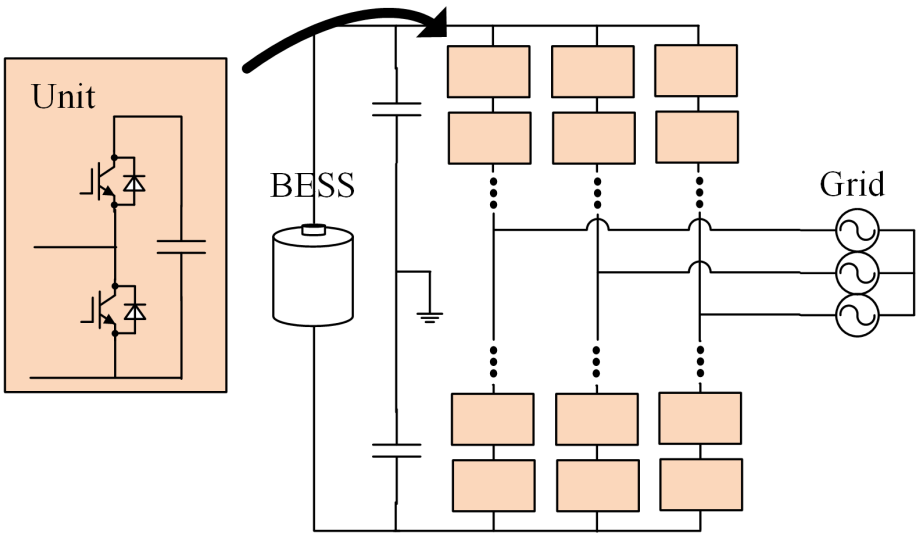

Figure 2.12: MMC topology with centrally-connected architecture for BESS interface [62].

flowing through the batteries. The NPC is low in cost and high in efficiency, but it permits unequal loss distribution in the devices. The active NPC solves this problem with active devices and hence has a higher number of components. The FC is excellent at equal loss distribution, but its DC link capacitors must be very large and controlling the capacitor charge adds complexity [23].

Multilevel topologies operate at a reduced switching frequency compared to conventional topologies, and they have lower device rating requirements and often lower output voltage distortion. Modular topologies like the CHB and MMC have lower manufacturing costs, better balancing among battery modules, and redundant levels can be installed for increased reliability. During operation, the CHB and MMC produce excellent waveform quality, which reduces the need for a filter at their point of common coupling with the larger power system. However, CHBs and MMCs face limitations with correcting grid asymmetries since doing so usually requires unequal charging or discharging of the battery modules [62]. Also, multilevel converters generally have higher costs than traditional topologies due to their higher numbers of devices, even though the voltage rating requirements of those devices are lower [23].

Topology Comparisons

Topologies with line-frequency transformers have far more power loss than transformerless designs. However, DC-DC converters produce significant losses also, so the most efficient topologies are typically the CHB and MMC. Although they are lossy, DC-DC converters have the advantage of regulating battery operation so the AC-DC converters can operate with a constant DC bus voltage irrespective of battery type or conditions. They can also serve as an additional layer of protection for the battery modules from lower order harmonics [62].

2.3 Internal Battery Modeling

Battery models describe how various battery behaviors change during operation. For battery models, there exists a steep trade-off between accuracy and simplicity. The most accurate models are often far too complex or computationally-heavy, and the simplest models tend to have large error [28]. The parameters for battery models are typically obtained either from manufacturer datasheets or experimentally [27, 64, 65].

There are several factors that affect the dynamic behavior of a battery. A battery's open-circuit voltage changes nonlinearly as its SOC changes. When a step change event in load occurs, a battery exhibits a transient response that contains voltage drops with different time constants. In long term applications, the usable capacity of a battery decreases with cycle number and/or storage time [66]. Model selection depends on the fidelity needed for the specific characteristics of the battery that are relevant to the application [64]. If the advantages of multiple model types are needed, models can also be combined [64, 66, 67, 68].

2.3.1 Common Battery Model Types

Electrochemical models such as [33] are precise representations of the chemical reactions taking place within a battery, and for that reason they are the most accurate models [64]. These models are often used during the design process for batteries so that the design characteristics of their electrodes and electrolytes can be optimized. However, an electrochemical model typically

contains a system of coupled and time-varying partial differential equations, which require substantial computation capability and/or time [27, 30, 59, 65, 66, 67, 68]. Also, the parameters for electrochemical models are usually not obtainable from manufacturers and therefore require experimental acquisition [33, 67].

Mathematical models employ stochastic strategies or empirical equations to forecast system runtime, efficiency, and capacity. These models are simple, but their error is often 5-20% and they provide no information on internal battery parameters or voltage-current characteristics. Thus, mathematical models can be quite useful for system-level designers but are too abstract for use with circuit simulation [27, 65, 66, 67, 68].

Electrical models are between electrochemical and mathematical models in terms of accuracy and complexity. They are the most logical choice for use with circuit or grid-level simulations, as their I-V characteristic error is usually only 1-5% [28, 30, 65, 66, 67, 68]. Electrical models are composed of voltage sources, current sources, resistors, and capacitors, which make them easy to simulate with other circuit-based systems [65, 66]. They can be either static or dynamic, and they can be categorized into simple models, Thevenin models, impedance models, and runtime models [27, 66, 67, 68]. These models are explained in detail below.

In each of the electrical models, the most common way to track the SOC is by current integration [64, 69], which experiences drift in practice but is acceptably accurate for short durations [64]. SOH is often measured by the degradation of certain battery parameters due to aging [65]. The fidelity of most models explained below could be further improved by consideration of temperature, current direction, and capacity fade.

Simple Models

The ideal model for a battery is a simple voltage source, but this accounts for only the battery's nominal voltage and no other characteristics [27, 28, 54]. A simple linear circuit model contains a voltage source representing open-circuit voltage and an equivalent series resistance (Fig. 2.13). This model does not consider the dependence of the open circuit voltage or internal resistance on

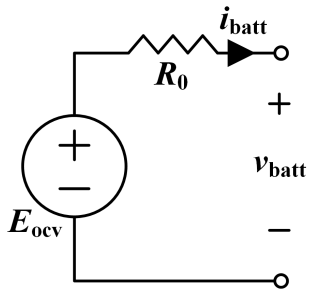

Figure 2.13: Linear battery model [28, 64, 70].

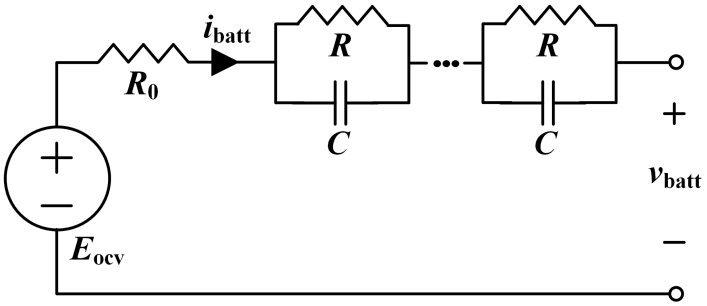

Figure 2.14: Thevenin battery model [64, 70].

SOC, so it is only useful in applications where battery capacity is assumed to be infinite or SOC is unimportant [27, 28, 64, 65, 70].

The linear circuit model can be improved by allowing the open circuit voltage and/or the equivalent series resistance to change with the battery's SOC, which adds an additional degree of fidelity and makes the model more practical. A dynamic battery model can bring even more accuracy by using mathematical equations to account for nonlinear characteristics in the open circuit voltage and/or the equivalent series resistance as functions of other internal states [65, 70].

Thevenin Models

Variations of the Thevenin model are the most commonly used models for battery applications. The simplest Thevenin models use a constant open-circuit voltage, a constant equivalent series resistance, and one or more RC networks to model the battery's response to transients at a particular SOC as shown in Fig. 2.14 [27, 28, 30, 56, 64, 67, 68, 70]. This response is due to charge depletion and recovery, which have to do with dispersing concentrated reactants around

the electrodes when current begins and diffusion of reactants back to the electrodes when current ends, respectively [64]. Adding additional RC networks increases accuracy, but typically only one or two are necessary [64, 67, 68]. Because this model is only authentic for one SOC level, its usefulness increases tremendously if the dependence of each parameter on SOC are modeled [28, 64]. Parameters for Thevenin models can be obtained using pulse testing or impedance spectroscopy [64, 67, 68].

Impedance Models

Traditional impedance-based models employ electrochemical impedance spectroscopy, which measures the battery's small-signal response to a range of low-frequency current injections. The result is an AC-equivalent model in the frequency domain, which is then used to determined the equivalent time-domain circuit network necessary to model the battery's impedance spectra [56, 64, 65, 66]. The positive and negative electrodes are modeled separately, and the final model for each half-cell typically contains a resistor, an inductor, and the impedance network in series as shown in Fig. 2.15 [64, 65].

The impedance-fitting process is very complex, so nonlinear least-squares fitting algorithms are usually used for creating the electrical impedance network [64, 65, 66]. The resulting model is only applicable to one SOC level and temperature setting, so traditional impedance models are typically used for SOC or SOH estimation instead of battery simulation [56, 64, 65, 66, 67, 68].

High-frequency impedance models can be used for studying the battery's response to current ripple, which should be considered when designing the passives and control for connected power

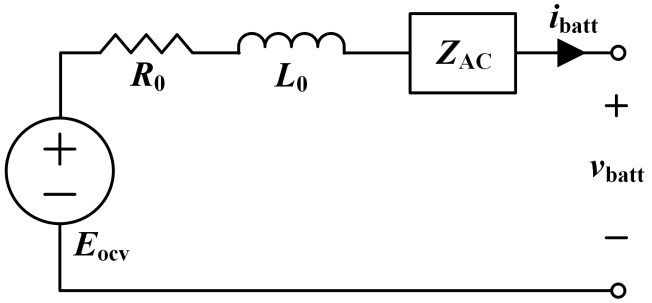

Figure 2.15: Impedance-based battery model [64, 65].

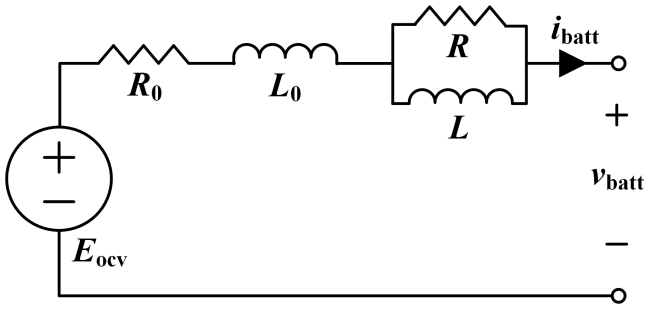

Figure 2.16: High frequency battery model [71, 72].

electronics. Current ripple must be absorbed by the battery and surrounding passives, and the amount absorbed by each depends on the impedance of each at the specific switching frequency. The impedance of a battery depends on various internal states as well as current level, but batteries appear to be almost entirely inductive at frequencies close to converter switching frequencies. For frequencies above several kHz, a battery's frequency response tends to be linear and can therefore be modeled by a single pole. As frequency rises, inductance decreased and resistance increases, which an additional R-L pair can model as shown in Fig. 2.16 [71, 72].

High-frequency impedance models only focus on converter switching frequency ranges and are therefore only valid at those frequency levels. They are created using current ripple testing, which provides information about the battery's intrinsic inductance at a specific frequency. While typical battery models contain several capacitive components, high-frequency impedance models contain primarily inductive components [71, 72].

Runtime Models

Thevenin models and impedance models are poor at predicting battery runtime. Runtime models are used for simulations of battery runtime and voltage, typically for cases in which the discharge current is constant since runtime models become less accurate as load currents vary [56, 65, 66, 67, 68]. Runtime models contain three parts: an RC network to mimic transient behavior, an RC network with dependent voltage and current sources to model losses, and a dependent voltage source with a series resistance to model terminal behavior [65].

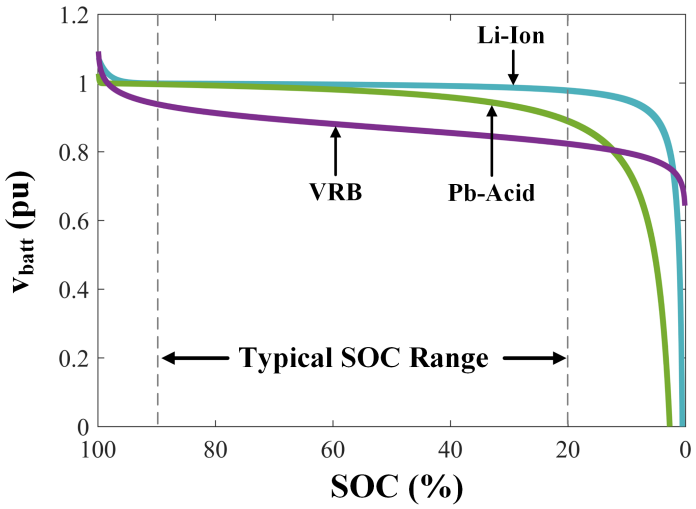

Figure 2.17: Characteristic voltage vs. SOC polarization curves for various battery technologies [30, 73, 74].

2.3.2 Technology-Specific Models

The characteristic voltage vs. SOC discharge curves for Li-Ion, Pb-Acid, and VRB batteries (assuming constant current) is shown in Fig. 2.17. When close to 100% SOC, the battery experiences a sharp rise in voltage as part of what can be referred to as its exponential zone. Then, the battery voltage stays close to its rated voltage throughout most of its typical SOC range, and it begins to drop very quickly when the SOC decreases below 20% [73, 74]. This curve also moves upward and downward as current level varies due to polarization, and most battery models lose integrity as the SOC approaches 0%.

Lithium Ion and Lead Acid Battery

Conventional battery types are the most widely modeled, and most models can be used for multiple battery chemistries with only slight parameter changes since the current-voltage behaviors of conventional batteries are so similar.

A dynamic battery model that mimics terminal voltage, open circuit voltage, internal resistance, discharge current, and SOC behavior during both charging and discharging was proposed in 1965 and became known as the Shepherd model. This model had a current-dependent term that

accurately described how voltage varies nonlinearly with current and battery charge, but this term often creates an algebraic loop in simulations [73, 75]. Thus, a revised model that accounts for this voltage variation based on only battery charge was proposed in 2007 and has become one of the most popular battery models used in literature [73].

The behavior of the battery across its voltage vs. SOC curve can be modeled as a controlled voltage source and a series resistance [73]. The controlled voltage source is modeled as a first order dynamic system with the battery's charge as its state variable. A mathematical function for replicating manufacturer-provided voltage curve behavior during discharge is equation 2.1, which models the battery's terminal voltage as a function of capacity (J), total charge discharged ($\int idt$), nominal open-circuit voltage (E_{ocv}), series resistance (R_0), polarization constant (K), exponential zone amplitude (A), and inverse exponential zone time constant (B).

$$v_{batt} = E_{ocv} - R_0 i_{batt} - \overbrace{K\frac{J}{J - \int idt}\int idt}^{\text{Polarization}} + \overbrace{Ae^{-B\int idt}}^{\text{Exponential Zone}} \tag{2.1}$$

This model is very similar to the Shepherd model, except Shepherd's polarization term that was dependent on current is now only dependent on total charge discharged (current integrated over time) [73, 74]. Because current-dependence is removed, it is really only valid for cases of constant battery current. In an improved version of this model, the polarization term dependent on total charge discharged has been split into two terms (one discharge-dependent and one current-dependent) so that open-circuit voltage behavior and voltage dependency on current level during discharge are better represented as shown in equation 2.2. The battery current is filtered when fed back into the equation, which solves algebraic loop concerns and expands the model's applicability to current-varying cases [74]. This model is shown in Fig. 2.18 and makes the following assumptions:

- Internal series resistance is constant
- Model parameters are the same for charging and discharging
- Battery capacity does not vary with current level
- Temperature and self-discharge do not affect battery behavior

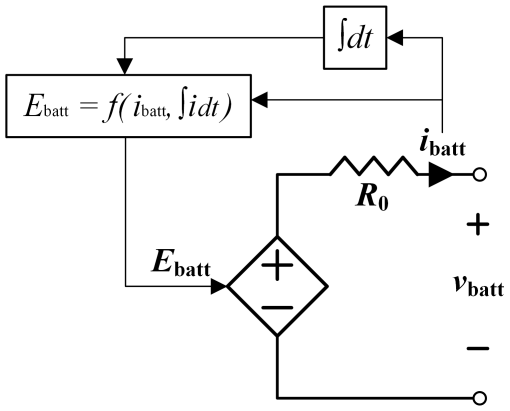

Figure 2.18: Dynamic circuit model for Li-Ion and Pb-Acid batteries [73, 74].

$$v_{batt(dis,LiIon)} = E_{ocv} - R_0 i_{batt} - \overbrace{K\frac{J}{J - \int idt}\int idt}^{\text{Polarization}} - \overbrace{K\frac{J}{J - \int idt} i_{batt}}^{\text{Polarization}} + \overbrace{Ae^{-B\int idt}}^{\text{Exponential Zone}} \tag{2.2}$$

The exact equation shown in 2.2 is used for modeling Li-Ion discharging behavior. Pb-Acid batteries experience hysteresis in their exponential zone, which is small compared to the Nickel-based chemistries that this model serves but still noteworthy. Thus, its exponential zone is replaced by a function $Exp(t)$ that describes the hysteresis behavior, with $u(t) = 0$ corresponding to discharging and $u(t) = 1$ corresponding to charging:

$$\frac{dExp(t)}{dt} = B\, i_{batt}\, (-Exp(t) + A\, u(t)) \tag{2.3}$$

Pb-Acid and Li-Ion batteries have similar open-circuit voltage characteristics when charging, and their voltages increase very rapidly when the battery approaches full charge due to polarization resistance. Polarization resistance is theoretically infinite at full charge, but this behavior has been found to occur around 90% SOC experimentally so the model's polarization resistance term is shifted accordingly. Thus, the charging voltage functions for Lithium Ion and Lead Acid are (2.4) and (2.5), respectively [74].

Table 2.1: Lithium-Ion and Lead-Acid Dynamic Model Paramters

Type	J (Ah)	E_{ocv} (V)	R_0 (Ω)	K (Ω or V/Ah)	A (V)	B (Ah)$^{-1}$
Li-Ion	2.3	3.366	0.01	0.0076	0.26422	26.5487
Pb-Acid	7.2	12.4659	0.04	0.047	0.83	125

$$v_{batt(ch,LiIon)} = E_{ocv} - R_0 i_{batt} - \overbrace{K\frac{J}{J-\int idt}\int idt}^{\text{Polarization}} - \overbrace{K\frac{J}{\int idt - 0.1J} i_{batt}}^{\text{Polarization}} + \overbrace{Ae^{-B\int idt}}^{\text{Exponential Zone}} \tag{2.4}$$

$$v_{batt(ch,PbAcid)} = E_{ocv} - R_0 i_{batt} - \overbrace{K\frac{J}{J-\int idt}\int idt}^{\text{Polarization}} - \overbrace{K\frac{J}{\int idt - 0.1J} i_{batt}}^{\text{Polarization}} + \overbrace{Exp(t)}^{\text{Exponential Zone}} \tag{2.5}$$

Parameters for this model are shown in Table 2.1. The error between simulated voltage and experimentally-measured voltage is within 5% (experimentally 3% for Li-Ion) for SOC between 20% and 100%. The precision of voltage values at SOC lower than 20% is within 10%. Thus, reference [74] claims it to be valid between 20% and 100% for Li-Ion and between 30% and 100% for Pb-Acid since it does not consider the Peukert effect. MathWorks uses this model for Simulink's battery module and adds temperature dependence to it [76].

In addition, several Thevenin models have been developed for Li-Ion and Pb-Acid batteries to better describe their dynamics [68, 77]. In general, two RC networks are used to model the multiple time constants exhibited by the battery's transient response [68]. Each parameter is typically dependent on one or more of the following: SOC, current, temperature, and cycle number [66, 68]. In sophisticated models, both runtime and current-voltage behavior can be accurately described using coupled Thevenin and runtime circuits as shown in Fig. 2.19 [64, 66, 67, 77]. The Thevenin half of these models describe transient response characteristics while the runtime component predicts battery lifetime [66]. Simulation in the Laplace domain can ease the computation requirements for parameters containing exponential and logarithmic equations [68].

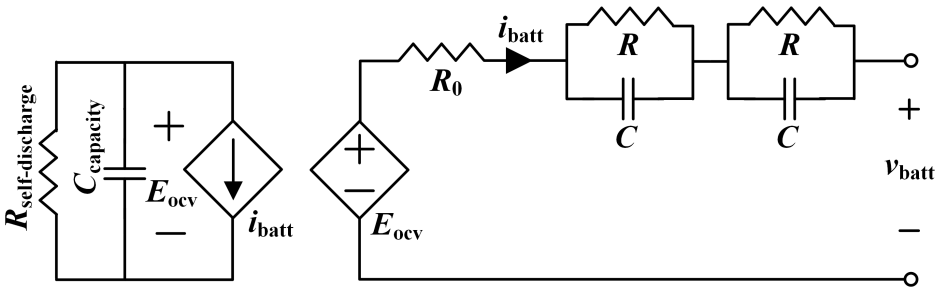

Figure 2.19: Thevenin-runtime model for Li-Ion and Pb-Acid batteries [64, 66, 67, 77].

Vanadium Redox Flow Battery

Flow batteries require different models than conventional batteries due to their flowing electrolyte [7], but most system-level electrical models assume the electrolyte flow rate to be constant [78]. For a constant flow rate, the same modeling approaches common for Li-Ion and Pb-Acid batteries are also applicable to VRB systems. Two simple models are proposed in [78] and [79]. Both of these model VRB cell voltage, but they do not consider the battery's dynamic behavior.

Thevenin electrical models that consider nonlinear battery parameters use the topology in Fig. 2.14 with one or two RC networks [30, 80]. The model in [30] proposes the circuit topology shown in Fig. 2.20 for a 15-cell, 1 kW / 1 kWh VRB system. In addition to static and dynamic behavior, this model considers shunt current, self-discharge due to diffusion, and a hydraulic circuit model for pumping system losses. The open-circuit voltage (E_{ocv}) in this model is calculated as a function of standard electrode potential (E_0), the gas constant (G), the Faraday constant (F), temperature (T), the apparent cell SOC (SOC_{cell}), and a curve-fitting coefficient (a) that accounts for differences in actual SOC and SOC calculation.

$$E_{ocv} = E_0 + a\frac{2GT}{F} ln(\frac{SOC_{cell}}{1 - SOC_{cell}}) \tag{2.6}$$

The tank SOC (SOC_{tank}) is a direct measure of vanadium ion concentration level in the electrolyte tanks, and it changes as electrons move through the cell stack. Thus, it can be calculated as a function of F, tank volume (W), and the concentration of vanadium ions in the electrolyte (c). SOC_{cell} is related to SOC_{tank} but is also dependent on the electrolyte flow rate (U).

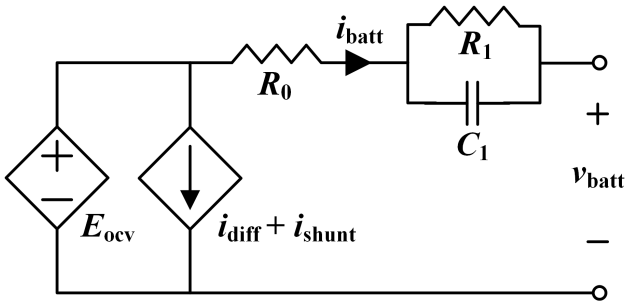

Figure 2.20: Thevenin model for VRB flow batteries [30].

$$SOC_{tank} = SOC_{tank}(0) - \frac{15}{FWc}\int_0^t (i_{batt} + i_{diff})dz \tag{2.7}$$

$$SOC_{cell} = SOC_{tank} - \frac{15}{2FUc}(i_{batt} + i_{diff}) \tag{2.8}$$

The diffusion current is the following, where the self-discharge loss (η_{diff}) is 5%:

$$i_{diff} = \frac{\eta_{diff}}{2 - \eta_{diff}}|i_{batt}| \tag{2.9}$$

Several sets of parameters for different current levels and electrolyte flow rates were obtained for this system in [30] and are shown in Table 2.2. All of the constants used in the model are displayed in Table 2.3.

Table 2.2: Vanadium Redox Thevenin Model Circuit Parameters [30]

i_{batt} (A)	U (L/min)	a	R_0 (Ω)	R_1 (Ω)	C_1 (F)
124.8	2	1.6999	0.0209	0.0085	1.16e3
124.8	4	1.4537	0.0217	0.0031	1.90e3
124.8	6	1.3364	0.0218	0.0013	4.48e3
62.4	2	1.3203	0.0222	0.0098	1.34e3
62.4	4	1.2534	0.0247	0.0044	3.77e3
62.4	6	1.2176	0.0252	0.0019	6.57e3
-62.4	2	1.3461	0.007	0.0152	1.77e3
-62.4	4	1.2738	0.0102	0.0089	2.84e3
-62.4	6	1.2471	0.0103	0.0065	4.42e3
-124.8	2	1.5531	0.0107	0.0137	1.61e3
-124.8	4	1.3921	0.0104	0.0097	1.11e3
-124.8	6	1.3491	0.0102	0.0084	1.65e3

Table 2.3: Vanadium Redox Thevenin Model Constants

E_0 (V)	G (J/(mol°K))	T (°K)	F (C/mol)	W (L)	c (M)	η_{diff} (%)
1.39	8.314	300	96487	30	2	5

2.4 Power Conditioning System Modeling and Control

The power conditioning system can be represented using average models of all power electronic converters and mathematical models of passive components. Control for the power conditioning system is heavily dependent on the power electronic topology and/or combination of topologies used. Modeling techniques and control for the power conditioning system are described in this section.

2.4.1 Passive Component Modeling

Capacitors and inductors can be modeled using mathematical equations. The mathematical models that govern voltage and current for capacitors and inductors are, respectively:

$$v_C(t) = \frac{1}{C}\int_{-\infty}^{t} i_C(t)\,dt \tag{2.10}$$

$$i_L(t) = \frac{1}{L}\int_{-\infty}^{t} v_L(t)\,dt \tag{2.11}$$

Discrete forms of these equations are:

$$v_C[x] = v_C[x-1] + \frac{i_C[x]}{C}T_s \tag{2.12}$$

$$i_L[x] = i_L[x-1] + \frac{v_L[x]}{L}T_s \tag{2.13}$$

2.4.2 Power Electronics Modeling

Power electronic converters are commonly modeled using average circuit models, which neglect switching ripple but provide information about the average DC components of waveforms. This greatly simplifies circuit analysis, which is useful for fast calculation of converter states [81].

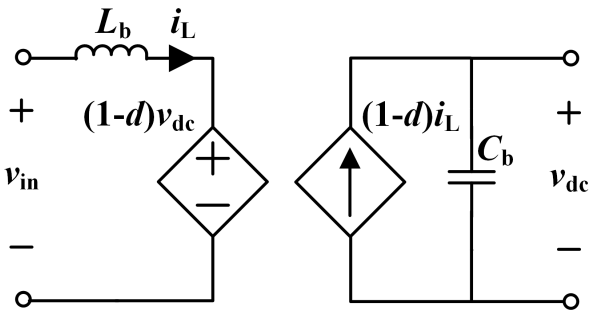

Figure 2.21: Average model of a half-bridge.

Average models utilize the average proportion of each cycle that a switch is on, which is referred to as the switch's duty cycle. With this, every switch in the converter can be modeled by a duty cycle-dependent voltage source for one side of the switch and a duty cycle-dependent current source for the other side. Then, the principles of inductor volt-second balance and capacitor charge balance are applied, which mandate that the sum of all DC components in inductor voltage and capacitor current equal zero across the switching cycle [81]. With this assumption, the average DC inductor current and capacitor voltage can be calculated. Thus, the average model for the half-bridge is shown in Fig. 2.21.

For AC-DC converters, the average model can be further simplified using the synchronous direct-quadrature (dq) coordinate system. In this system, the sinusoidal voltage and current components of multi-phase AC systems are reduced to DC-like dq coordinates as measured on a rotating dq axis. These coordinates can be found using the Park and Clarke transformations, which together create the following transformation matrix:

$$Y = \sqrt{\frac{2}{3}} \begin{bmatrix} cos(\omega t) & cos(\omega t - \frac{2\pi}{3}) & cos(\omega t + \frac{2\pi}{3}) \\ -sin(\omega t) & -sin(\omega t - \frac{2\pi}{3}) & -sin(\omega t + \frac{2\pi}{3}) \\ \sqrt{\frac{1}{2}} & \sqrt{\frac{1}{2}} & \sqrt{\frac{1}{2}} \end{bmatrix} \tag{2.14}$$

The average model of a three-wire VSI is shown in Fig. 2.22 (abc coordinates) and Fig. 2.23 (dq coordinates).

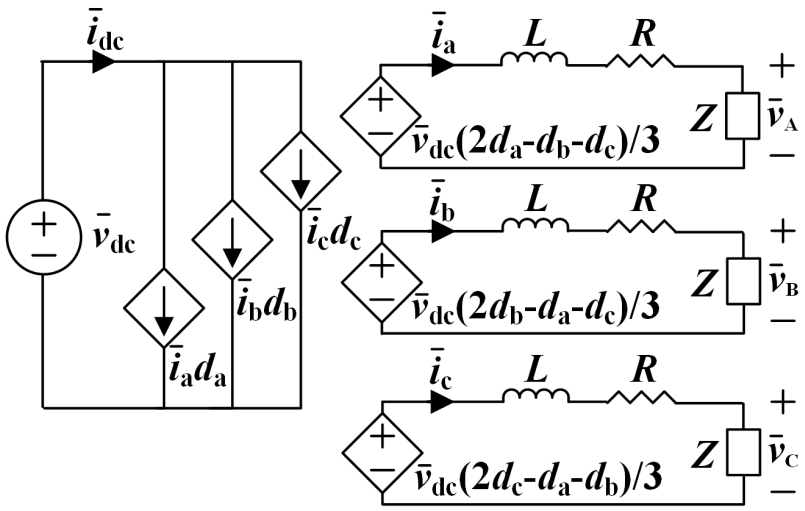

Figure 2.22: Average model of a voltage source inverter in *abc* coordinates.

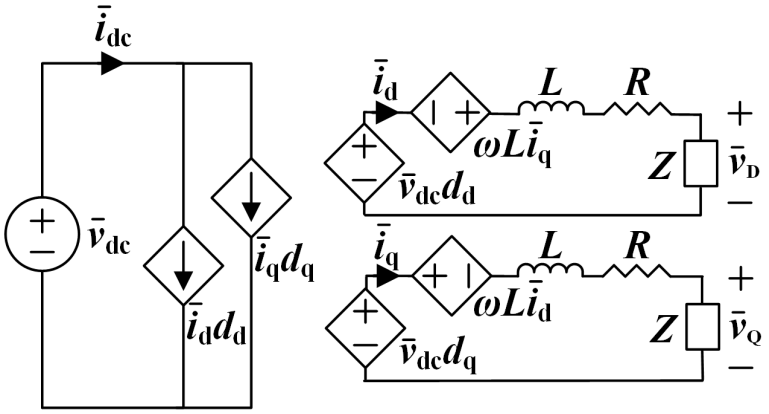

Figure 2.23: Average model of a voltage source inverter in *dq* coordinates.

2.4.3 DC-DC Converter Control

DC-DC converters can be controlled using voltage mode control or current mode control. Voltage mode control uses a single PI regulator loop to compensate for output voltage error, and it can be used with fixed-frequency pulse width modulation or phase shift modulation. For improved line regulation, a feed-forward control loop that varies the switching frequency according to input voltage changes can be added. Current mode control regulates the current through an inductor or transformer according to peak current value, average current value, or hysteretic control. Peak value control regulates the inductor peak current and the output voltage at a fixed

switching frequency, and average value control regulates the average current through an inductor or transformer with excellent noise immunity and high loop gain [23].

2.4.4 AC-DC Converter Control

All emulators on the HTB function using voltage source inverters, which convert one common DC link voltage to three-phase AC voltage waveforms. References for the AC waveforms can be generated using voltage source voltage control (VSVC), voltage source current control (VSCC), or space vector control (SVC) strategies. With VSVC, sinusoidal voltage references are created with amplitude and phase angle such that the desired interaction with the line voltage is achieved. In VSCC, an outer voltage loop provides a current reference that will result in the desired DC link voltage or AC voltage, and an inner current loop takes this reference and modulates phase duty cycles so that the output current follows and is in phase with the line voltage. However, this requires independent regulation of each phase. SVC is similar to VSCC in that it has an outer voltage loop and an inner current loop, but control is conducted in the *dq* domain so that only two references (direct and quadrature) must be controlled [23]. Voltage source inverters on the HTB use SVC.

2.4.5 Double-Stage Topology Control

Direct and quadrature references are typically created with inner current loops using proportional-integrator (PI) controllers [15, 16]. In double stage topologies, the outer loop responsible for the direct current reference typically controls the DC link voltage between the two converter stages, also with a PI controller. Since the DC link's voltage variation must be as small as possible for correct BESS operation, this loop effectively pulls out all charge flowing into the DC link from the DC-DC converter (and battery) and injects it into the larger power system as active power. With the DC link voltage kept constant, the DC-DC converter then conducts active power control on the battery modules by changing its duty cycle to achieve desired battery-side voltage [82].

The quadrature current reference in the AC-DC converter is used for reactive power control applications. When the AC-DC converter's output voltage is higher than the power system line voltage, reactive power is injected into the power system [82].

2.5 Application-Specific Control

Control for power system support functions is realized in high-level control loops that generate active and reactive power references for the power conversion system [23].

2.5.1 Primary Frequency Regulation

Primary frequency regulation must begin in the first few seconds after a frequency-altering event [11]. This is typically conducted at the local level by independent entities using proportional control. With proportional control, the power output level of a frequency regulating system is directly proportional to the error in frequency [13], as shown in Figs 2.24 and 2.25. The percentage of frequency error at which the system responds with full power output against the frequency error is referred to as slope, and it is typically 5% for generators as shown in Fig. 2.24 [11]. Primary frequency regulation methods using storage often use far steeper slopes, as shown in Fig. 2.25 [13, 69], since they are usually easier to ramp than generators. The primary frequency regulation deadband for storage can be adjusted according to how often the storage should be cycled, as frequent cycling can significantly reduce the lifetime of some storage technologies such as Li-Ion BESSs. A more complex method of primary frequency control specific to BESS adds a dependency on SOC, so the proportional parameter changes with the SOC of the BESS. This helps to protect the storage system from heavy operation at critical SOC levels [77].

During primary frequency regulation, the d-axis of an AC-DC converter interface to the power system is given priority over the q-axis in terms of power output [15]. Proportional control typically has a deadband during which the regulating system does not respond to error, which protects the regulation system from having to work constantly. Per NERC standards, this deadband is normally 0.036 Hz higher and lower than 60 Hz for generators [11, 82], but tighter deadband widths such as

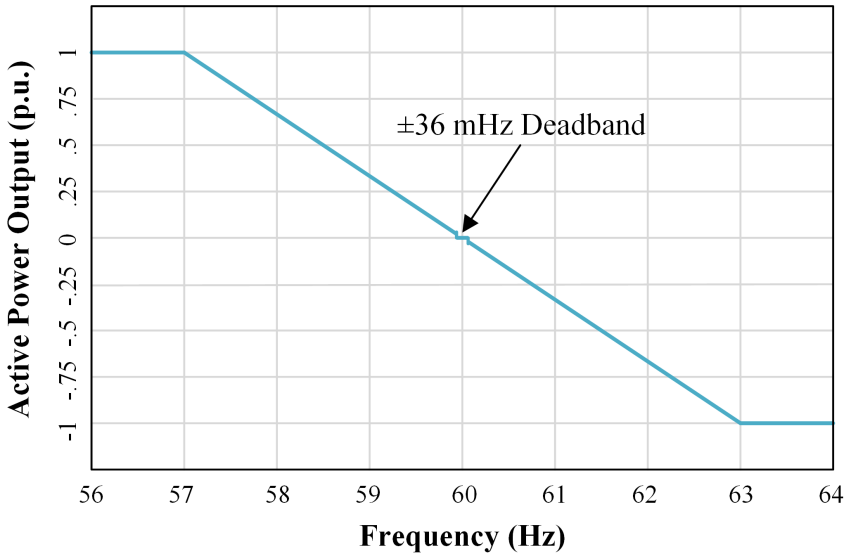

Figure 2.24: Proportional frequency control typical of generator governors [11].

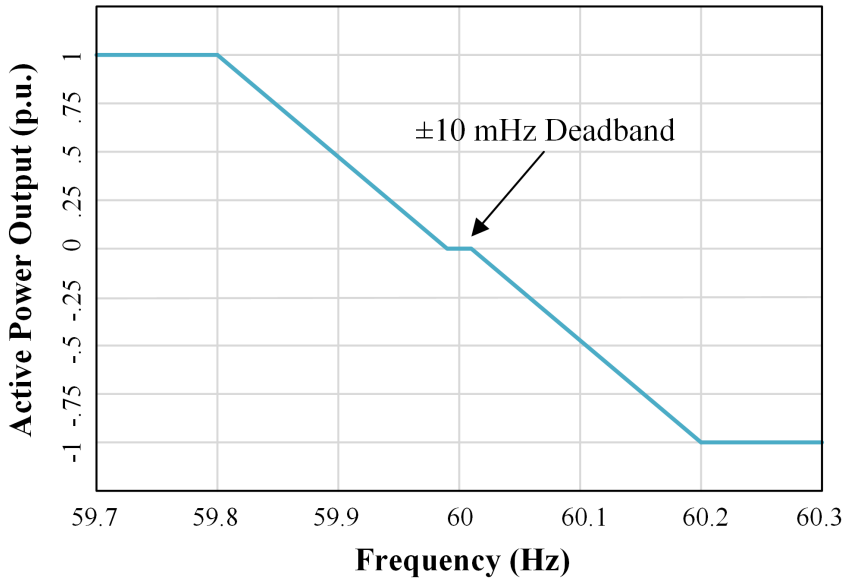

Figure 2.25: Proportional frequency control typical of storage systems [13, 69].

0.01 Hz have been used for storage so that the storage is cycled more frequently than the generators [13, 69]. Because proportional control does not have an integrator, it naturally produces a steady state error [13].

2.5.2 Inertia Emulation

The goal of inertia emulation is to slow a power system's rate of change of frequency and improve frequency oscillation damping by providing active power response to frequency changes similar to that of a synchronous generator [16]. BESS's have faster response times than conventional power plants, which makes them excellent candidates for inertia emulation [82]. Inertia emulation is typically realized through derivative control, in which the derivative of the frequency error is used along with proportional control to create an active power reference for the BESS as shown in Fig. 2.26 [12, 14, 15, 16, 32, 61]. A deadband of 0.001 Hz/s above and below zero is typical for this derivative control so that the BESS does not attempt to correct small frequency fluctuations inherent in a power system [32]. Also, a low-pass filter is typically inserted after the derivative block in the control scheme so that reaction to high frequency noise in the system is subdued [12].

For cases in which both derivative and proportional control are used, the derivative control requests higher levels of active power than the proportional control in reaction to a disturbance [12]. However, a very high gain in the derivative controller results in the BESS discharging quickly, and thus a second frequency disturbance when the battery stops discharging [15]. Also, increasing the derivative's gain beyond a certain threshold can cause stability problems for the control itself. The added low pass filter introduces a delay in the system that also affects stability, but this can only be reduced by increasing the filter's cutoff frequency and thus permitting some high frequency oscillations through the derivative control. High frequency harmonics, if seen by the derivative controller, result in very large BESS output power oscillations [16].

In literature, BESSs used for inertia emulation have had double-stage converter topologies [15, 61]. The BESS is controlled so that operation stays within the battery modules' limits, and the initial SOC is usually set to be around 50%. Since the effective utilization of the BESS's capacity

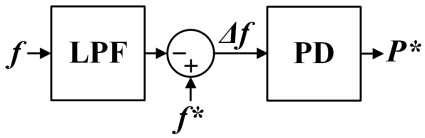

Figure 2.26: Basic inertia emulation control algorithm [12, 14, 15, 16, 32, 61].

is low when it is used for inertia emulation, it is often used for other grid services as well such as primary frequency regulation [32].

2.5.3 Voltage Support

There are a variety of methods used to support voltage in transmission and distribution systems. The most common is with an on-load tap changer, which automatically selects a tap position on a transformer in order to control the secondary side's voltage level. Other devices include step voltage regulators, switched capacitors, reactive power compensators, and inverters conducting reactive power control. More system-level strategies of controlling voltage include generator reactive power output, generator curtailment, network reconfiguration, microgrid islanding, demand-side management, and voltage-controlled energy storage [19, 83, 84, 85]. No single strategy is capable of solving all voltage issues, so power systems employ several of these devices and methodologies together [84].

Voltage support is most commonly conducted by manipulating reactive power. When a grid-tied inverter's real power conversion is lower than its rated power, its remaining apparent power can be used for reactive power injection or absorption [16, 21]. For voltage support, a controller uses the voltage error at the PCC to produce a reactive power reference for the inverter using piece-wise proportional control as shown in Fig. 2.27 [15, 16, 83]. Drawbacks to using inverter interfaces for reactive power control include high device stress, nearby voltage controllers interfering with each other, increased power losses in the line, and the inverter's active power capability not being fully realized [83].

Simple strategies for mitigating voltage problems lasting around ten minutes include the fixed reactive power, fixed power factor, power factor as a function of active power, and reactive power as a function of voltage control methods. Fixed reactive power is the simplest but requires prior knowledge of generation and load profile predictions. For fixed power factor, the reactive power injected is proportional to the active power, even though reactive power is unnecessary during periods of low real power production. Using a power factor that is a function of active power improves the high levels of loss associated with the constant power factor strategy by changing

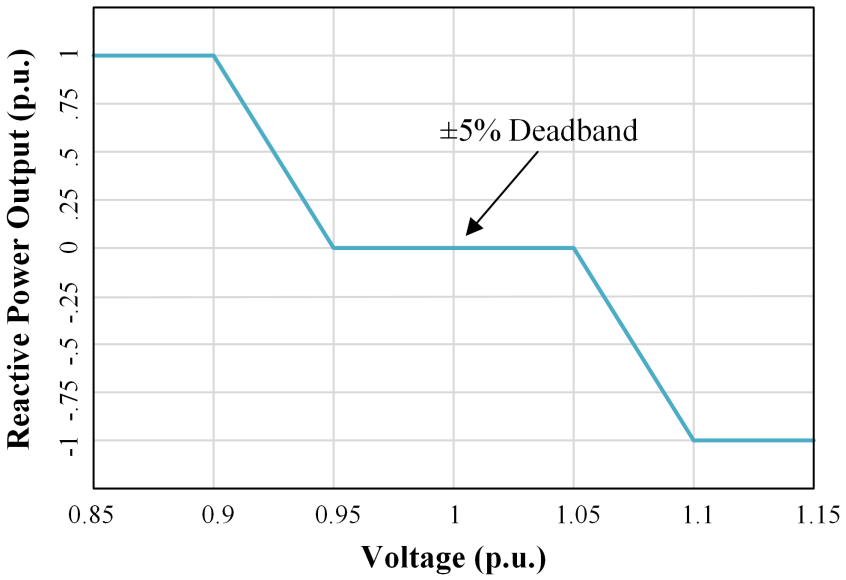

Figure 2.27: Proportional voltage support control typical of grid-tied inverters [17, 21].

the power factor to predefined constants at different active power levels. Finally, reactive power injection as a function of bus voltage directly uses line voltage information to determine reactive power needs, and this strategy is visualized in Fig. 2.27 [21].

2.6 Chapter Summary

Battery emulation has been used extensively for electric vehicle applications, and the advantages it provides are also applicable to power system applications. In addition to the battery modules, typical BESSs contain a battery monitoring system, system supervisory control, and a power conditioning system. BESSs based on flow batteries also have external storage tanks and pumping systems for the electrolyte. Electrical models for batteries are useful for power system-level analysis, and types of electrical models include simple models, Thevenin models, impedance-based models, and runtime models. Thevenin models are usually the best for studying dynamics, and several Thevenin models have been published for Li-Ion, Pb-Acid, and VRB BESSs.

The converters in the power conditioning system for the BESS can be modeled using average models, and all passive components can be modeled using their governing equations relating

voltage and current. There are multiple ways to control the power electronics depending on the number of stages used and the topologies chosen. Also, an operational BESS can be controlled to provide a number of different power systems support applications including primary frequency regulation, inertia emulation, and voltage support.

Chapter 3

Emulator Design Methodology

This chapter contains detailed documentation of the BESS emulator development process. A topology for the emulated BESS is selected, internal battery models for the specific battery chemistries are implemented, and basic active and reactive power control for the emulated BESS is designed. Then, power system support functions are added to the emulated BESS using outer power control loops. Finally, the emulated BESS is simulated in Matlab/Simulink and confirmed to behave correctly according to operator power command.

3.1 System Overview

The electrical topology shown in Fig. 3.1 was selected for the BESS emulator. The double-stage power conditioning system was deemed the most appropriate structure for the desired applications of the emulator. Having two stages allows for decoupled active and reactive power control, and the constant DC link allows the VSI to work at a single operating point. In addition, DSP implementation of a double-stage power conditioning system is simple, and the references generated for the AC-DC converter can be directly transferred to the VSI on the HTB. The cascaded H-bridge topology is popular for large-scale storage systems, but modeling and control of a cascaded H-bridge on a DSP would be far more complicated since so many more circuit components and passives are involved. Each implemented component requires computation time

on the DSP, and including all of the circuit components in a cascaded H-bridge would likely require computation time that exceeds the DSP sampling period.

Because a simple double-stage power conditioning system has been selected, the BESS is divided into power blocks with the topology shown in Fig. 3.1. Each power block is rated at 1 MW and is assumed to connect to 480 V lines in the distribution system. Thus, the DC link voltage is designed to be 900 V, and the battery storage modules are arranged so that the battery bus voltage is between 600 and 700 V. The current references for the HTB VSI are multiplied by the number of these power blocks required to achieve the desired BESS system capacity.

The final emulator control must be implemented on a digital signal processor (DSP) that controls the VSI on the HTB. The DSP has a sampling time of 100 μs, so the emulator control must be efficient enough for complete execution within that time period. The emulators on the HTB all have the same inner current control loop for the VSIs, and this loop is shown in Fig. 3.2. Thus, the final output of the BESS-specific emulator control must be direct and quadrature current references for the VSI.

3.2 Internal Battery Models

Validated models in literature were used for the internal battery models of the BESS emulator. The Li-Ion and Pb-Acid chemistries have the same model using different parameters, and the VRB system has its own separate model.

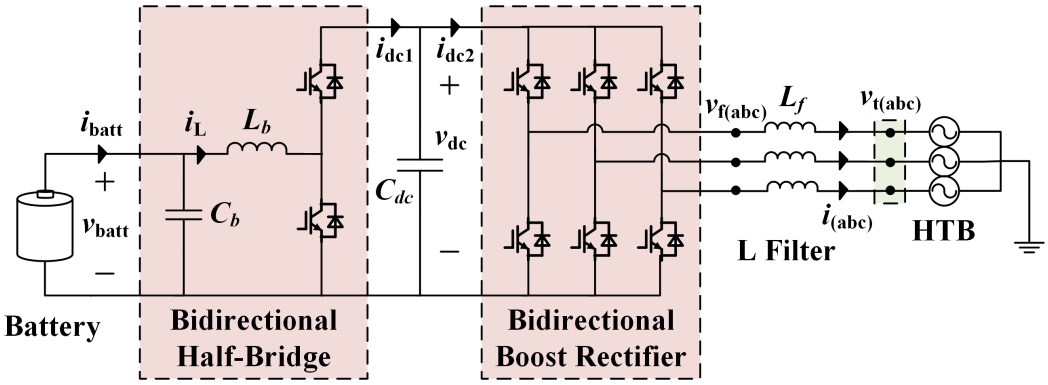

Figure 3.1: Electrical topology of emulated BESS.

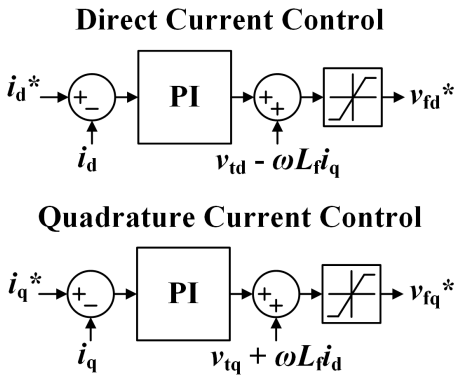

Figure 3.2: Inner current control loop for HTB inverters.

3.2.1 Lithium Ion and Lead Acid Battery Models

The dynamic battery model with polarization terms dependent on both current and total charge discharged was selected for the Li-Ion and Pb-Acid emulators. Its consideration of voltage variation due to both current and SOC gives it more authenticity across wide current and SOC ranges than the Shephard model or the SOC-dependent revised model. This model, comprised of a controlled voltage source and a series resistance, has a simple electrical structure that can be easily implemented on a DSP. In addition, it has been experimentally demonstrated to represent battery dynamics with a maximum voltage error of 5% (and lower for Li-Ion) between 20% and 100% SOC [74].

This model for the Li-Ion and Pb-Acid batteries (including hysteresis behavior) assumes the electrical behavior shown in Fig. 2.18, and its equations (2.2 - 2.5) were converted to the discrete time domain for implementation on the DSP. For this application, each equation must be a function in which the voltage applied to the battery terminals is an input and the resulting current is an output. Thus, the battery model equations were manipulated to calculate current as a function of voltage, total charge discharged, and other static battery parameters. The complete discrete discharging and charging models for Li-Ion are the following functions of capacity (J), total charge discharged ($\int idx$), nominal open-circuit voltage (E_{ocv}), series resistance (R_0), polarization constant (K), exponential zone amplitude (A), and inverse exponential zone time constant (B).

$$i_{batt(dis,LiIon)}[x] = \frac{-v_{batt}[x] + E_{ocv} - K\frac{J}{J-\int_0^{x-1} idx}\int_0^{x-1} idx + Ae^{-B\int_0^{x-1} idx}}{R_0 + K\frac{J}{J-\int_0^{x-1} idx}} \tag{3.1}$$

$$i_{batt(ch,LiIon)}[x] = \frac{-v_{batt}[x] + E_{ocv} - K\frac{J}{J-\int_0^{x-1} idx}\int_0^{x-1} idx + Ae^{-B\int_0^{x-1} idx}}{R_0 + K\frac{J}{\int_0^{x-1} idx - 0.1J}} \tag{3.2}$$

Similarly, the discharging and charging models for Pb-Acid are:

$$i_{batt(dis,PbAcid)}[x] = \frac{-v_{batt}[x] + E_{ocv} - K\frac{J}{J-\int_0^{x-1} idx}\int_0^{x-1} idx + Exp[x]}{R_0 + K\frac{J}{J-\int_0^{x-1} idx}} \tag{3.3}$$

$$i_{batt(ch,PbAcid)}[x] = \frac{-v_{batt}[x] + E_{ocv} - K\frac{J}{J-\int_0^{x-1} idx}\int_0^{x-1} idx + Exp[x]}{R_0 + K\frac{J}{\int_0^{x-1} idx - 0.1J}} \tag{3.4}$$

where

$$Exp[x] = \frac{Exp[x-1] + ABT_s i_{batt}[x]u[x]}{1 + BT_s i_{batt}[x]} \tag{3.5}$$

Both Li-Ion and Pb-Acid systems were designed so that each battery string would have a nominal voltage between 600 and 700 V and each power block of strings would have a power rating of 1 MW assuming a current limit of 1 C. The BESS parameters selected according to these criteria are shown in Table 3.1. The values used to make these calculations were those used for the actual model, which are shown in Table 2.1.

Table 3.1: Lithium-Ion and Lead-Acid BESS Design Parameters

Type	No. Series-Connected Cells in String	No. Parallel Strings	Nominal Battery Bus Voltage (V)	Power Rating (MW)
Li-Ion	200	646	673.2	1.0002
Pb-Acid	300	1337	623.2	0.9999
VRB	450	34	625.5	1.0200

3.2.2 Vanadium Redox Battery Model

The Vanadium Redox Thevenin model detailed in section 2.3.2 was selected for the emulator primarily for its dynamic response consideration. Dynamic response is an important component of the HTB's capabilities, and simpler published models such as the alternative described in section 2.3.2 do not consider dynamics. For Vanadium Redox flow batteries, there does not yet exist a simple, non-Thevenin dynamic model like the one selected for Li-Ion and Pb-Acid.

The model proposed in [30] considers several factors in addition to the circuit model, as explained in section 2.3.2. However, due the computational limits of the DSP, only the circuit model and the additional open circuit voltage, diffusion current, and SOC equations were considered for the BESS emulator. Like with the Li-Ion and Pb-Acid model, a function for battery current was derived for use with the BESS emulator. First, the following two loop equations were written based on the circuit model, which includes series resistance (R_0), R-C pair voltage (v_1), R-C pair capacitance (C_1), R-C pair resistance (R_1), and open-circuit voltage (E_{ocv}).

$$i_{batt} = C_1 \frac{dv_1}{dt} + \frac{v_1}{R_1} \tag{3.6}$$

$$E_{ocv} = R_0 i_{batt} + v_1 + v_{batt} \tag{3.7}$$

These equations were converted to the discrete-time domain and combined to form one function for battery current as follows.

$$i_{batt}[x] = \frac{E_{ocv}[x-1] - \frac{R_1 C_1 v_1[x-1]}{T_s + R_1 C_1} - v_{batt}[x]}{R_0 + \frac{R_1 T_s}{T_s + R_1 C_1}} \tag{3.8}$$

The model's equations for open circuit voltage and internal current (i_{int}) considering diffusion were also converted to discrete forms. In addition to the aforementioned variables, these equations include temperature (T), the gas constant (G), the Faraday constant (F), and the cell SOC (SOC_{cell}). The internal current was calculated by adding together i_{batt} and i_{diff}, which uses equation 2.9.

$$E_{ocv}[x] = E_0 + a\frac{2GT}{F} ln(\frac{SOC_{cell}[x-1]}{1 - SOC_{cell}[x-1]}) \tag{3.9}$$

$$i_{int}[x] = \frac{2}{1.95} i_{batt}[x] \tag{3.10}$$

The parameters for this VRB model, which are summarized in Table 2.2, are for a 1 kW / 1 kWh system with 15 cells in series. Thus, E_{ocv} must be multiplied by 15 for use in the circuit model. The number of cells per string and the number of strings to create the 1 MW power block are shown in Table 3.1.

3.2.3 Battery Monitoring System

Section 2.2.2 explains that the BMS monitors and reports battery states such as SOC, SOH, temperature, and the voltage levels of individual battery packs. Since the HTB is designed for primarily short-term and system-level testing, long-term states such as battery SOH and internal details such as individual pack voltage levels are not necessary for the HTB. Also, since only the VRB model considers temperature, room temperature is assumed and no temperature control is implemented. Thus, the only internal state to be reported by the BMS in the emulator is SOC.

For the Li-Ion/Pb-Acid model, the BESS's SOC is estimated using current integration, as described in section 2.3.1. The battery's total charge discharged is calculated after every iteration of the battery model by performing discrete integration of the battery's current, according to the relationship shown in equation 3.11.

$$\int_0^x idx = \int_0^{x-1} idx + i_{batt}[x]T_s \tag{3.11}$$

The SOC is then calculated by subtracting this value from the battery's capacity, J, and dividing the result by the capacity.

$$SOC[x] = \frac{J - \int idx}{J} \tag{3.12}$$

The VRB model contains its own equations for calculating cell SOC, which include new variables such as tank SOC (SOC_{tank}), electrolyte flow rate (U), tank volume (W), tank concentration (c) . These are converted to the following discrete forms.

$$SOC_{tank}[x] = SOC_{tank}[0] - \frac{15}{FWc} i_{int}[x] T_s \tag{3.13}$$

$$SOC_{cell}[x] = SOC_{tank}[x] - \frac{15}{2FUc} i_{int}[x] \tag{3.14}$$

3.3 Power Conditioning System Models and Control

The power conditioning system is controlled by the system supervisory control (SSC) inside of a BESS. Thus, the DC link voltage control, active power control, and reactive power control serve the role of the SSC.

3.3.1 DC-DC Converter Model

The bi-directional half-bridge described in section 2.2.3 was selected for the DC-DC converter topology primarily for its simplicity. When the battery discharges, it behaves like a boost converter, and when power flow reverses for battery charging, it serves as a buck converter. The passive component sizes can be adjusted to match any given system being emulated. Average models do not consider ripple behavior, so the inductor L_b and capacitor C_b were set to somewhat arbitrary default values of 100 μH and 10 mF, respectively.

The average model of the half-bridge is derived by first writing the inductor's voltage equation:

$$L\frac{di_L}{dt} = v_{batt} - v_{sw} \tag{3.15}$$

If s is defined as boolean and $s = 1$ indicates that the low-side switch is on, s can be used to relate the voltage and current values on one side of the switch to those on the other side.

$$\begin{cases} \dfrac{di_L}{dt} = v_{batt} - v_{dc}(1-s) & (3.16) \\ i_{dc1} = i_L(1-s) & (3.17) \end{cases}$$

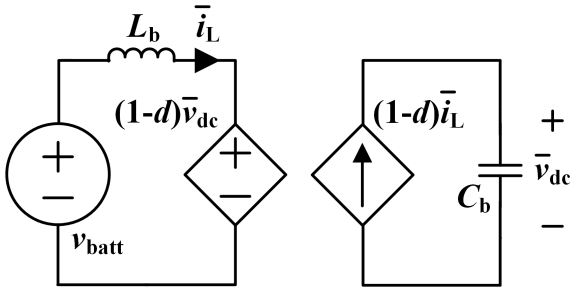

Figure 3.3: Half-bridge average model.

Across the switching cycle, the average of s becomes a switching duty cycle, so the average model is found to be:

$$\begin{cases} \dfrac{di_L}{dt} = v_{batt} - v_{dc}(1-d) & (3.18) \\ \quad i_{dc1} = i_L(1-d) & (3.19) \end{cases}$$

Thus, the average model of the half-bridge is shown in Fig. 3.3. The converter's inductor current and capacitor voltage equations in discrete time are:

$$i_L[x] = i_L[x-1] + \frac{v_{batt}[x-1] - v_{dc}[x](1-d[x])}{L_b} * T_s \tag{3.20}$$

$$v_{batt}[x] = v_{batt}[x-1] + \frac{i_{batt}[x] - i_L[x-1]}{C_b} * T_s \tag{3.21}$$

3.3.2 AC-DC Converter Model

In order for the double stage topology to function correctly, the voltage of the DC link between the DC-DC converter and the AC-DC converter must stay constant. To keep it constant, the boost rectifier was selected for the AC-DC converter topology.

For several HTB emulators, the physical VSI on the HTB is included in the emulated model so that references for the modeled AC-DC converter can be fed straight to the physical inverter. The physical inverters on the HTB have inductor output filters, which are also common at the output of BESSs as shown in section 2.2.3. Thus, it is intuitive to control the physical voltage source inverter

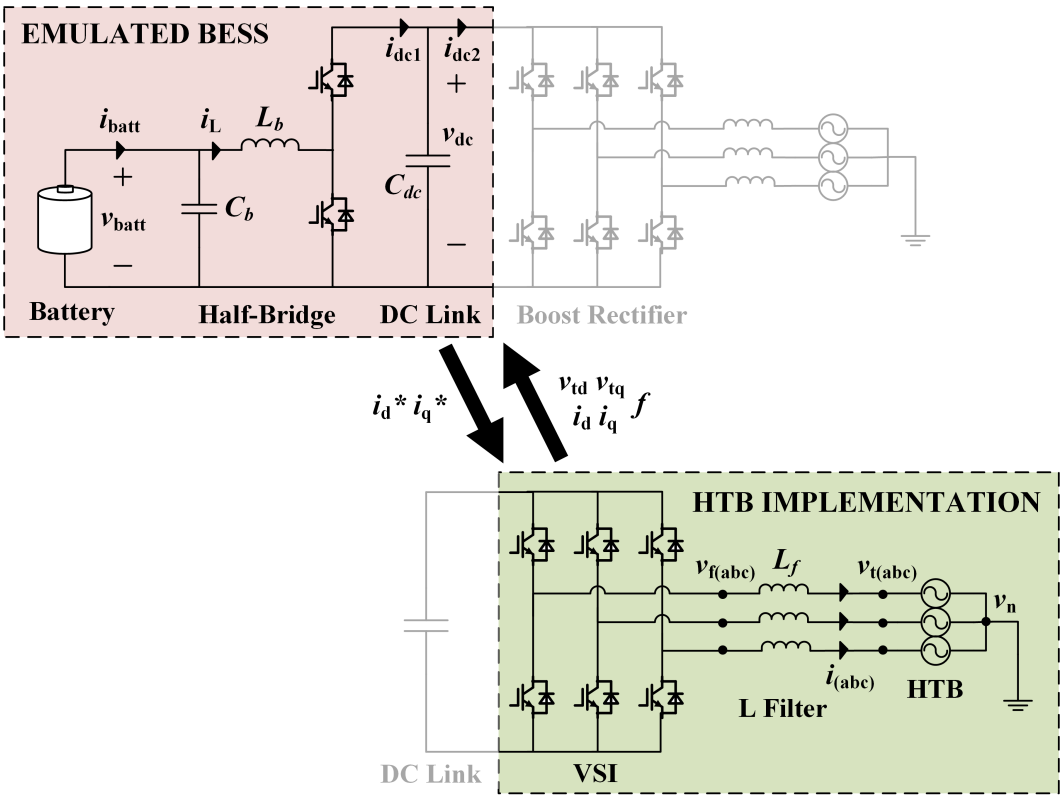

Figure 3.4: Integration of BESS emulator and HTB inverter.

on the HTB as if it were the boost rectifier in the BESS itself. Fig. 3.4 shows a diagram of how the BESS model and the physical HTB inverter are integrated.

The average model for the VSI is derived by first writing inductor voltage equations:

$$L_f \frac{d\overrightarrow{i_{(abc)}}}{dt} = \overrightarrow{v_{f(abc)}} - \overrightarrow{v_{t(abc)}} \tag{3.22}$$

If s_n is defined as boolean and $s_n = 1$ indicates that the high-side switch for phase n is on, s_n can be used to relate a certain phase's voltage and current to v_{dc} and i_{dc}. Thus, $\overrightarrow{v_f}$ can be reduced to:

$$\overrightarrow{v_{f(abc)}} = v_{dc}\overrightarrow{s_{(abc)}} - \overrightarrow{v_n} \tag{3.23}$$

$$\overrightarrow{v_n} = \frac{v_{dc}}{3}\begin{bmatrix} 1 & 1 & 1 \\ 1 & 1 & 1 \\ 1 & 1 & 1 \end{bmatrix} \overrightarrow{s_{(abc)}} \tag{3.24}$$

which combines into:

$$L_f \frac{d\overrightarrow{i_{(abc)}}}{dt} = \frac{v_{dc}}{3} \begin{bmatrix} 2 & -1 & -1 \\ -1 & 2 & -1 \\ -1 & -1 & 2 \end{bmatrix} \overrightarrow{s_{(abc)}} - \overrightarrow{v_{t(abc)}} \tag{3.25}$$

Thus, the switching model is:

$$\begin{cases} \dfrac{d\overrightarrow{i_{(abc)}}}{dt} = \dfrac{v_{dc}}{3L_f} \begin{bmatrix} 2 & -1 & -1 \\ -1 & 2 & -1 \\ -1 & -1 & 2 \end{bmatrix} \overrightarrow{s_{(abc)}} - \dfrac{1}{L_f} \overrightarrow{v_{t(abc)}} & (3.26) \\ i_{dc2} = \overrightarrow{s_{(abc)}}^T \cdot \overrightarrow{i_{(abc)}} & (3.27) \end{cases}$$

Across the switching cycle, the average of $\overrightarrow{s_{abc}}$ becomes a switching duty cycle. Thus, the average model is found to be:

$$\begin{cases} \dfrac{d\overrightarrow{\overline{i_{(abc)}}}}{dt} = \dfrac{\overline{v_{dc}}}{3L_f} \begin{bmatrix} 2 & -1 & -1 \\ -1 & 2 & -1 \\ -1 & -1 & 2 \end{bmatrix} \overrightarrow{d_{(abc)}} - \dfrac{1}{L_f} \overrightarrow{\overline{v_{t(abc)}}} & (3.28) \\ \overline{i_{dc2}} = \overrightarrow{d_{(abc)}}^T \cdot \overrightarrow{\overline{i_{(abc)}}} & (3.29) \end{cases}$$

The circuit diagram of the *abc* average model is shown in Fig. 3.5. The average model equation is transformed into dq coordinates using equation 2.14, resulting in the model shown in Fig. 3.6.

$$\begin{cases} \dfrac{d\overrightarrow{\overline{i_{(dq)}}}}{dt} = \dfrac{\overline{v_{dc}}}{L_f} \begin{bmatrix} 1 & 0 & 0 \\ 0 & 1 & 0 \\ 0 & 0 & 0 \end{bmatrix} \overrightarrow{d_{(dq)}} - \dfrac{1}{L_f} \overrightarrow{\overline{v_{t(dq)}}} - \begin{bmatrix} 0 & -\omega & 0 \\ \omega & 0 & 0 \\ 0 & 0 & 0 \end{bmatrix} \overrightarrow{\overline{i_{(dq)}}} & (3.30) \\ \overline{i_{dc}} = \overrightarrow{d_{(dq)}}^T \cdot \overrightarrow{\overline{i_{(dq)}}} \end{cases}$$

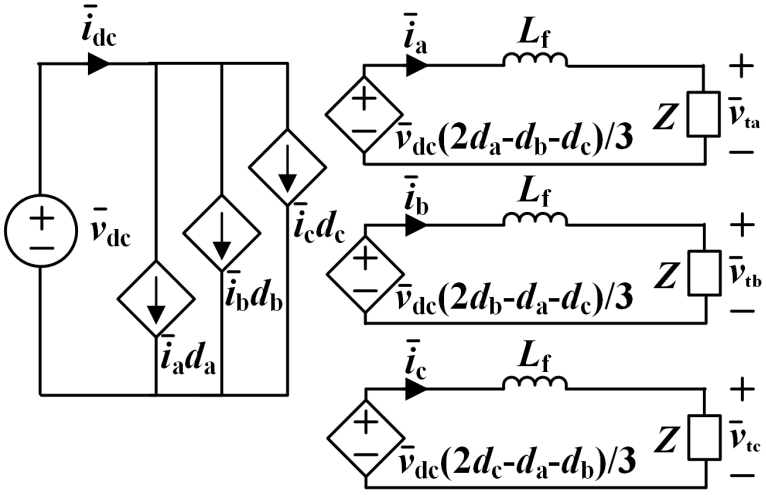

Figure 3.5: Voltage source inverter average model (*abc* coordinates).

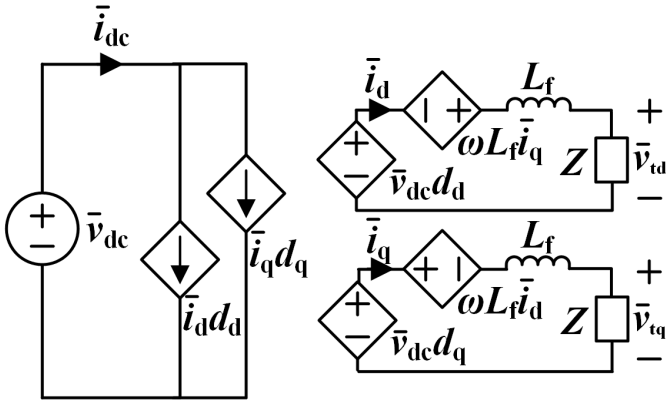

Figure 3.6: Voltage source inverter average model (*dq* coordinates).

With this average model, v_{fd} and v_{fq} are calculated using the line voltage, the inductor voltage, and the cross-coupling term voltage as follows.

$$v_{fd}[x] = v_{td}[x] + L_f \frac{(i_d[x-1] - i_d[x-2])}{T_s} - \omega L_f i_q[x-1] \tag{3.31}$$

$$v_{fq}[x] = v_{tq}[x] + L_f \frac{(i_q[x-1] - i_q[x-2])}{T_s} + \omega L_f i_d[x-1] \tag{3.32}$$

This voltage can then be used to calculate the DC current i_{dc2} with an assumption that the power entering the VSI equals the power leaving it (before the L filter) [39]. Thus, the equations necessary for for finding i_{dc2} are as follows.

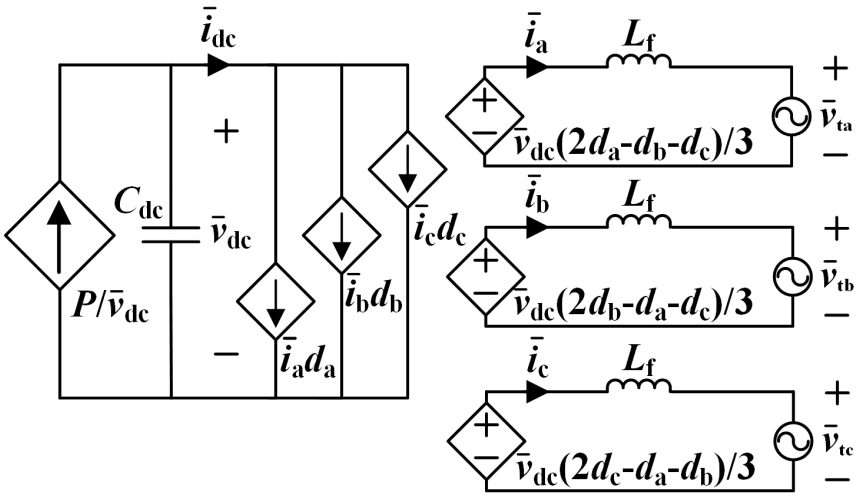

Figure 3.7: Boost rectifier average model (*abc* coordinates).

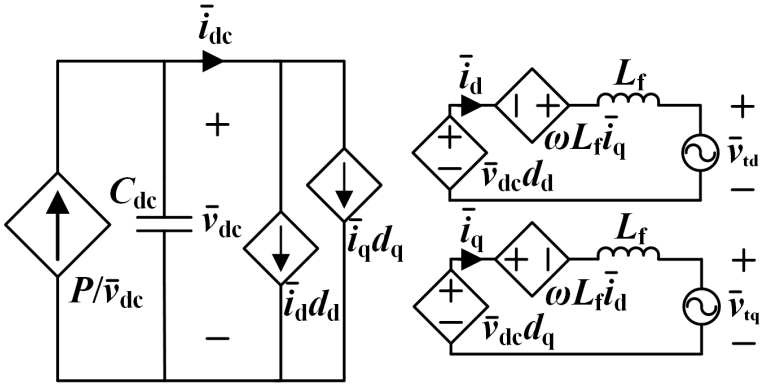

Figure 3.8: Boost rectifier average model (*dq* coordinates).

$$P_f(x) = 1.5 * (v_{fd}[x-1] i_{fd}[x-1] + v_{fq}[x-1] i_{fq}[x-1]) \tag{3.33}$$

$$i_{dc2}[x] = \frac{P_f[x]}{v_{dc}[x-1]} \tag{3.34}$$

The average models for the boost rectifier in *abc* coordinates and *dq* coordinates are shown in Figs. 3.7 and 3.8, which were derived the same way as the VSI's average models. The whole power electronics interface for the emulated BESS was implemented using the combined average model shown in Fig. 3.9, which includes the half-bridge and the boost rectifier in *dq* coordinates. All control for the power conditioning system was designed using this combined average model.

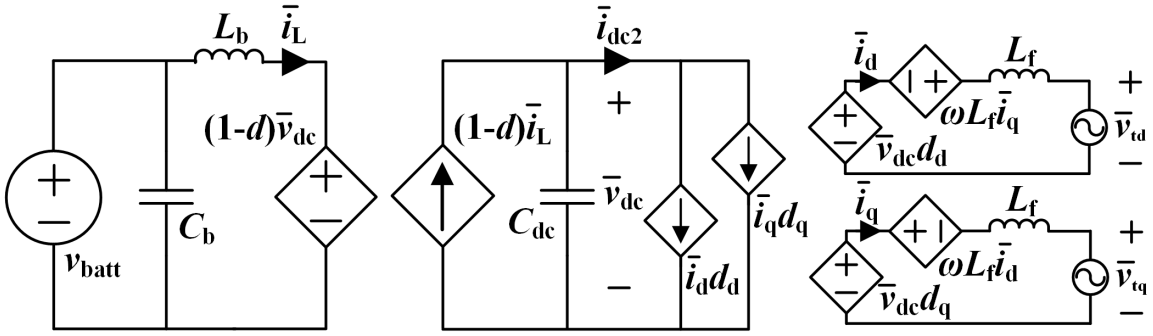

Figure 3.9: Combined average model for BESS emulator.

3.3.3 DC Link Voltage Control

The DC link voltage varies with the following equation based on i_{dc1} and i_{dc2}:

$$v_{dc}[x] = v_{dc}[x-1] + \frac{i_{dc1}[x] - i_{dc2}[x]}{C_{dc}} T_s \tag{3.35}$$

To emulate the BESS's terminal behavior, the physical VSI on the HTB is controlled like the BESS's boost rectifier, which regulates its DC side's voltage regardless of power flow direction. DC link voltage control is accomplished using the voltage source inverter's direct current reference to push and pull charge in and out of the DC link's capacitor to keep it at its rated voltage, as described in section 2.4.5. If the controller is fast enough, the current reference it generates will effectively pull out all charge right as it enters the DC link capacitor from the DC-DC converter, thus preventing the capacitor from charging or discharging.

The DC link voltage control uses a PI controller, and its complete algorithm is shown in Fig. 3.10. This loop must be the fastest among all of the BESS emulator's control algorithms besides the inner current control loop for the physical VSI on the HTB.

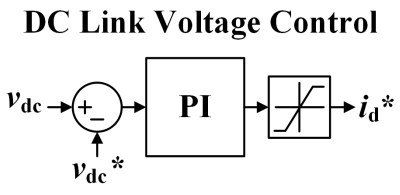

Figure 3.10: DC link voltage control for BESS emulator.

The PI controller's parameters were designed using the Matlab/Simulink single-input single-output control design tool. First, the VSI on the HTB was simulated using the average model shown in Fig. 3.6. The current control loop (Fig. 3.2) common to all current-controlled emulators on the HTB was implemented for generating the VSI's duty cycles. Then, the DC link voltage PI controller was designed using the combined average model in Fig. 3.9 to ultimately generate the current reference for the direct current control loop.

The control parameters were designed so that the controller's bandwidth would be as high as possible without causing significant overshoot in the direct current reference generated. Overshoot in the direct current reference would translate to overshoot in the BESS emulator's power output to the HTB, which would temporarily exceed the power level commanded of the BESS emulator. This would require other power system components such as generators to compensate for the swing, which is not desirable in a realistic power system.

All control parameters were designed assuming a 10 MW power system power base, a 12.5 kV power system voltage base, and a 3 MW BESS consisting of 3 1-MW blocks in parallel. The final PI control parameters for this specified system are shown in Table 3.2. When the emulated system's power and voltage bases are adjusted, the control parameters are also automatically adjusted.

3.3.4 Active Power Control

The DC-DC converter conducts active power control for the battery emulator using inductor current control, as shown in Fig. 3.11. At the input of the control loop, the active power reference and the SOC determine the future action of the battery based on power reference polarity and SOC limits. The discharging control algorithm is adopted for positive values of P^*, and the charging

Table 3.2: Control Parameters for BESS Emulator Control Loops

Control Loop	P	I	D
DC Link Voltage Control	3.1	304	–
Active Power Control	0.0015	0.0025	–
Frequency Control	0.01	–	0.1
Voltage Control	0.5	–	–

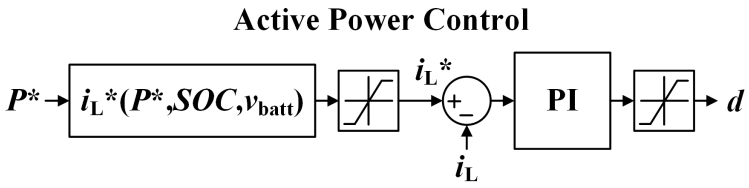

Figure 3.11: Active power control for BESS emulator.

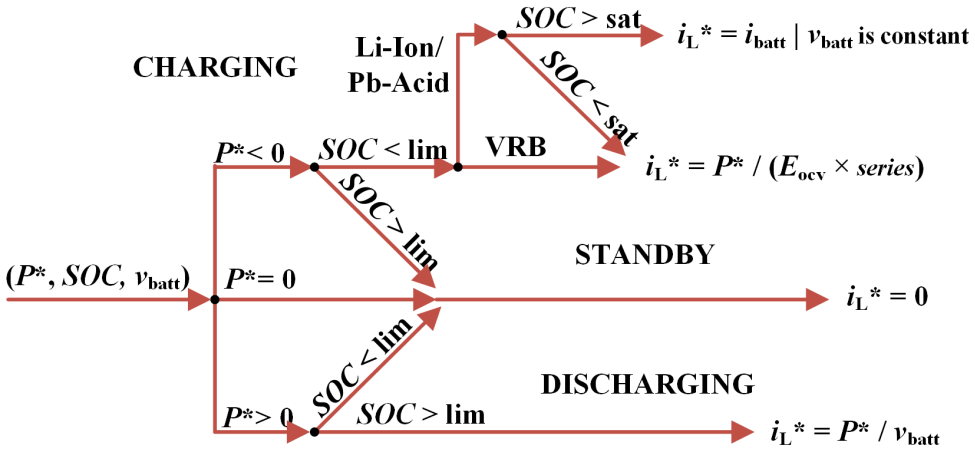

Figure 3.12: Charging and discharging algorithm for active power control.

algorithm is activated for negative values. Since the DC link voltage is assumed to be constant, a PI controller then manipulates the converter's modulation index to alter the converter's battery-side voltage. This forces the battery current (governed by the internal battery model) to essentially track the inductor current reference.

A flow chart of the charging and discharging algorithm used to calculate the inductor current reference is shown in Fig. 3.12. A constant power approach is used for discharging, so the active power command is divided by the battery's voltage to generate the inductor current reference. The lower limit for the Li-Ion and Pb-Acid batteries' SOC is 20%, and discharging is ended if that boundary is reached. The vanadium redox battery can be discharged completely, as depth of discharge does not affect its lifetime as discussed in section 1.1.2.

The Li-Ion and Pb-Acid charging algorithm has two-stages, beginning with constant current (CC) charging until the battery's SOC reaches a designated level. During this stage, the exact current used for CC is calculated by dividing the active power command by the battery's nominal

voltage, which is a constant. When the SOC reaches the designated transition point, which for this model is set to be 80% SOC, constant voltage (CV) charging begins and allows the current to drop and slowly approach zero.

The VRB charging algorithm uses a single constant current stage. Similar to the Li-Ion and Pb-Acid model, the exact current used for CC is calculated by dividing the active power command by the battery's nominal voltage.

The PI parameters for the active power control were designed the same way as the DC link voltage controller using Matlab/Simulink. The active power control parameters were designed using the single-input single-output tool on top of the same simulated model of the VSI, the inner current control loop, and the DC link voltage control loop. The Li-Ion system was assumed for design purposes, and the final control parameters (Table 3.2) were confirmed to function appropriately with the Pb-Acid and VRB systems as well. Thus, since interchangeability between emulated system parts is desired for HTB, the same control parameters are used for all three battery system types.

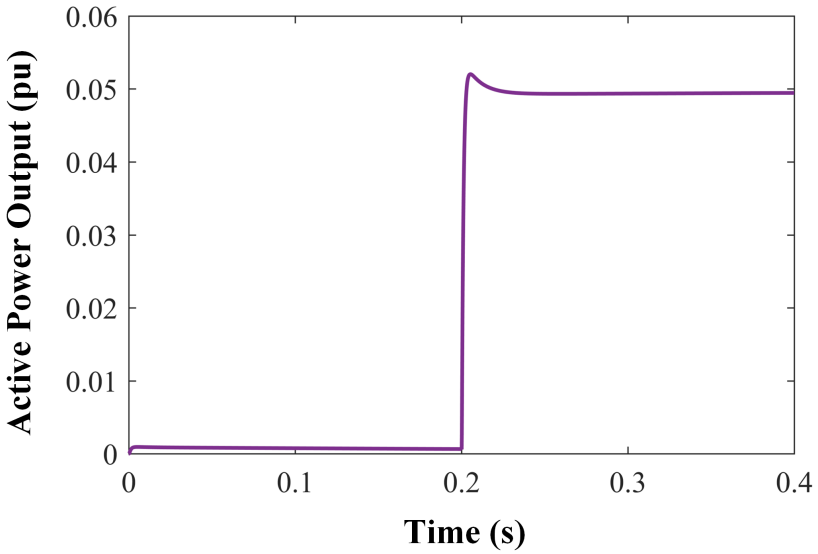

Figure 3.13: Simulated BESS response to active power command step change.

The BESS's simulated output response to an active power command step change is shown in Fig. 3.13, which includes both the active power control and the DC link voltage control. Its overshoot is less than 5% of the step change difference.

3.3.5 Reactive Power Control

The VSI's reactive power output can be controlled for power system support applications using its quadrature current reference. The VSI's quadrature current reference is generated based on a reactive power command, as shown in Fig. 3.14. The current reference (i_q^*) is calculated according to the following function of reactive power reference (Q^*), voltage between the VSI and inductor filter ($v_{f(dq)}$), and direct current (i_d).

$$i_q^*(x) = -\frac{\frac{Q^*(x)}{1.5} - v_{fq}(x-1)i_d(x-1)}{v_{fd}(x-1)} \tag{3.36}$$

The power rating S_{rating} of the voltage source inverter is assumed to be the same as that of the BESS. Thus, the active P and reactive Q power generated by the direct and quadrature current references, respectfully, must satisfy the following inequality:

$$S_{rating} \geq \sqrt{P^2 + Q^2} \tag{3.37}$$

For cases in which the active and reactive power references violate this range requirement, the active power reference is given higher priority. Thus, the reactive power reference is reduced until the inequality is satisfied.

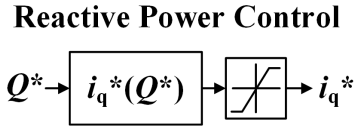

Figure 3.14: Reactive power control for BESS emulator.

3.4 Application-Specific Control

Control loops for power system support functions are added on top of the existing active and reactive power control. They generate either the active or reactive power command based on conditions of the external power system.

3.4.1 Primary Frequency Regulation

As described in section 2.5.1, primary frequency regulation uses proportional control to stabilize a system's frequency after a disturbance until secondary frequency regulation can restore it to its normal value. Thus, primary frequency regulation capability is added to the BESS emulator using a proportional control loop as shown in Fig. 3.15. If enabled, this control loop generates the active power command for the BESS emulator based on system frequency needs.

A low-pass filter is implemented at the control loop's frequency input so that the BESS does not react to noise. This low-pass filter is implemented in the frequency domain to minimize DSP computation time. Its discrete-time transfer function is the following, with a time constant (τ) of 0.6:

$$f_{LPF}[x] = \frac{2\tau - T_s}{2\tau + T_s} f_{LPF}[x-1] + \frac{T_s}{2\tau + T_s}(f[x] + f[x-1]) \tag{3.38}$$

A proportional constant of 1% is used in the control loop, which is less than the standard slope of 5% described in section 2.5.1 so that the BESS does not ramp to full power so quickly. Like typical frequency regulation, a deadband of ± 10 mHz is implemented so the BESS does not operate constantly for small fluctuations. However, a hysteretic characteristic is added to the deadband so that primary frequency regulation does not end until the frequency returns to within 8 mHz of its nominal value, even if it is within the original wider deadband. This will prevent the frequency from hovering around either the upper or lower deadband and forcing the frequency regulation to work more frequently than necessary.

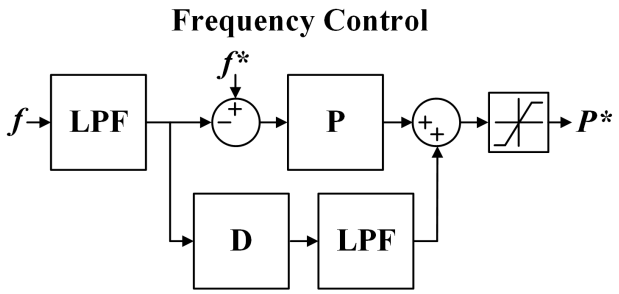

Figure 3.15: Primary frequency regulation and inertia emulation control for BESS emulator.

3.4.2 Inertia Emulation

The main purpose of inertia emulation is to slow or dampen the system-level frequency change following a disturbance. This is conducted using a derivative controller as described in section 2.5.2 since derivative controllers react according to changes in the input signal. Thus, a derivative component is added to the existing frequency controller used for primary frequency regulation. When primary frequency control and inertia emulation operate simultaneously, the output power command is a sum of their control outputs as shown in Fig. 3.15.

Derivative controllers are sensitive to input signal noise, so an additional low-pass filter was added after the calculation of the frequency error difference:

$$\Delta f_{LPF}[x] = \frac{2\tau - T_s}{2\tau + T_s}\Delta f_{LPF}[x-1] + \frac{T_s}{2\tau + T_s}(\Delta f[x] + \Delta f[x-1]) \tag{3.39}$$

It contains the same discrete transfer function as equation 3.38, and a time constant of 0.3 was used. Instead of a deadband, a threshold was implemented in the derivative controller so that it does not operate until a frequency change of more than 0.6 Hz/s is detected. After this threshold is met, the derivative controller operates for 10 seconds and then returns to its dormant state until another frequency change above its threshold is detected.

3.4.3 Voltage Support

There are multiple algorithms for conducting voltage support as described in section 2.5.3. Support using reactive power can be based on measurement of line voltage itself or just generation

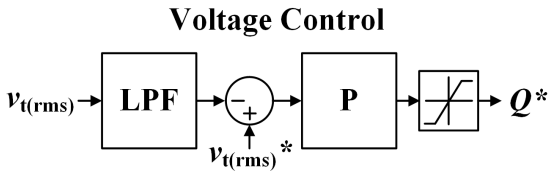

Figure 3.16: Voltage support control for BESS emulator.

conditions alone. The proportional algorithm based on line voltage was selected for this application since it provides support based on the detected needs of the system.

A simple proportional control loop (Fig. 3.16) was implemented for voltage support, and its output is an automated reactive power command. Similar to the primary frequency regulation control, it contains a deadband of 5% around the nominal voltage level. As stated in section 3.3.5, reactive power output yields to active power output when the system's capacity has been reached. Thus, voltage support is prioritized below both types of frequency control in the default setting.

3.5 Implementation

The BESS emulator is implemented in true units (not per unit) so that its empirical equations retain their forms. Before its output current references are sent to the inner current control loop of the HTB's VSIs, the current references are converted to per unit values with the same base as the power system being emulated on the HTB, such as WECC. Then, these per unit values are scaled up to HTB units using the physical HTB's power and voltage base. The same scaling in reverse must occur when current and voltage measurements from the HTB system are used in the BESS emulator. The emulator is implemented so that this scaling occurs automatically for all control parameters and measurements using the power and voltage scales specified by the user.

The default power system scale is specified for the WECC system since this will be the first application of the BESS emulator. The WECC system's power and voltage bases as well as the HTB's power and voltage bases are displayed in Table 3.3.

Table 3.3: Power and Voltage Bases for WECC and HTB Systems

Base	WECC	HTB
Power	10 GW	2 kW
Voltage	500 kV	43.833 V

Table 3.4: Functions Comprising the BESS Emulator

Name	Purpose	Variable Inputs	Internally-Stored Variables	Variable Outputs
Internal	Contains the internal battery models	v_{batt}	SOC	i_{batt}
DCDC	Contains the half-bridge converter model	M, i_{batt}	i_L	i_{dc1}, v_{batt}
DCLink	Contains the DC link model	i_{dc1}, i_{dc2}	none	v_{dc}
VdcCtrl	Controls the DC link voltage via the VSI's direct current reference	v_{dc}	none	i_d^*
PCtrl	Controls the active power output of batteries via the half-bridge's modulation index	P^*, i_L	none	M
QCtrl	Controls the reactive power output of the VSI via the quadrature current reference	Q^*, i_d^*, v_d, v_q	none	i_q^*
FreqCtrl	Conducts primary frequency regulation and inertia emulation via active power command	f	none	P^*
VCtrl	Conducts voltage support via reactive power command	$v_{t(rms)}$	none	$Q*$
HtoB	Calculates power output and rms voltage based on HTB measurements	v_d, v_q, i_d, i_q	none	P, Q, i_{dc2}, $v_{t(rms)}$

The emulated BESS is implemented using nine primary function calls that collectively govern the DSP's control output to the VSI. Their descriptions, variable inputs, and variable outputs are shown in Table 3.4. Each of these functions is executed once per DSP control cycle. If FreqCtrl or VSupport are disabled, the respective power command must come from an operator input.

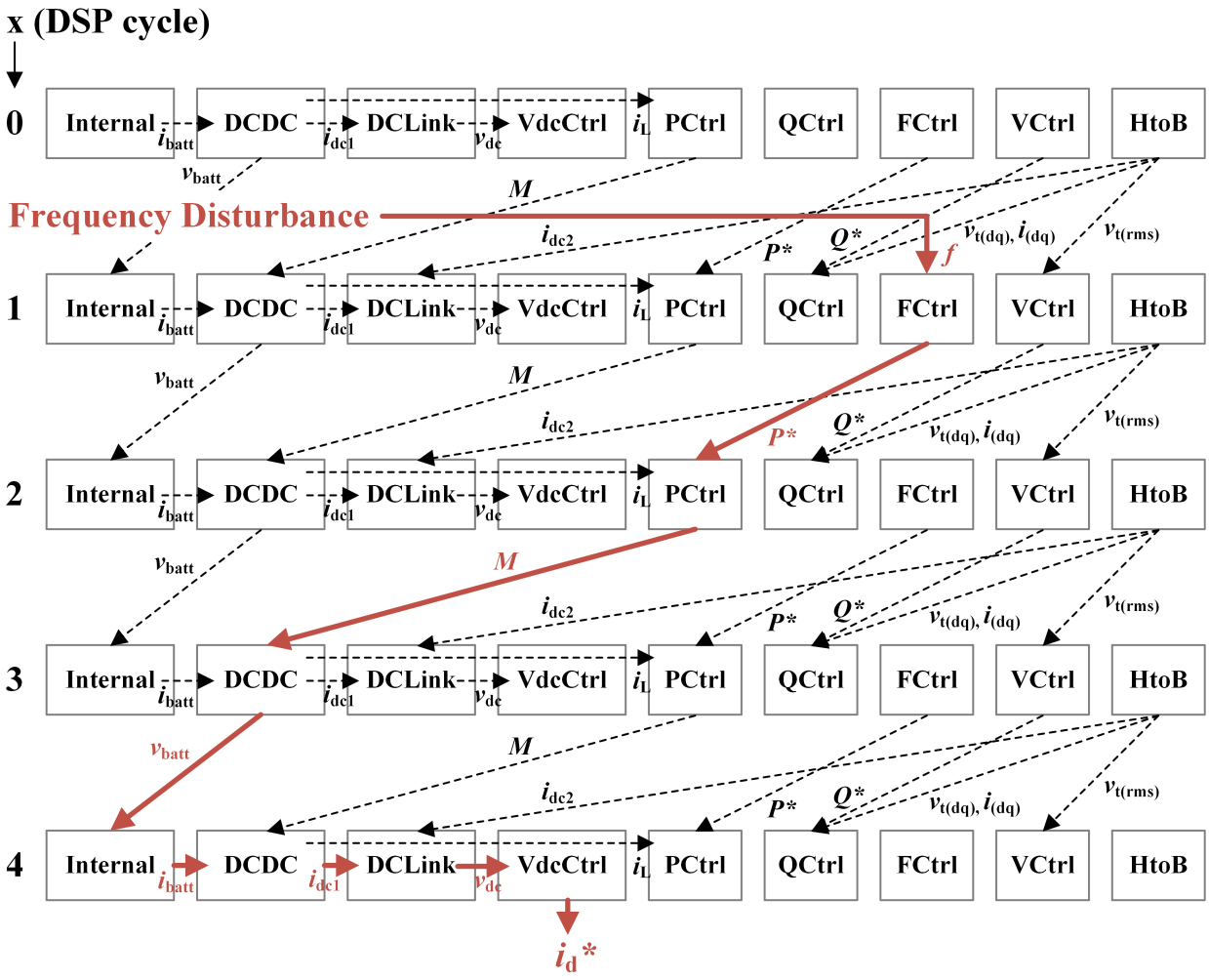

Figure 3.17: Frequency disturbance propagation through BESS emulator functions (Order 1).

If these functions are executed in the order shown in Table 3.4, a frequency disturbance reaction would propagate through the emulator's functions and eventually to the VSI's direct current reference with the path shown in Fig. 3.17. This order of execution within each cycle would require four DSP cycles before the reaction would reach the VSI.

Fig. 3.18 shows the functions reordered such that a frequency disturbance reaction would reach the HTB's VSI in the minimum number of cycles, which is two cycles. This is half of the time required by the previous order of execution. Reaction time is a major player in the effectiveness of a BESS's support during a disturbance, and this demonstrates how execution order can affect that. Thus, the latter execution order shown in Fig. 3.18 was selected for implementation on the DSP.

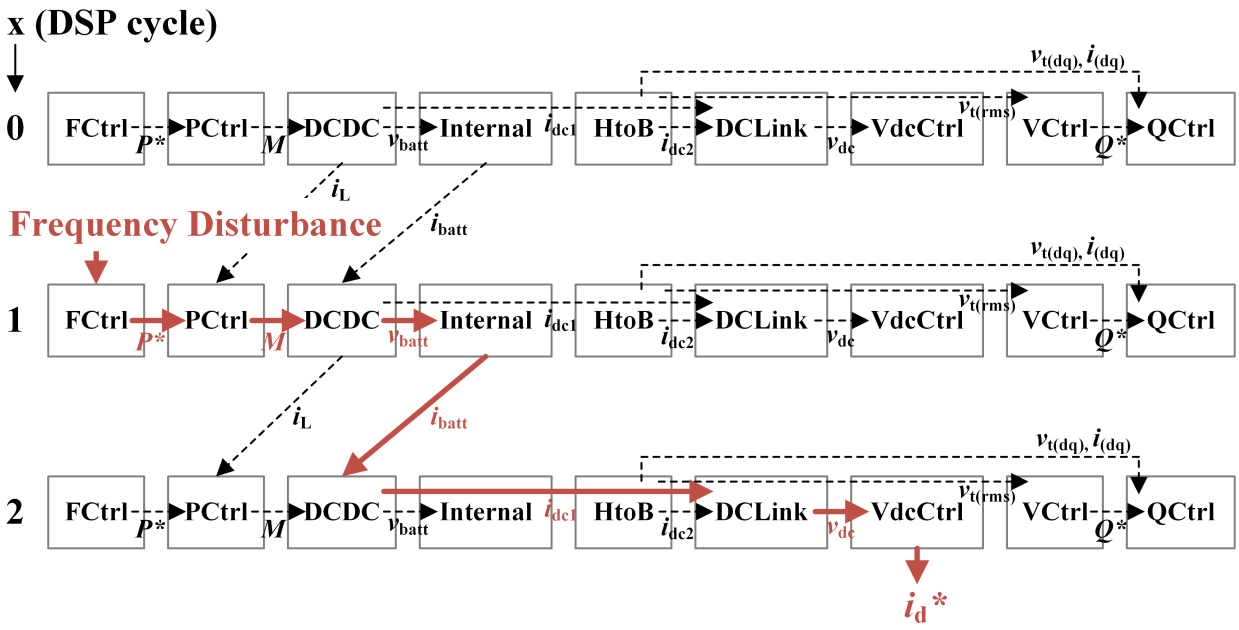

Figure 3.18: Frequency disturbance propagation through BESS emulator functions (Order 2).

3.6 Simulation

The BESS emulator was simulated in Matlab/Simulink to confirm correct behavior before implementation on the HTB. Because the Li-Ion and the Pb-Acid systems use the same model, only the Li-Ion system parameters were used during verification.

To simulate the active power control of the half-bridge converter, the battery emulator was given the following active power command step changes from an initial SOC of 60%: 0 → 0.05 → 0.07 → 0.05 → 0 → -0.05 → 0 pu. As shown in Fig. 3.19, the active power injection followed this command for both the Li-Ion and the VRB models. Throughout the duration of this testing, the DC link voltage control kept the DC voltage within 1.5% of 900 V. As the battery discharged and charged, the SOC fell with a slope that was directly dependent on the input/output power level, which was highest when the active power command was 0.07 pu. As the cell current increased, the battery's voltage decreased due to internal series resistance. The specific cell voltage drop and SOC rate of change as a result of cell current were verified to match the published waveforms accompanying both the Li-Ion and VRB models in references [30] and [74].

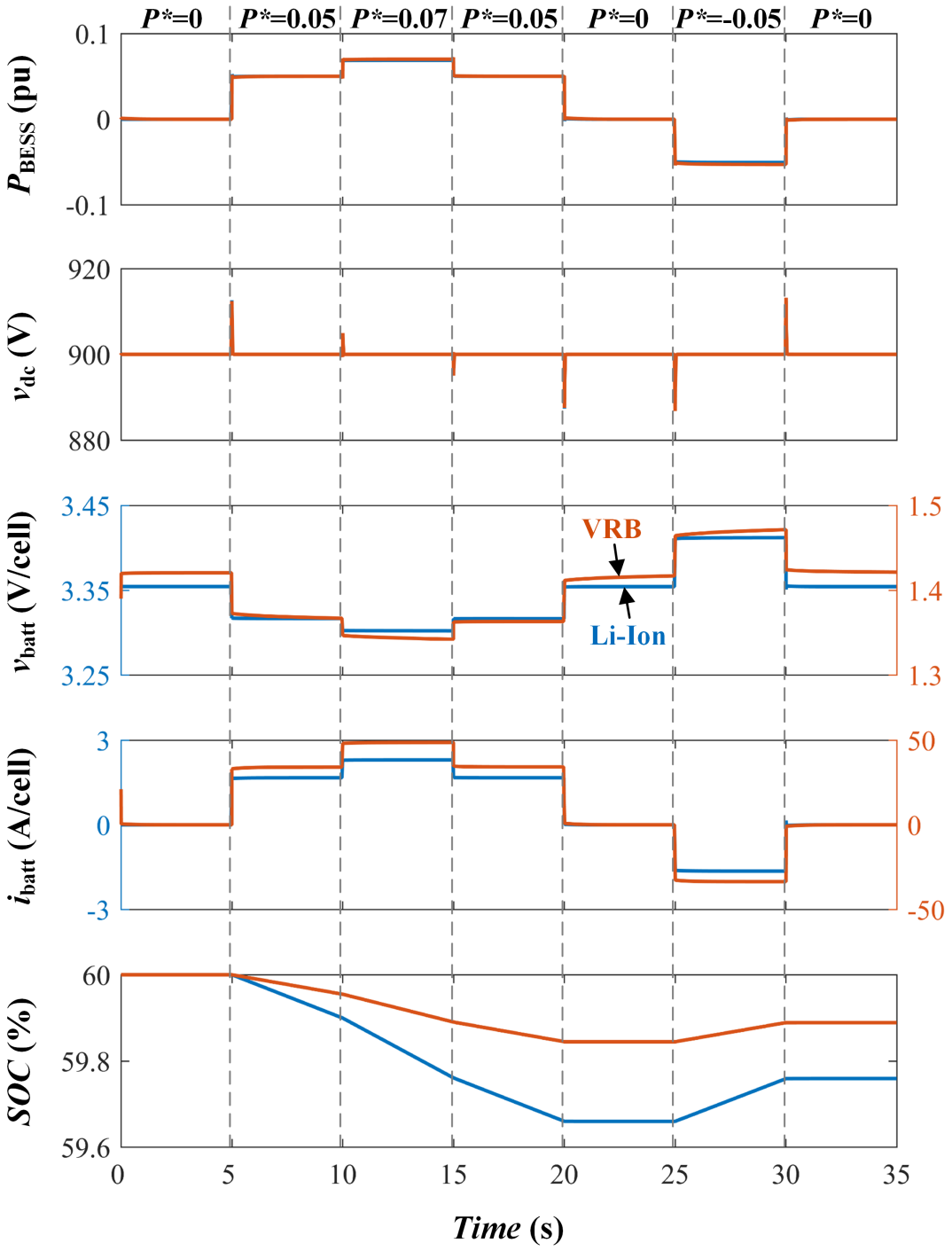

Figure 3.19: Active power control simulation for BESS emulator.

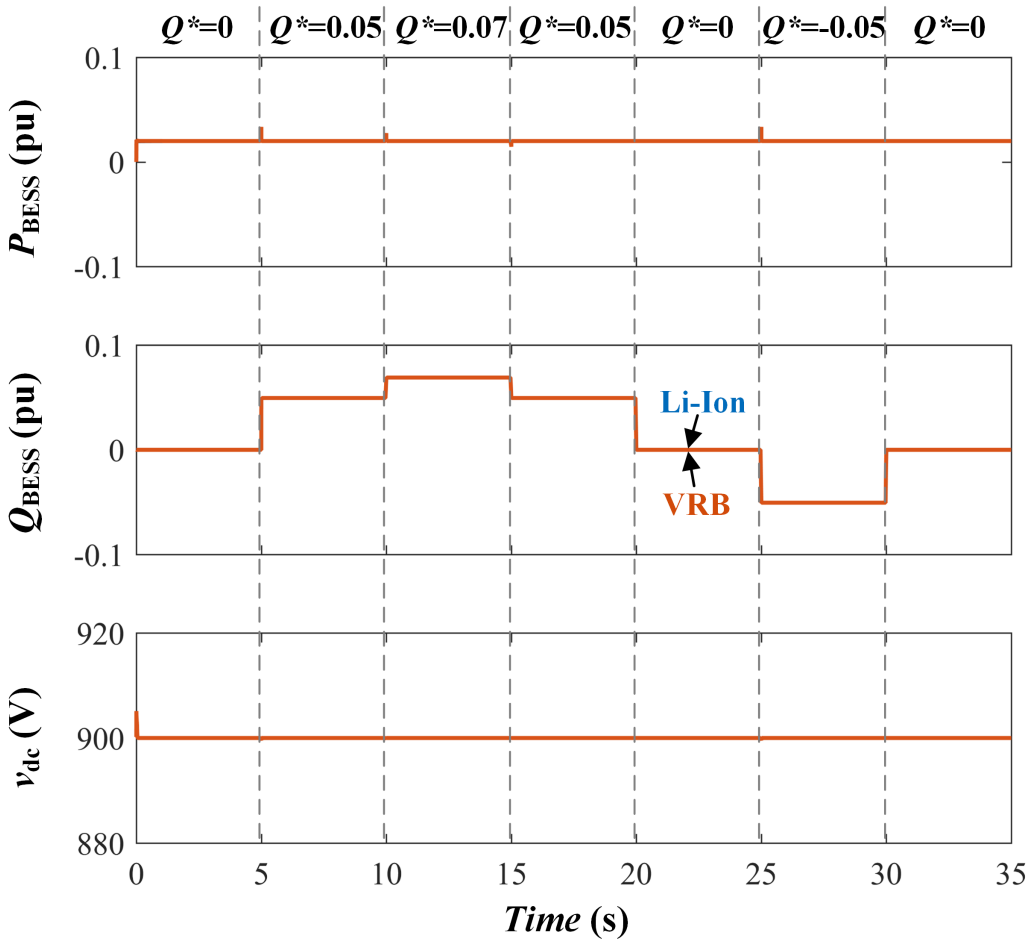

Figure 3.20: Reactive power control simulation for BESS emulator.

The reactive power control of the inverter was simulated with the same step changes for the reactive power command between 0 → 0.05 → 0.07 → 0.05 → 0 → -0.05 → 0 pu while the battery was discharging at 0.02 pu from an initial SOC of 60%. The resulting waveforms are shown in Fig. 3.20 and and demonstrate the appropriate step changes in reactive power injection but no change in active power. Thus, the independence of active and reactive power control was verified.

Because the application-specific control functions depend on system conditions for operation, they were only tested for basic functionality in simulation and then refined during testing on the HTB.

3.7 Chapter Summary

The emulated BESS contains an internal battery model, a two-stage power conditioning system, and an inductor filter at its point of connection with the power system. The internal battery model consists of previously-published models for Li-Ion, Pb-Acid, and VRB battery technologies, and the power conditioning system consists of a half-bridge and a boost rectifier implemented using average models. Because the boost rectifier contains the same physical topology as a VSI, the VSI on the HTB can be controlled as if it were the boost rectifier.

All current-source VSIs on the HTB have the same inner current control loop. The BESS's DC link voltage is controlled with a PI controller whose output is the direct current reference for the HTB VSI. Similarly, a reactive power control loop uses the quadrature current reference. Active power control is conducted by the DC-DC converter using average inductor current control. All of these control loops are confirmed to respond appropriately to active and reactive power commands in simulation. Outer power system support control loops for frequency and voltage are also implemented so that the BESS emulator can be used for primary frequency regulation, inertia emulation, and voltage support.

Chapter 4

Experimental Results and Discussion

In this chapter, the emulated BESS is implemented on a digital signal processor (DSP) and used to control a VSI on the HTB. The previously-simulated active and reactive power command tests are run on the physical HTB, and the application-specific support functions are also tested using instantaneous load changes. The system responses observed in these experiments are discussed in detail, and the BESS emulator is concluded to function as desired for all test cases.

4.1 Experimental Setup

To verify the BESS emulator's behavior on the HTB, it was tested in a single area cabinet with the configuration shown in Fig. 4.1. The cabinet included four inverters separated into two buses, one with a synchronous generator emulator and a ZIP load emulator and the other with the BESS emulator and another ZIP load emulator. These buses were separated by a 2.4 mH transmission line, and each inverter had a 0.5 mH inductor filter at its AC terminal. A photo of this setup is shown in Fig. 4.2.

The standard active and reactive power commands for the synchronous generator emulator and the ZIP load emulators are shown in Table 4.1. These are the typical start-up values for these emulators in the four-area WECC system, and they remain constant throughout all testing unless specified otherwise. For the WECC system to operate at 80% renewable generation, a large

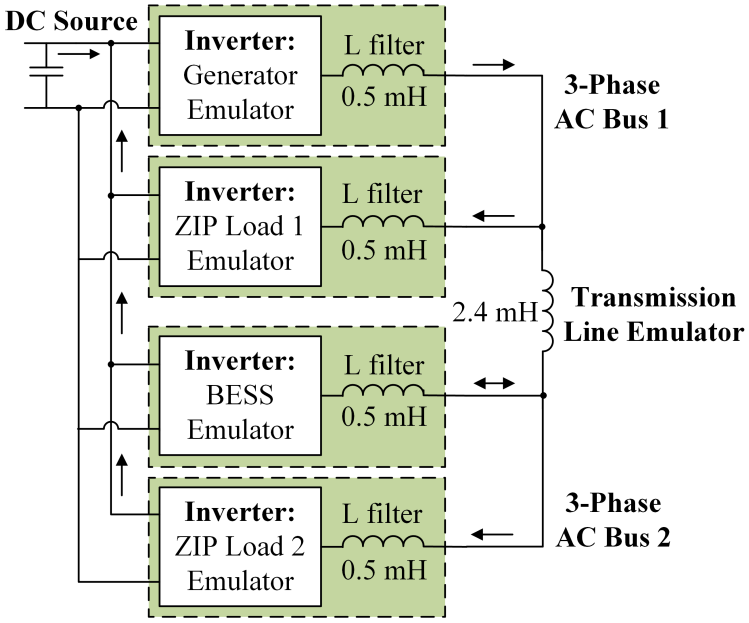

Figure 4.1: Single-area experimental setup for BESS emulator testing.

amount of reactive power compensation is required for voltage support in the area where the BESS emulator will be implemented. Both aggregated loads in this area are assumed to be capacitive as a result, so their default testing values in Table 4.1 are negative. Also, the generator's output power fluctuates as necessary to meet the needs of the system. Like in simulation, the BESS emulator was set to have a capacity of 700 MVA, or 0.07 pu on the HTB WECC system design.

For generators and storage on the HTB, a positive power value indicates power injection and a negative power value indicates absorption. For loads, a positive power value refers to absorption and a negative value indicates injection.

Table 4.1: Operating Point of Emulators in Experimental Setup

Power	Generator	Load 1	Load 2
$P_{mechanical}$ (pu)	0.1	–	–
P (pu)	–	0.1	0.07
Q (pu)	–	-0.1	-0.1

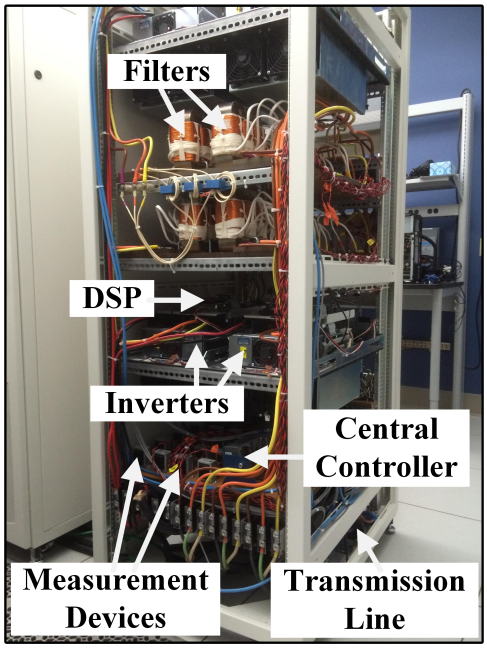

Figure 4.2: Photo of single-area experimental setup for BESS emulator testing.

4.2 Command-Based Experiments

The BESS was first tested using a series of command-based experiments to verify correct operation of its internal control. After the other emulators were brought to the operating points specified in Table 4.1, a sequence of command step changes were delivered to the BESS emulator.

The active power control and the DC link voltage control in the BESS emulator were first tested using active power command step changes from 0 $\rightarrow$ 0.05 $\rightarrow$ 0.07 $\rightarrow$ 0.05 $\rightarrow$ 0 $\rightarrow$ -0.05 $\rightarrow$ 0 pu, with five seconds between each step. The reactive power command was set to zero. The resulting internal BESS waveforms for the Li-Ion and VRB systems are shown in Fig. 4.3. Both systems show a similar step-change response in active power output as well as DC link regulation to within 1% of 900 V. The nominal voltage levels of the Li-Ion and VRB cells are 3.366 V and 1.39 V, respectively. Both average cell voltage waveforms show appropriate decreases when power output increases and the same in reverse due to internal series resistance. Also, the SOC level of each system decreases during discharging and increases during charging at a rate that varies according to power input/output.

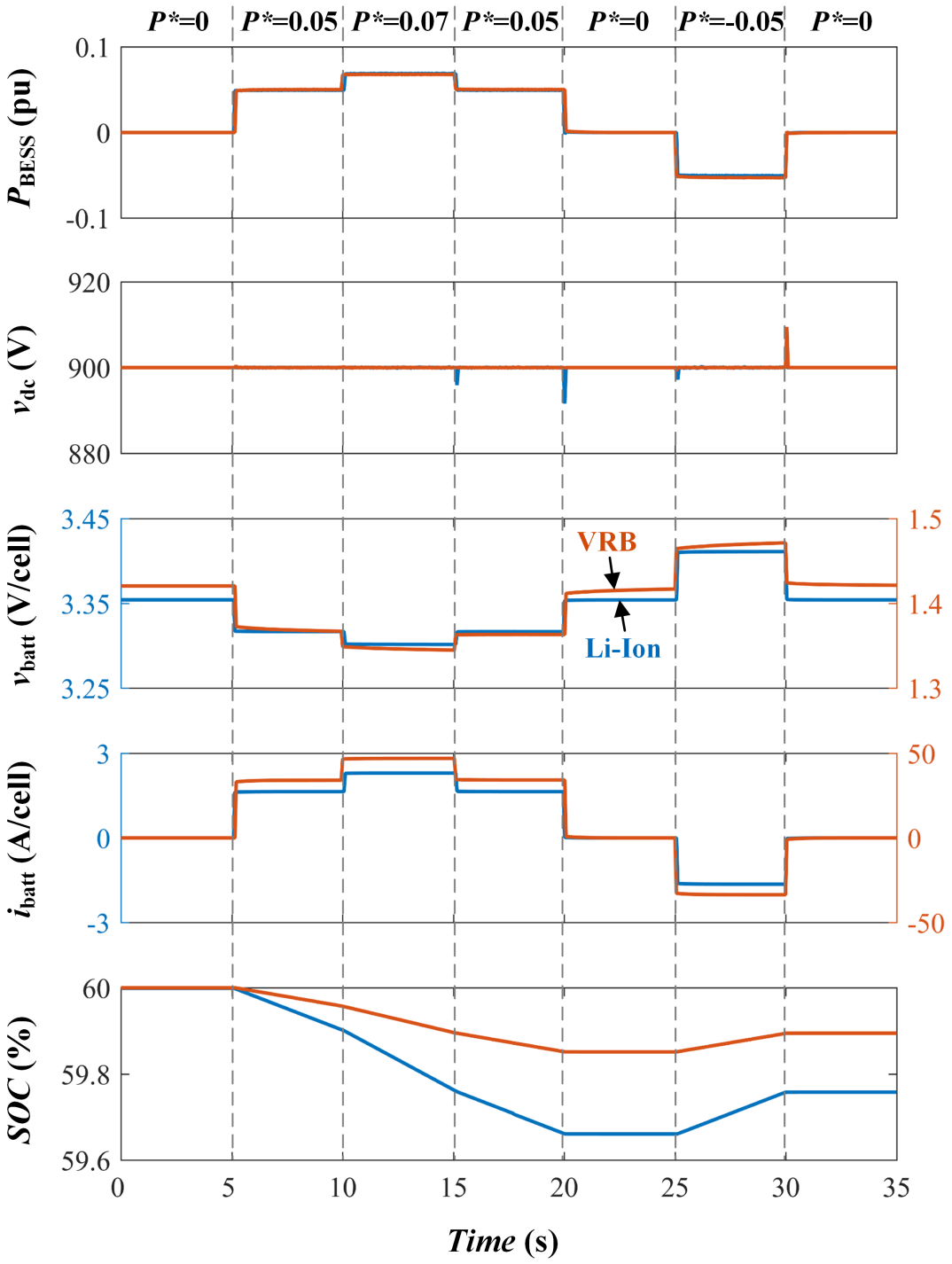

Figure 4.3: Experimental active power control test for BESS emulator.

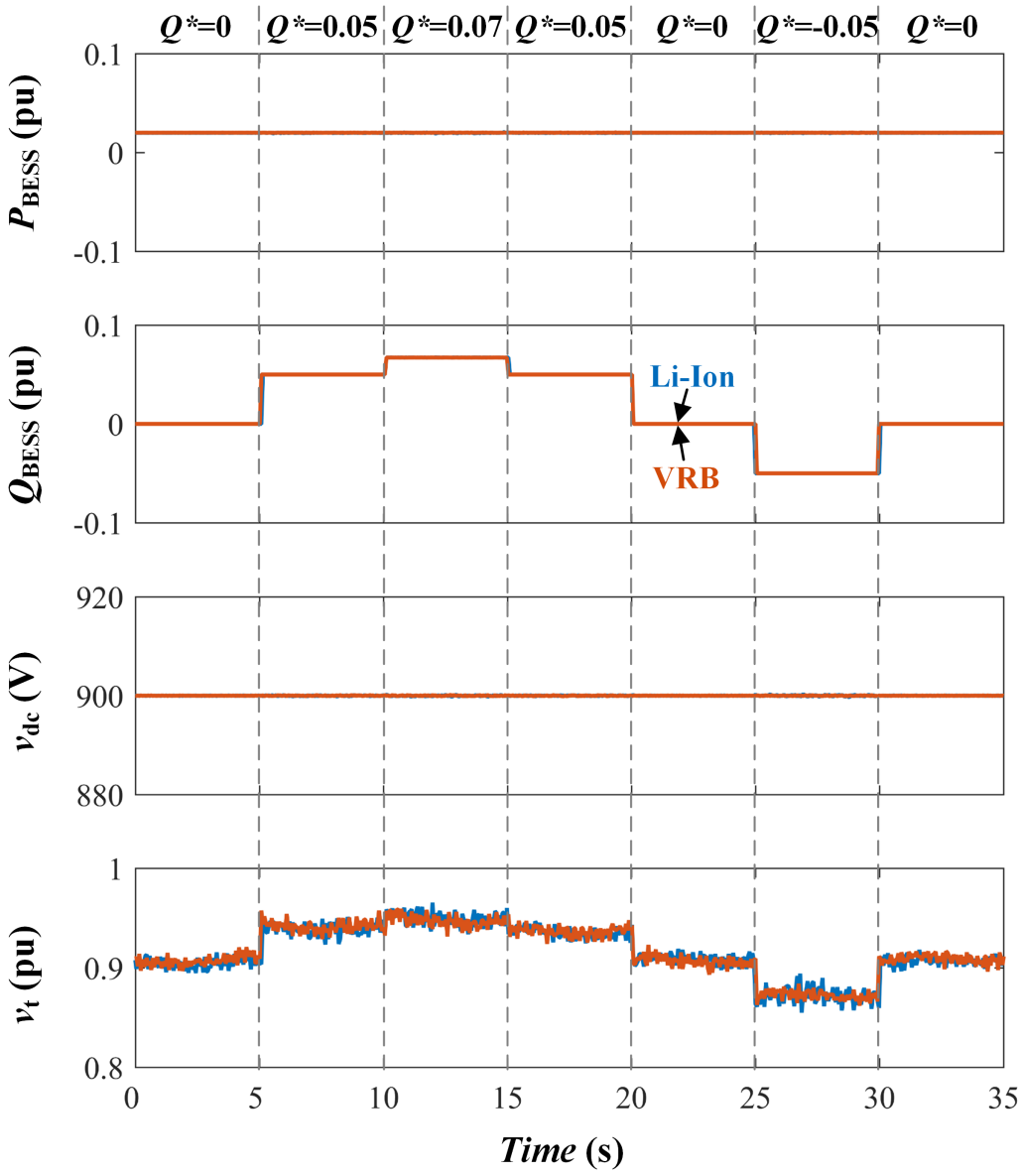

Figure 4.4: Experimental reactive power control test for BESS emulator.

The reactive power control was tested using reactive power step changes in the same sequence, $0 \rightarrow$ j0.05 $\rightarrow$ j0.07 $\rightarrow$ j0.05 $\rightarrow 0 \rightarrow$ -j0.05 $\rightarrow 0$ pu, with the active power command set at 0.02 pu. For the BESS emulator, a positive reactive power command results in reactive power injection and a negative command results in absorption. The resulting waveforms are shown in Fig. 4.4 for Li-Ion and VRB, respectively. Both show correct tracking of the reactive power command, unhindered

active power output, and a constant DC link voltage. This demonstrates independence between the emulated BESS's active and reactive power control loops. The BESS's terminal voltage rises when the BESS injects reactive power and falls when the BESS absorbs reactive power as expected. Thus, it was concluded that the emulated BESS's reactive power control functions appropriately.

4.3 Power System Support Experiments

Since the BESS emulator demonstrated appropriate responses to active and reactive power commands, its outer control loops for power system support services were tested next. With these control loops enabled, the active and reactive power commands for the emulated BESS are generated automatically based on the power system's needs. For all of these tests, Load 1 in Fig. 4.1 was switched on and off to emulate step changes in generation or load due to sudden generation or line losses. For comparison purposes, the system's response to this load change without any of the BESS emulator's support functions is shown in Fig. 4.5.

First, the emulated BESS's primary frequency regulation capability was tested using Load 1 step changes every 20 seconds, as shown in Fig. 4.6. Because this consists of only proportional control, the BESS emulator's active power output tracks the frequency's deviation from 60 Hz when it leaves its deadband of ± 10 mHz. In this case, the frequency settles closer to 60 Hz when the load is off but further from it when the load is on, so the amount of active power provided varies accordingly. In response to the load changes, the frequency's immediate deviation from 60 Hz is significantly reduced with the primary frequency regulation when compared to the case without it in Fig. 4.5.

Then, the BESS emulator's inertia emulation function was enabled in addition to the primary frequency regulation. The system was cycled through the same load changes every 20 seconds,

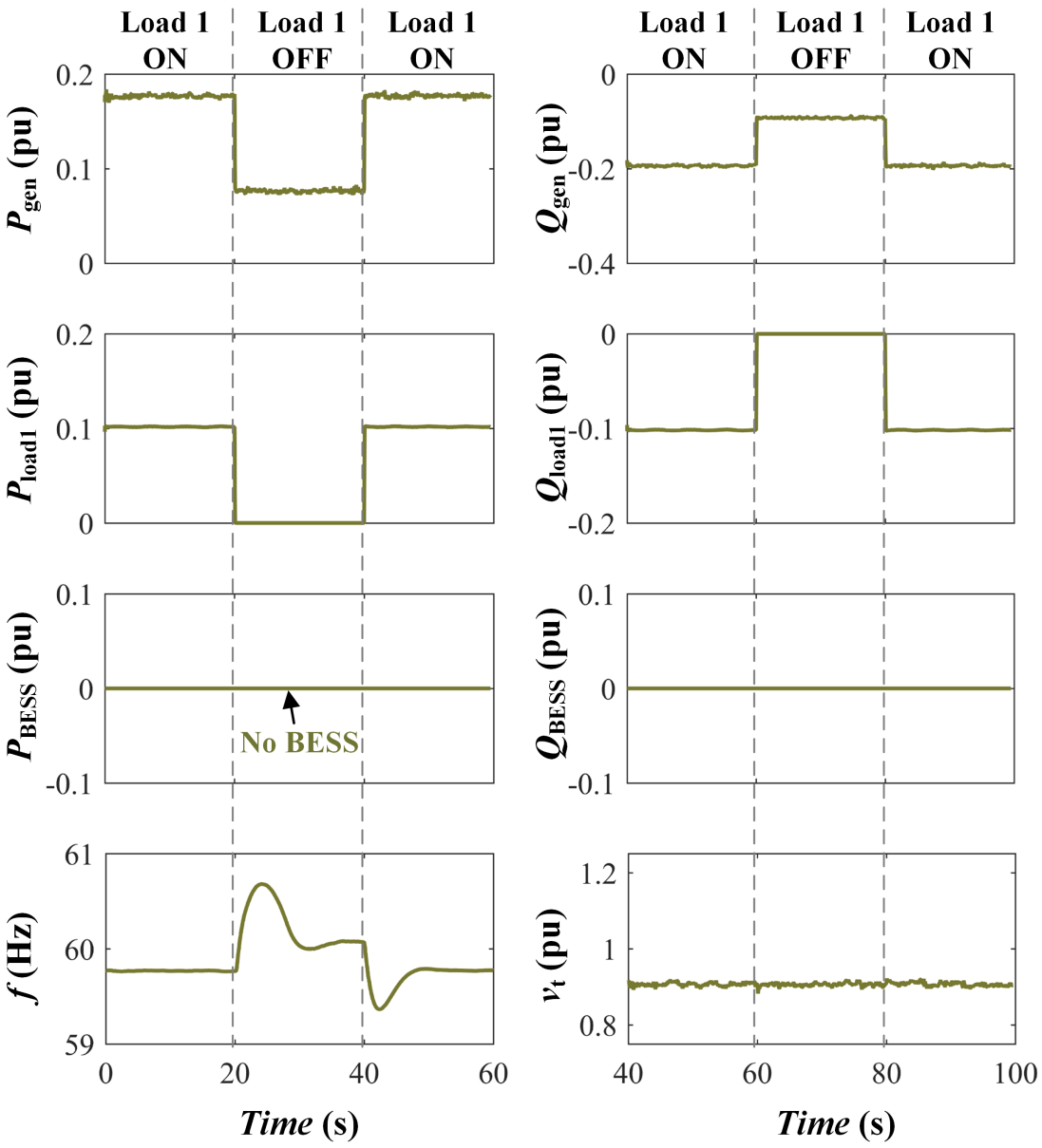

Figure 4.5: HTB system response to load change without BESS support.

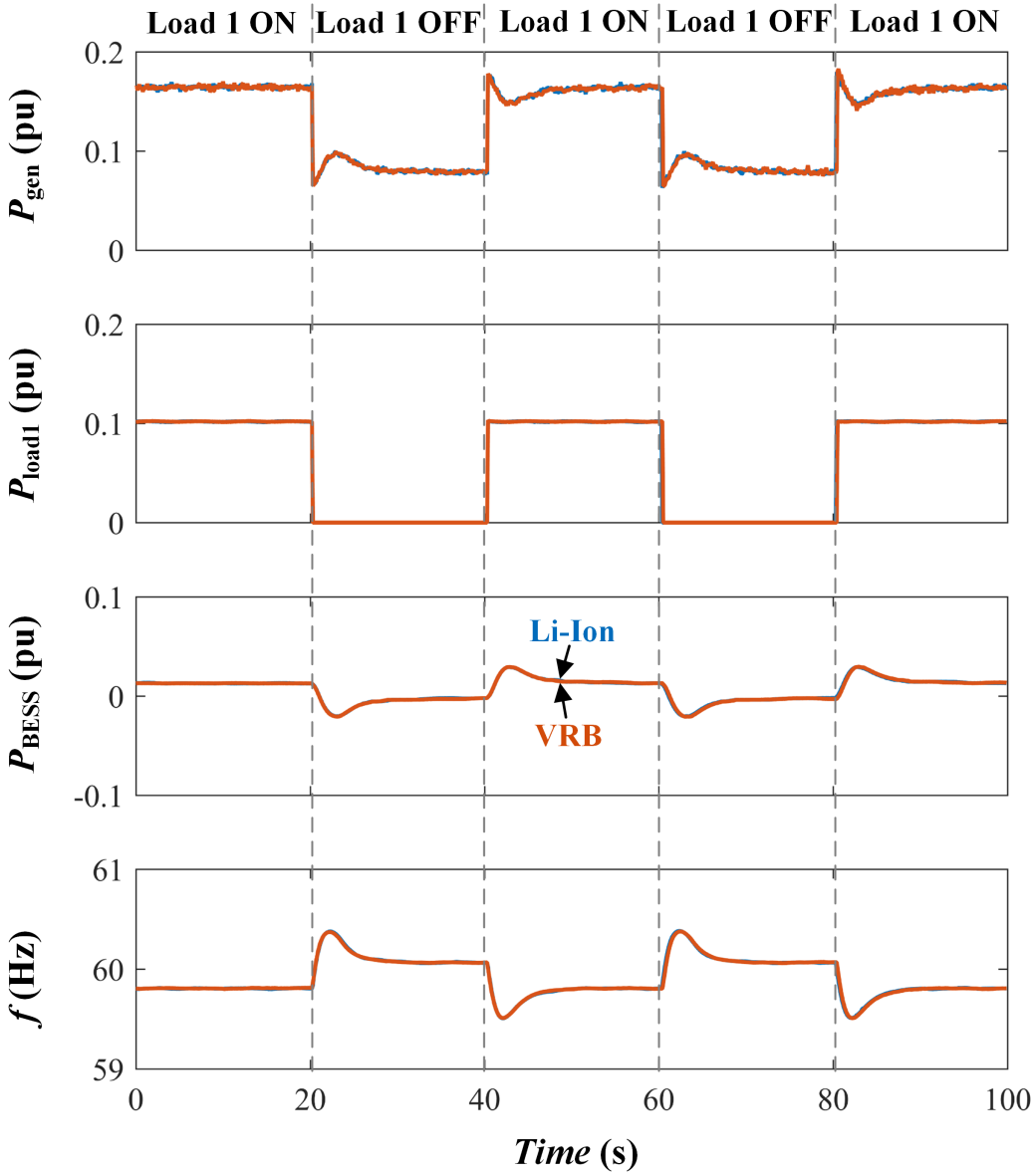

Figure 4.6: HTB system response to load change with primary frequency regulation conducted by BESS emulator.

and the resulting waveforms are shown in Fig. 4.7. With the inertia emulation enabled, the frequency controller reacted very quickly and forced the BESS emulator to reach full power almost immediately once the frequency change was detected. It then gradually declined in power input/output, resulting in a similarly-slow power curve for the generator that resembles a heavy inertial response. As a result, the frequency waveform shows very little deviation from 60 Hz in response to the load change when compared to the previous cases.

There is a spike in generator electrical power during the short time between the load's change and the BESS's response, but this was concluded to be mandated by Kirchoff's current law in the small two-bus system being tested. The generator emulator is the only voltage source in this small system, and all other emulators are controlled like current sources. Since there are no other electrical pathways for current to enter or exit the two buses, it is natural for the generator emulator to absorb the immediate current difference caused by the load change. The result is the short spike, and this spike causes the frequency to begin rising or falling until the BESS's inertia emulation function enabled.

The BESS's voltage support function was tested in a similar fashion with load changes every 20 seconds, and the resulting waveforms are shown in Fig. 4.8. For both systems, reactive power was injected appropriately throughout the whole duration of this test since the BESS's terminal voltage was always outside of its 5% deadband. Since the BESS's terminal voltage remained close to constant for the duration of the test, the BESS's reactive power output stayed relatively constant as well.

Finally, the ability of all three support functions to operate simultaneously was tested with the same load change scenario. As shown in Fig. 4.9, the frequency control behaves identically to the test when only primary frequency regulation and inertia emulation were enabled. The BESS emulator responds to the frequency change immediately, and there is very little deviation in the resulting frequency waveform. However, the voltage support capacity is now limited by the active power output since active power has priority over reactive power for the inverter's capacity. Because of this, the reactive power injection is limited by the curve of the active power output even when it is needed, resulting in the dips in BESS reactive power after the transitions at 20 and 40

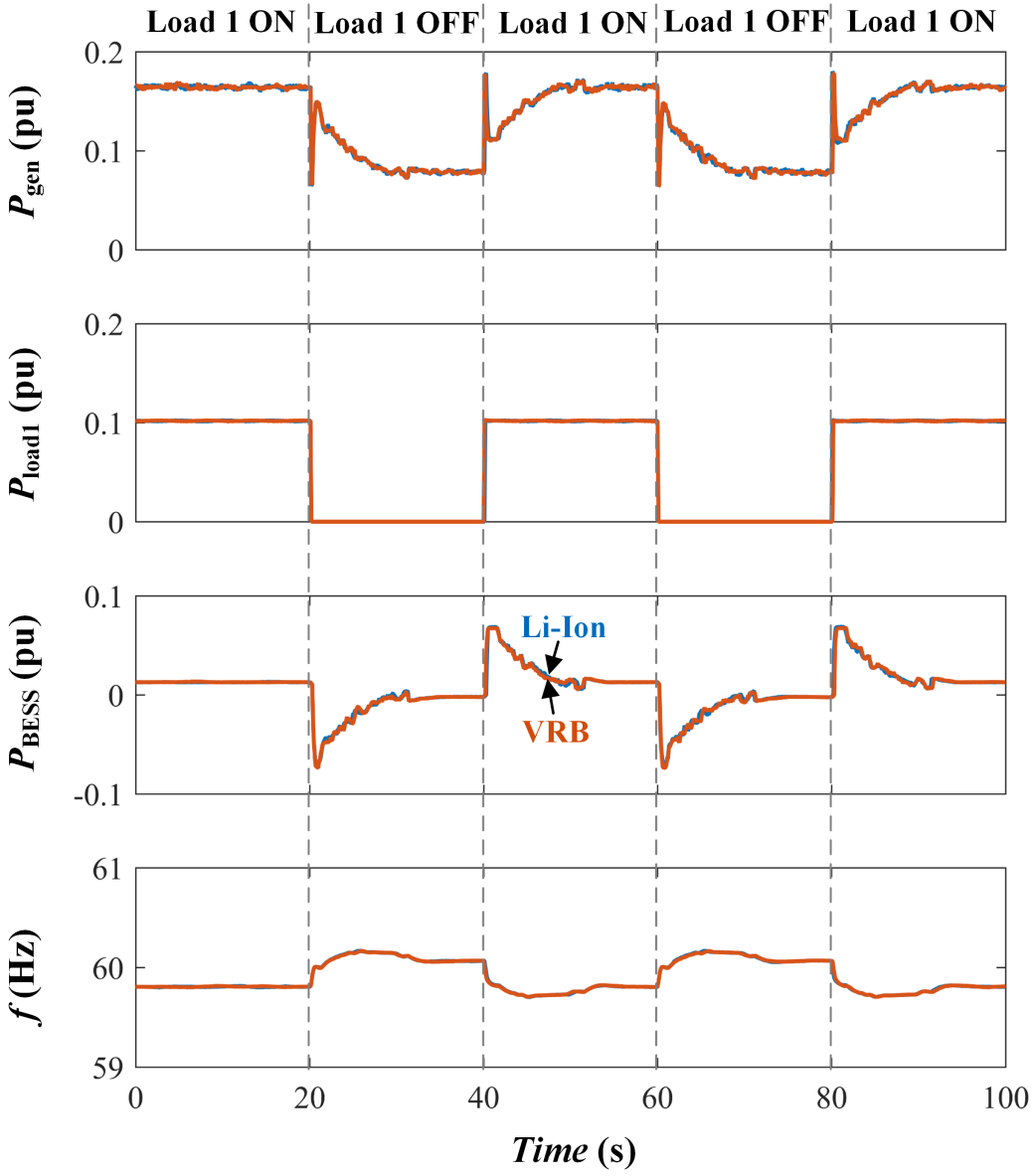

Figure 4.7: HTB system response to load change with primary frequency regulation and inertia emulation conducted by BESS emulator.

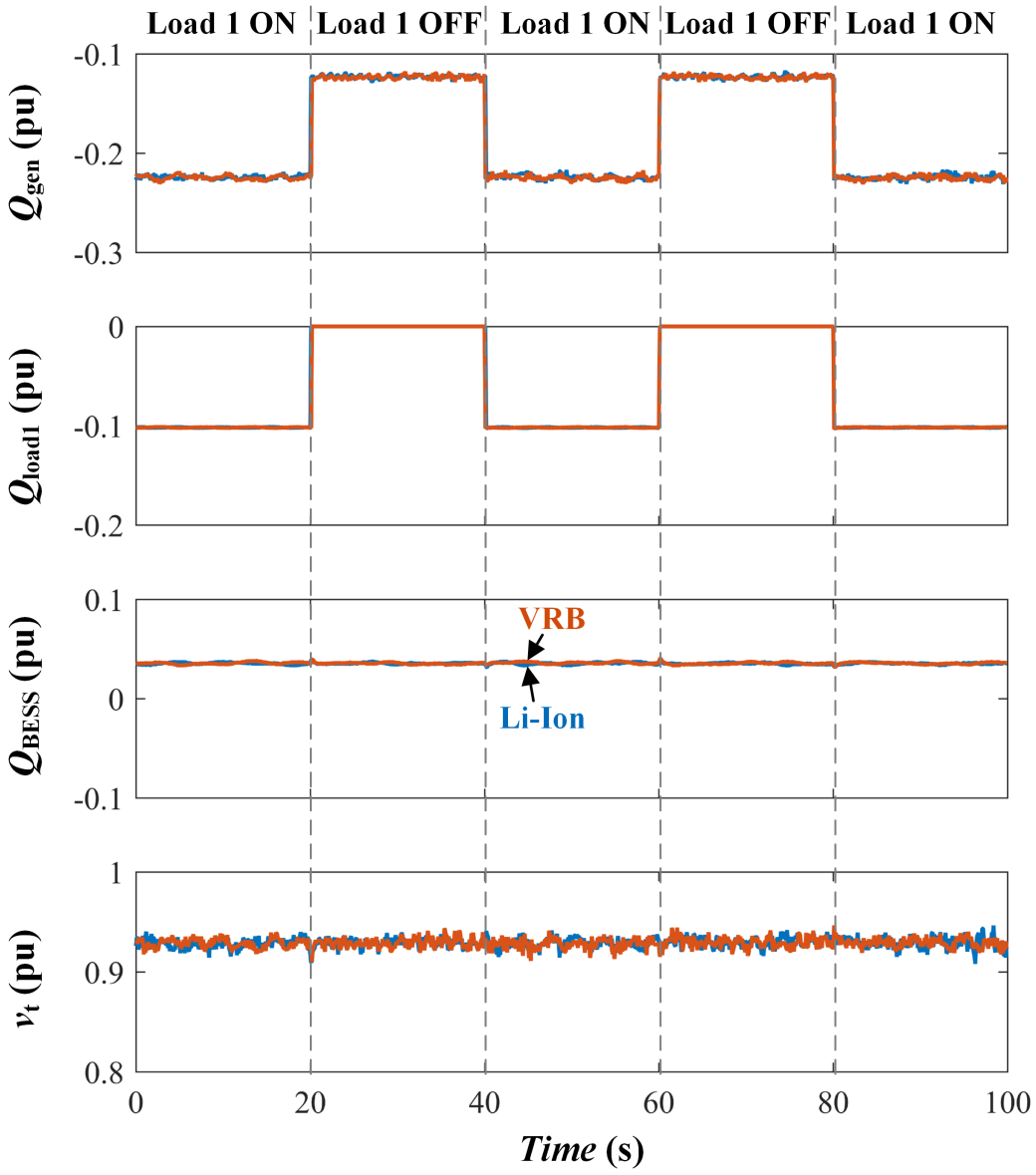

Figure 4.8: HTB system response to load change with voltage support conducted by BESS emulator.

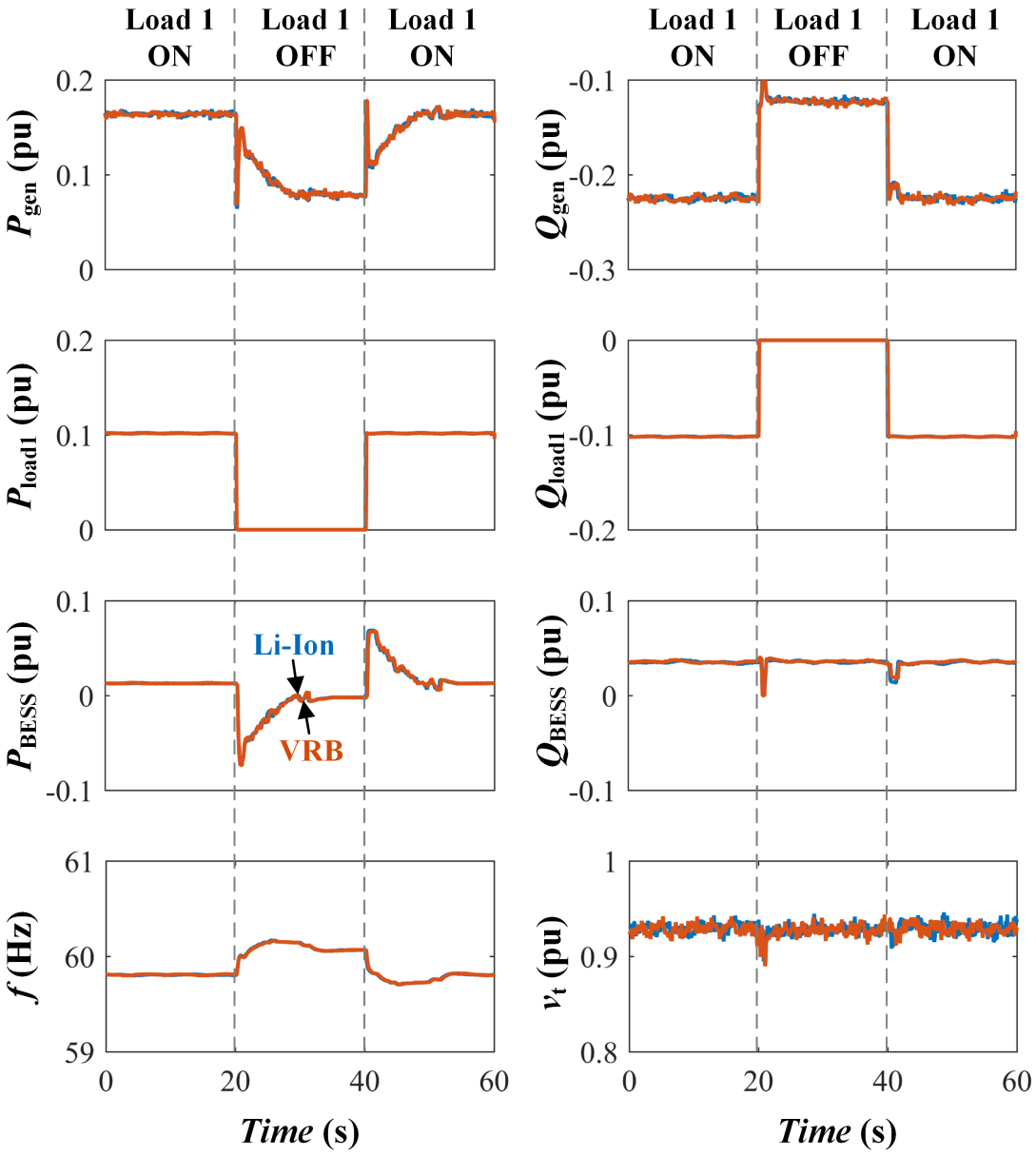

Figure 4.9: HTB system response to load change with all three support functions of BESS emulator.

seconds. When capacity becomes available again, the voltage support function uses it as reactive power. Thus, it was concluded that the three support functions are capable of seamless simultaneous operation.

4.4 Discussion

As observed in simulation and experimental results, the Li-Ion and VRB chemistries behaved very similarly and are nearly indistinguishable at the power system level. This can be attributed to the fact that their cell-level differences are effectively decoupled from the power system by the two-stage power electronics interface. The dynamics of both systems are slow enough for the power electronics to track them, so they are not observable at the system level. Thus, for power system support services, either technology can be used and the choice between them should depend on other technical specifications and economics rather than performance from the system's perspective.

The simulated and experimental results for the active power control and reactive power control tests are very similar. The primary difference for the active power control tests were disturbances in the DC link voltage, which appear to be significantly smaller in the experimental results. This can likely be attributed to the fact that the simulation records data points every 100 μs but the experimental data only has a precision of 100 ms. Since the DC link voltage spike observed in the simulation occurs for very little time, it is very likely that its highest points are missed by the experimental data collection. The same phenomenon was observed for spikes in active power during the simulated reactive power test. These were likely so short that they were between data points when the experimental data was recorded.

Fig. 4.10 displays the system's response to a load change for three different control conditions: no frequency control enabled, only primary frequency regulation enabled, and primary frequency regulation and inertia emulation enabled. The conditions for this load change are identical to those in Figs. 4.5, 4.6, and 4.7 at 40 seconds, using the Li-Ion BESS emulator. It is clear that adding only the primary frequency regulation helps suppress the frequency transient and reduces the duration of its swing, but the best response is achieved when inertia emulation is also enabled.

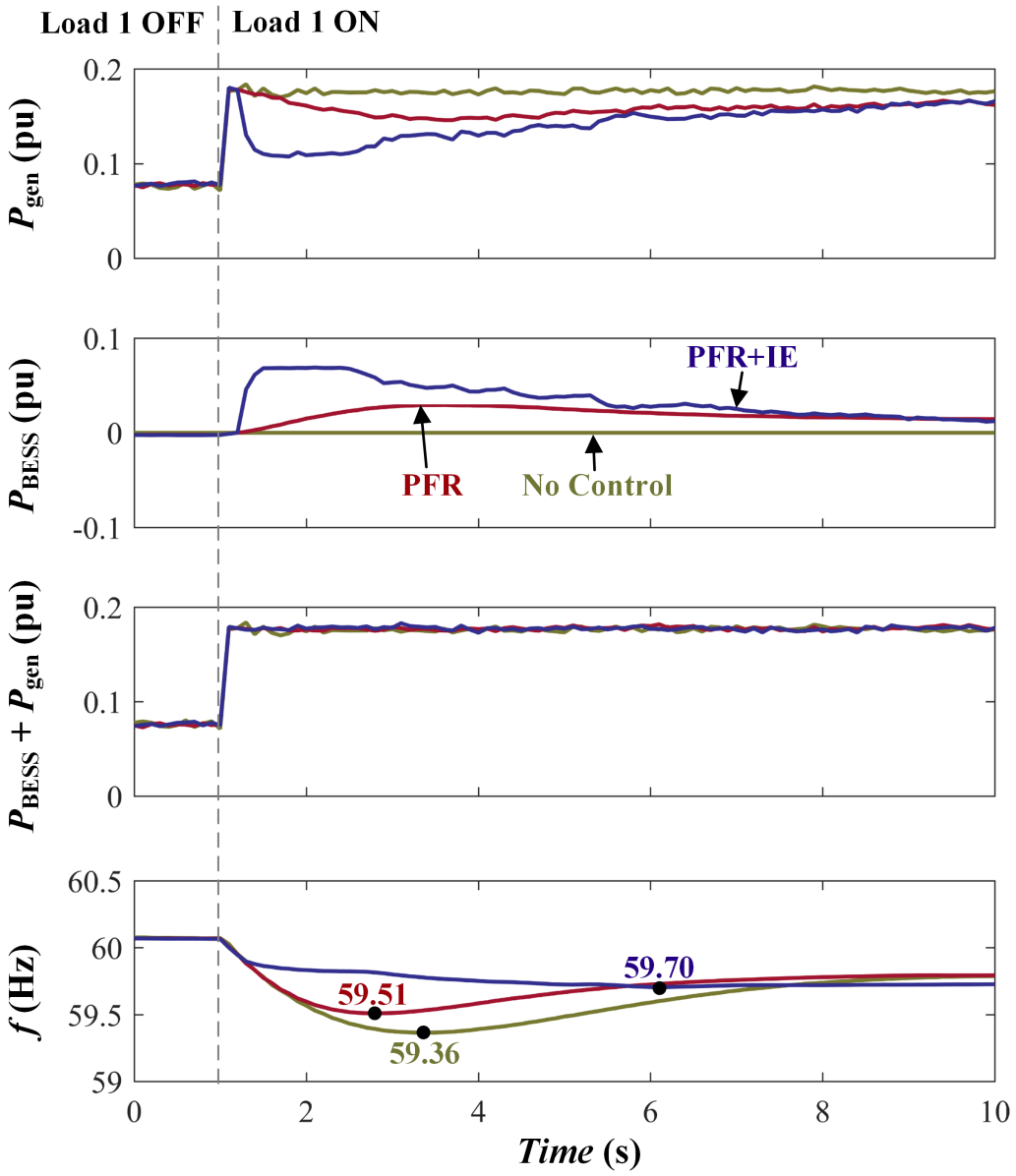

Figure 4.10: Comparison of HTB system responses to load change with and without frequency control functions of Li-Ion BESS emulator.

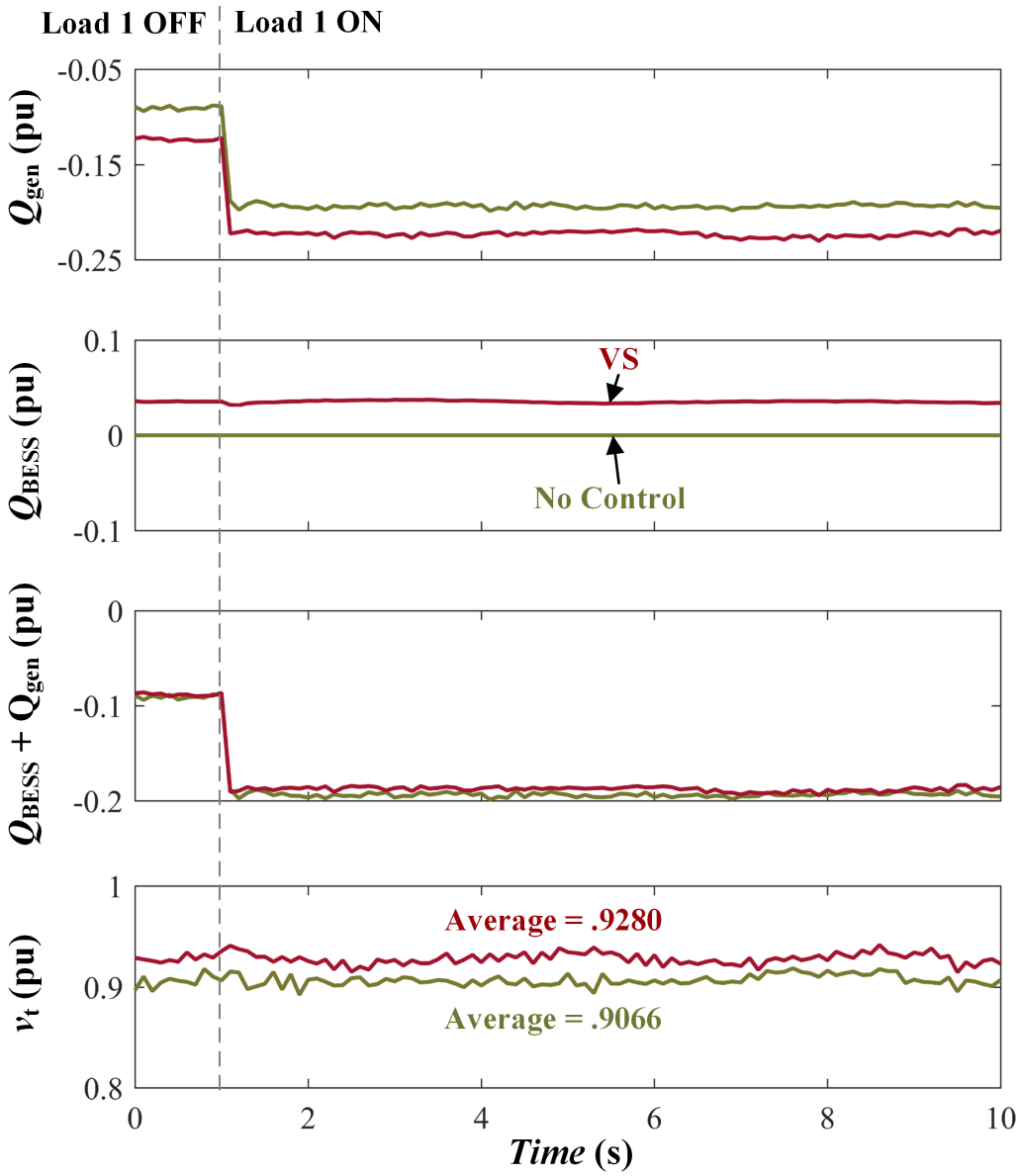

Figure 4.11: Comparison of HTB system responses to load change with and without voltage support of Li-Ion BESS emulator.

With inertia emulation, the BESS emulator reaches full power very soon after the load change and then slowly ramps down. This allows the frequency to ramp to its new stable value instead of swinging, which is significantly less taxing on the system as a whole. This difference in frequency swing can ultimately be attributed to the difference between mechanical and electrical power for the generator, which is the same for all cases immediately following the disturbance but is quickly compensated by the BESS when inertia emulation is enabled. The sum of the active power output from the generator and the BESS shows that the total active power injection is the same for all three cases.

Similarly, Fig. 4.11 displays the system's response to the same load change with no control and then with voltage support enabled. It is clear that the BESS emulator's bus voltage is maintained at a higher level with the voltage support enabled in comparison to the case without it. The sum of the reactive power injected by the generator and the BESS is similar for both cases, which shows that the generator absorbs most of the BESS's reactive power output during voltage support. However, since that occurs on a different bus, the BESS emulator's terminal voltage stays higher during the period following the disturbance.

Thus, it can be concluded that the BESS emulator is capable of providing primary frequency regulation, inertia emulation, and voltage support for HTB test scenarios. As shown in Fig. 4.9, these support functions can be run in parallel without compromising the effectiveness of any function as long as the system's support needs are within the BESS emulator's capacity. If the demand for BESS support exceeds its capacity, the voltage support function yields capacity to the frequency control functions, which can reduce the effectiveness of the voltage support. However, as the frequency support needs decrease, capacity is re-allocated to the voltage support in real time.

4.5 Chapter Summary

Models and control for the emulated BESS were implemented on a DSP and used to control one VSI on the HTB for experimental testing. The test setup included one generator emulator, two load emulators, and the BESS emulator, separated into two buses. The same active power control and reactive power control tests conducted in simulation were repeated experimentally on the

HTB, and the simulated and experimental responses compared closely for both the Li-Ion and the VRB internal battery technologies. Because the power conditioning system decouples the battery's behavior from the power system, the Li-Ion and VRB models were nearly indistinguishable from the system's perspective.

The application-specific control functions were tested by cycling one of the load emulators through on/off step changes. With primary frequency regulation enabled, the frequency swing as a result of the load change was significantly reduced. With inertia emulation enabled in addition to primary frequency regulation, the frequency swing was nearly eliminated. The voltage support function demonstrated appropriate levels of support for the BESS terminal voltage when it dropped below a certain threshold. These three support functions were concluded to be capable of simultaneous operation.

Chapter 5

Conclusions and Recommendations

Energy storage can be a valuable tool for power systems, especially for services such as balancing power generation and load. It is particularly beneficial for cases with intermittent or fluctuating generation, which is common for renewable energy sources such as wind and PV. The HTB is a VSI-based grid emulator designed for studying power system scenarios with high renewable penetration, so an energy storage emulator is a useful addition to the existing HTB emulator repertoire. Since the HTB already has flywheel energy storage, battery energy storage is the logical next choice for storage emulator development.

The emulated BESS was designed such that it contained an internal battery model and a two-stage power conditioning system connected to the larger power system. Due to their present and projected prevalence, Li-Ion, Pb-Acid, and VRB battery technologies were selected for implementation in the emulator. A dynamic battery model based on the Shepherd model was selected for the Li-Ion and Pb-Acid technologies, as there are only minor differences between the behaviors of conventional battery technologies. A Thevenin model with one R-C pair was selected for the VRB.

The power electronics interface was designed using a bi-directional half-bridge as its DC-DC converter and a bi-directional boost rectifier with an inductor filter between its output and the power system coupling point. These were implemented using average models, and multiple control loops were designed to govern their actions like the system supervisory control of a BESS. The DC-DC

converter's duty cycle was used to conduct active power control, and the boost rectifier's direct and quadrature current references were used to conduct DC link voltage control and reactive power control, respectively.

A plethora of applications exists for energy storage in power systems, so control loops automating support functions for frequency and voltage were designed for the BESS emulator. The frequency control loop consists of a proportional controller for primary frequency regulation and a derivative controller for inertia emulation, both of which are summed to generate an active power command for the emulated BESS. The voltage control loop creates a reactive power command for the emulated BESS with a proportional controller for the BESS's terminal voltage.

The sole purpose of this BESS design is to emulate a typical BESS's behavior at its terminals so that its interactions with the power system are authentic. Because the boost rectifier has the same physical topology as the VSI, the physical VSI on the HTB can be controlled as if it were the boost rectifier in the emulated BESS. The models and control for the emulated BESS were implemented on a DSP, and the DSP used the current references generated for the emulated boost rectifier to control the physical VSI on the HTB.

The BESS's active and reactive power control functions were tested with command step changes in simulation and experimental testing. Both control loops produced appropriate responses to the commands, and independence between active and reactive power control was demonstrated. The simulated and experimental waveforms were very similar for both internal battery model types, and the DC link voltage was closely regulated to its nominal value. Also, the battery voltage, current, and SOC increased and decreased with patterns that reflected correct internal battery model behavior. Because the internal battery model behavior is decoupled from the power system by the power conditioning system, the Li-Ion and the VRB battery systems are virtually indistinguishable at the system level.

The automated support functions for the BESS emulator were tested by cycling a nearby load through on-off step changes. With only primary frequency regulation enabled, a significant reduction was achieved in the frequency swing due to the load change. When inertia emulation was enabled in addition to primary frequency regulation, the frequency swing was effectively

eliminated. Similarly, the voltage support function demonstrated a positive effect on the BESS emulator's terminal voltage. Finally, all three support functions were enabled and confirmed to operate correctly and simultaneously, during which active power had priority over reactive power when the BESS reached full apparent power capacity.

Thus, the BESS emulator is now ready for use in HTB scenario tests. In the future, the BESS emulator can be used to study how battery energy storage can be used to support a WECC system with up to 80% renewable generation. Topics of investigation may include how much storage capacity is necessary for a desired level of system support as well as the best location(s) for the storage within the power system. The BESS capacity specified for this design (700 MVA) was very small compared to the whole WECC system, which has a power base of 10 GVA on the HTB. For this reason, a single BESS emulator will not be capable of providing enough frequency or voltage support when major events happen in the system. Thus, multiple BESS emulators should be used in multiple places within the HTB's WECC system or the BESS emulator should be scaled to a larger capacity if a substantial effect on the power system is desired. The BESS emulator can be scaled to have as many blocks as necessary for the HTB system's needs.

Combined emulators featuring the emulated BESS and other power system components could also be developed so that the HTB can represent more detailed power systems. Combining emulators requires that the combined models and control still fit within the sampling time of the DSP, which will be a challenge for emulators using the BESS. Both the Li-Ion/Pb-Acid and the VRB emulated systems use almost all of the allowable computation time per DSP cycle, so their models must be implemented in less computationally-heavy ways before being combined with generator or load models. This can be accomplished by replacing the exponential in the Li-Ion/Pb-Acid model and the logarithm in the VRB model with lookup tables, as these are particularly slow functions.

Performance specifications should be defined for each of the BESS emulator's control functions and power system support applications. For the internal active and reactive power control loops, these may include control bandwidth, gain and phase margin, overshoot, and settling time. For the frequency control, efficacy may be measured by BESS emulator response time

or by frequency swing characteristics like peak value or settling time. Also, the addition of a BESS in a power system may increase generator stress if the generator overcompensates for the BESS emulator's actions. All of these factors should be considered when evaluating the BESS emulator's performance for a specific application, and its control parameters should be redesigned if specifications are not met.

The BESS emulator that has been developed does not consider capacity fade or cell-balancing needs. Also, the Li-Ion/Pb-Acid model does not consider temperature, and the VRB model does not consider losses due to its pumping system. All of these factors were determined to be unnecessary for the intended use of the BESS emulator on the HTB, but future applications may require them. If that is the case, the internal battery models should be modified to include them.

Bibliography

[1] "Renewable infrastructure investment handbook: A guide for institutional investors," World Economic Forum, Tech. Rep., Dec. 2016. 1

[2] M. Higgins, E. Burgess, and B. Ehrlich, "Energy storage likely to increase in utility resource planning," *Natural Gas & Electricity*, vol. 32, no. 10, pp. 1–9, Apr. 2016. 1

[3] A. McCrone, U. Moslener, F. d'Estais, E. Usher, and C. Grüning, "Global trends in renewable energy investment 2016," Frankfurt School UNEP Collaborating Centre for Climate and Sustainable Energy Finance, Tech. Rep., March 2016. 1, 19

[4] A. Gallo, J. Simões-Moreira, H. Costa, M. Santos, and E. M. dos Santos, "Energy storage in the energy transition context: A technology review," *Renewable and Sustainable Energy Reviews*, vol. 65, pp. 800–822, Nov. 2016. 1, 3, 4, 5, 8, 9, 10, 11, 12, 13, 14, 15, 16, 17, 18, 19, 20, 21, 22, 34

[5] "Grid energy storage," US Department of Energy, Tech. Rep., Dec. 2013. 1, 6, 10, 11, 14, 19, 20, 22, 23

[6] M. Aneke and M. Wang, "Energy storage technologies and real life applications – A state of the art review," *Applied Energy*, vol. 179, pp. 350–377, Oct. 2016. 1, 9, 10, 11, 12, 13, 14, 15, 16, 17, 18, 19, 20, 21, 22, 23

[7] M. T. Lawder, B. Suthar, P. W. Northrop, S. De, C. M. Hoff, O. Leitermann, M. L. Crow, S. Santhanagopalan, and V. R. Subramanian, "Battery energy storage system (BESS) and battery management system (BMS) for grid-scale applications," *Proceedings of the IEEE*, vol. 102, no. 6, pp. 1014–1030, May 2014. 1, 12, 13, 16, 31, 32, 33, 34, 51

[8] R. Kempener and E. Borden, "Battery storage for renewables: Market status and technology outlook," International Renewable Energy Agency, Tech. Rep., Jan. 2015. 2, 3, 4, 5, 6, 7, 12, 14, 15, 16, 18, 19, 20, 23, 31, 33, 34

[9] D. M. Rastler, "Electricity energy storage technology options: A white paper primer on applications, costs and benefits," Electric Power Research Institute, Tech. Rep. 1020676, Dec. 2010. 2, 9, 10, 11, 16, 19, 20, 21, 23

[10] A. A. Akhil, G. Huff, A. B. Currier, B. C. Kaun, D. M. Rastler, S. B. Chen, A. L. Cotter, D. T. Bradshaw, and W. D. Gauntlett, "DOE/EPRI 2013 electricity storage handbook in collaboration with NRECA," Sandia National Laboratories, Tech. Rep. SAND2013-5131, July 2013. 2, 3, 4, 5, 6, 7, 8, 9, 10, 11, 12, 13, 14, 15, 16, 17, 19, 20, 21

[11] "Balancing and frequency control," North American Electric Reliability Corporation (NERC) Resources Subcommittee, Tech. Rep., Jan. 2011. 5, 6, 57, 58

[12] F. Díaz-González, M. Hau, A. Sumper, and O. Gomis-Bellmunt, "Participation of wind power plants in system frequency control: Review of grid code requirements and control methods," *Renewable and Sustainable Energy Reviews*, vol. 34, pp. 551–564, June 2014. 5, 59

[13] J. Schmutz, "Primary frequency control provided by battery," June 2013, Power Systems and High Voltage Laboratories, Federal Institute of Technology Zurich. 5, 57, 58

[14] P. Tielens and D. Van Hertem, "Grid inertia and frequency control in power systems with high penetration of renewables," in *Proc. Young Researchers Symposium in Electrical Power Engineering*, 2012. 6, 7, 59

[15] S. M. Alhejaj and F. M. Gonzalez-Longatt, "Investigation on grid-scale BESS providing inertial response support," in *Proc. IEEE International Conference on Power System Technology*, 2016, pp. 1–6. 7, 31, 56, 57, 59, 60

[16] I. Serban and C. Marinescu, "Control strategy of three-phase battery energy storage systems for frequency support in microgrids and with uninterrupted supply of local loads," *IEEE Transactions on Power Electronics*, vol. 29, no. 9, pp. 5010–5020, Sept. 2014. 7, 56, 59, 60

[17] V. Khadkikar, R. K. Varma, and R. Seethapathy, "Grid voltage regulation utilizing storage batteries in PV solar-wind plant based distributed generation system," in *Proc. IEEE Electrical Power & Energy Conference*, 2009, pp. 1–6. 7, 61

[18] S. J. Lee, J. H. Kim, C. H. Kim, S. K. Kim, E. S. Kim, D. U. Kim, K. K. Mehmood, and S. U. Khan, "Coordinated control algorithm for distributed battery energy storage systems for mitigating voltage and frequency deviations," *IEEE Transactions on Smart Grid*, vol. 7, no. 3, pp. 1713–1722, May 2016. 8

[19] O. Ipinnimo, S. Chowdhury, S. Chowdhury, and J. Mitra, "A review of voltage dip mitigation techniques with distributed generation in electricity networks," *Electric Power Systems Research*, vol. 103, pp. 28–36, Oct. 2013. 8, 60

[20] J. Tant, F. Geth, D. Six, P. Tant, and J. Driesen, "Multiobjective battery storage to improve PV integration in residential distribution grids," *IEEE Transactions on Sustainable Energy*, vol. 4, no. 1, pp. 182–191, Jan. 2013. 8

[21] E. Demirok, P. C. Gonzalez, K. H. Frederiksen, D. Sera, P. Rodriguez, and R. Teodorescu, "Local reactive power control methods for overvoltage prevention of distributed solar inverters in low-voltage grids," *IEEE Journal of Photovoltaics*, vol. 1, no. 2, pp. 174–182, Oct. 2011. 8, 60, 61

[22] U.S. grid energy storage factsheet (2016). Center for Sustainable Systems, University of Michigan. Pub. No. CSS15-17. 9, 10, 11, 18, 19, 23

[23] V. F. Pires, E. Romero-Cadaval, D. Vinnikov, I. Roasto, and J. Martins, "Power converter interfaces for electrochemical energy storage systems – A review," *Energy Conversion and Management*, vol. 86, pp. 453–475, Oct. 2014. 9, 34, 35, 36, 37, 38, 39, 40, 41, 56, 57

[24] S. Sabihuddin, A. E. Kiprakis, and M. Mueller, "A numerical and graphical review of energy storage technologies," *Energies*, vol. 8, no. 1, pp. 172–216, 2015. 9, 13, 14, 15, 16, 17, 18, 19, 20, 21, 22

[25] H. Verma, J. Gambhir, and S. Goyal, "Energy storage: A review," *International Journal of Innovative Technology and Exploring Engineering*, vol. 3, no. 1, June 2013. 9, 10, 11, 12, 13, 17, 18, 19, 20, 22

[26] M. S. Whittingham, "History, evolution, and future status of energy storage," *Proceedings of the IEEE*, vol. 100, pp. 1518–1534, Apr. 2012. 11, 12, 13, 17, 19, 22

[27] R. Hidalgo-León and P. Jácome-Ruiz, "A survey on technologies to implement battery emulators based on DC/DC power converters." pp. 1–11, 2016. 11, 20, 29, 30, 36, 37, 38, 42, 43, 44

[28] A. R. Sparacino, G. F. Reed, R. J. Kerestes, B. M. Grainger, and Z. T. Smith, "Survey of battery energy storage systems and modeling techniques," in *Proc. IEEE Power and Energy Society General Meeting*, 2012, pp. 1–8. 12, 14, 16, 17, 19, 20, 21, 22, 42, 43, 44, 45

[29] M. Obi, S. Jensen, J. B. Ferris, and R. B. Bass, "Calculation of levelized costs of electricity for various electrical energy storage systems," *Renewable and Sustainable Energy Reviews*, vol. 67, pp. 908–920, Jan. 2017. 12, 15

[30] Y. Zhang, J. Zhao, P. Wang, M. Skyllas-Kazacos, B. Xiong, and R. Badrinarayanan, "A comprehensive equivalent circuit model of all-vanadium redox flow battery for power system analysis," *Journal of Power Sources*, vol. 290, pp. 14–24, 2015. 15, 43, 44, 47, 51, 52, 67, 85

[31] L. Barote, R. Weissbach, R. Teodorescu, C. Marinescu, and M. Cirstea, "Stand-alone wind system with vanadium redox battery energy storage," in *Proc. IEEE International Conference on Optimization of Electrical and Electronic Equipment*, 2008, pp. 407–412. 16, 21

[32] V. Knap, R. Sinha, M. Swierczynski, D.-I. Stroe, and S. Chaudhary, "Grid inertial response with lithium-ion battery energy storage systems," in *Proc. IEEE International Symposium on Industrial Electronics*, 2014, pp. 1817–1822. 20, 59, 60

[33] Y. A. Gandomi, D. Aaron, T. Zawodzinski, and M. Mench, "In situ potential distribution measurement and validated model for all-vanadium redox flow battery," *Journal of The Electrochemical Society*, vol. 163, no. 1, pp. A5188–A5201, 2016. 21, 42, 43

[34] W. B. Ray, A. S. Subburaj, J. A. Schrock, and S. B. Bayne, "Economic analysis of battery energy storage system," in *Proc. IEEE Industry Applications Society Annual Meeting*, 2015, pp. 1–7. 22

[35] A. Malhotra, B. Battke, M. Beuse, A. Stephan, and T. Schmidt, "Use cases for stationary battery technologies: A review of the literature and existing projects," *Renewable and Sustainable Energy Reviews*, vol. 56, pp. 705–721, Apr. 2016. 23, 31

[36] Department of Energy global energy storage database. U.S. Department of Energy. [Online]. Available: http://www.energystorageexchange.org/projects/data_visualization 23

[37] L. Yang, X. Zhang, Y. Ma, J. Wang, L. Hang, K. Lin, L. M. Tolbert, F. Wang, and K. Tomsovic, "Hardware implementation and control design of generator emulator in multi-converter system," in *Proc. IEEE Applied Power Electronics Conference and Exposition*, 2013, pp. 2316–2323. 24, 25, 26, 27

[38] J. Wang, L. Yang, Y. Ma, X. Shi, X. Zhang, L. Hang, K. Lin, L. M. Tolbert, F. Wang, and K. Tomsovic, "Regenerative power converters representation of grid control and actuation emulator," in *Proc. IEEE Energy Conversion Congress and Exposition*, 2012, pp. 2460–2465. 24, 25, 26, 27

[39] W. Cao, Y. Ma, J. Wang, L. Yang, J. Wang, F. Wang, and L. M. Tolbert, "Two-stage PV inverter system emulator in converter based power grid emulation system," in *Proc. IEEE Energy Conversion Congress and Exposition*, 2013, pp. 4518–4525. 24, 27, 73

[40] J. Wang, L. Yang, Y. Ma, J. Wang, L. M. Tolbert, F. Wang, and K. Tomsovic, "Static and dynamic power system load emulation in a converter-based reconfigurable power grid emulator," in *Proc. IEEE Energy Conversion Congress and Exposition*, 2014, pp. 4008–4015. 24, 27

[41] J. Wang, L. Yang, Y. Ma, J. Wang, L. M. Tolbert, F. F. Wang, and K. Tomsovic, "Static and dynamic power system load emulation in a converter-based reconfigurable power grid

emulator," *IEEE Transactions on Power Electronics*, vol. 31, no. 4, pp. 3239–3251, 2016. 24, 27

[42] L. Yang, Y. Ma, J. Wang, J. Wang, X. Zhang, L. M. Tolbert, F. Wang, and K. Tomsovic, "Development of converter based reconfigurable power grid emulator," in *Proc. IEEE Energy Conversion Congress and Exposition*, 2014, pp. 3990–3997. 24, 26

[43] L. Yang, J. Wang, Y. Ma, J. Wang, X. Zhang, L. Tolbert, F. Wang, and K. Tomsovic, "Three-phase power converter based real-time synchronous generator emulation," *IEEE Transactions on Power Electronics*, vol. 32, no. 2, pp. 1651–1665, Feb. 2017. 24

[44] X. Shi, Z. Wang, Y. Ma, L. Hang, L. M. Tolbert, and F. Wang, "Modeling and control of an LCL filter based three-phase active rectifier in grid emulator," in *Proc. IEEE Applied Power Electronics Conference and Exposition*, 2013, pp. 992–998. 26

[45] Y. Ma, L. Yang, J. Wang, F. Wang, and L. M. Tolbert, "Emulating full-converter wind turbine by a single converter in a multiple converter based emulation system," in *Proc. IEEE Applied Power Electronics Conference and Exposition*, 2014, pp. 3042–3047. 27

[46] Y. Ma, L. Yang, F. Wang, and L. M. Tolbert, "Voltage closed-loop virtual synchronous generator control of full converter wind turbine for grid-connected and stand-alone operation," in *Proc. IEEE Applied Power Electronics Conference and Exposition*, 2016, pp. 1261–1266. 27

[47] J. Wang, Y. Ma, L. Yang, L. M. Tolbert, and F. Wang, "Power converter-based three-phase induction motor load emulator," in *Proc. IEEE Applied Power Electronics Conference and Exposition*, 2013, pp. 3270–3274. 27

[48] M. Kesler, E. Ozdemir, M. C. Kisacikoglu, and L. M. Tolbert, "Power converter-based three-phase nonlinear load emulator for a hardware testbed system," *IEEE Transactions on Power Electronics*, vol. 29, no. 11, pp. 5806–5812, 2014. 27

[49] J. Wang, L. Yang, C. Blalock, and L. M. Tolbert, "Flywheel energy storage emulation using reconfigurable hardware test-bed of power converters," in *Proc. Electrical Energy Storage Applications and Technologies Technical Conference*, 2013. 27

[50] B. Liu, S. Zheng, Y. Ma, F. Wang, and L. M. Tolbert, "Control and implementation of converter based AC transmission line emulation," in *Proc. IEEE Applied Power Electronics Conference and Exposition*, 2015, pp. 1807–1814. 27

[51] Y. Ma, L. Yang, F. Wang, and L. M. Tolbert, "Short circuit fault emulation by shunt connected voltage source converter," in *Proc. IEEE Energy Conversion Congress and Exposition*, 2015, pp. 2622–2628. 27

[52] Y. Li, X. Shi, B. Liu, F. Wang, L. M. Tolbert, and W. Lei, "Hardware implementation of a four-terminal HVDC test-bed," in *Proc. IEEE Energy Conversion Congress and Exposition*, 2015, pp. 5363–5370. 27

[53] J. D. Boles, Y. Ma, W. Cao, L. M. Tolbert, and F. Wang, "Battery energy storage emulation in a converter-based power system emulator," in *Proc. IEEE Applied Power Electronics Conference and Exposition*, 2017, pp. 1–8. 28

[54] O. König, C. Hametner, G. Prochart, and S. Jakubek, "Battery emulation for power-HIL using local model networks and robust impedance control," *IEEE Transactions on Industrial Electronics*, vol. 61, no. 2, pp. 943–955, 2014. 29, 30, 43

[55] A. Thanheiser, T. P. Kohler, C. Bertram, and H.-G. Herzog, "Battery emulation considering thermal behavior," in *Proc. IEEE Vehicle Power and Propulsion Conference*, 2011, pp. 1–5. 29, 30

[56] T. Mesbahi, N. Rizoug, P. Bartholomeus, and P. Le Moigne, "Li-ion battery emulator for electric vehicle applications," in *Proc. IEEE Vehicle Power and Propulsion Conference*, 2013, pp. 1–8. 29, 30, 31, 44, 45, 46

[57] M. Michalczuk, B. Ufnalski, L. M. Grzesiak, and P. Rumniak, "Power converter-based electrochemical battery emulator," *Przeglad Elektrotechniczny*, vol. 90, no. 7, pp. 18–22, 2014. 29, 30

[58] H. Dai, X. Zhang, X. Wei, Z. Sun, J. Wang, and F. Hu, "Cell-BMS validation with a hardware-in-the-loop simulation of lithium-ion battery cells for electric vehicles," *International Journal of Electrical Power & Energy Systems*, vol. 52, pp. 174–184, 2013. 29, 30

[59] O. König, G. Gregorčič, and S. Jakubek, "Model predictive control of a DC–DC converter for battery emulation," *Control Engineering Practice*, vol. 21, no. 4, pp. 428–440, 2013. 29, 30, 43

[60] L. Gauchia and J. Sanz, "A per-unit hardware-in-the-loop simulation of a fuel cell/battery hybrid energy system," *IEEE Transactions on Industrial Electronics*, vol. 57, no. 4, pp. 1186–1194, 2010. 29, 30

[61] S. M. Alhejaj and F. M. Gonzalez-Longatt, "Impact of inertia emulation control of grid-scale BESS on power system frequency response," in *Proc. IEEE International Conference for Students on Applied Engineering (ISCAE)*, 2016, pp. 254–258. 31, 59

[62] G. Wang, G. Konstantinou, C. D. Townsend, J. Pou, S. Vazquez, G. D. Demetriades, and V. G. Agelidis, "A review of power electronics for grid connection of utility-scale battery energy storage systems," *IEEE Transactions on Sustainable Energy*, vol. 7, no. 4, pp. 1778–1790, Oct. 2016. 32, 34, 36, 38, 39, 40, 41, 42

[63] E. Chatzinikolaou and D. J. Rogers, "A comparison of grid-connected battery energy storage system designs," *IEEE Transactions on Power Electronics*, vol. PP, no. 99, Nov. 2016. 32, 33, 40

[64] A. Seaman, T.-S. Dao, and J. McPhee, "A survey of mathematics-based equivalent-circuit and electrochemical battery models for hybrid and electric vehicle simulation," *Journal of Power Sources*, vol. 256, pp. 410–423, June 2014. 42, 43, 44, 45, 50, 51

[65] K. Sun and Q. Shu, "Overview of the types of battery models," in *Proc. IEEE Chinese Control Conference*, 2011, pp. 3644–3648. 42, 43, 44, 45, 46

[66] M. Chen and G. A. Rincon-Mora, "Accurate electrical battery model capable of predicting runtime and IV performance," *IEEE Transactions on Energy Conversion*, vol. 21, no. 2, pp. 504–511, June 2006. 42, 43, 45, 46, 50, 51

[67] R. C. Kroeze and P. T. Krein, "Electrical battery model for use in dynamic electric vehicle simulations," in *Proc. IEEE Power Electronics Specialists Conference*, 2008, pp. 1336–1342. 42, 43, 44, 45, 46, 50, 51

[68] Y. Cao, R. C. Kroeze, and P. T. Krein, "Multi-timescale parametric electrical battery model for use in dynamic electric vehicle simulations," *IEEE Transactions on Transportation Electrification*, vol. 2, no. 4, pp. 432–442, Dec. 2016. 42, 43, 44, 45, 46, 50

[69] B. Xu, A. Oudalov, J. Poland, A. Ulbig, and G. Andersson, "BESS control strategies for participating in grid frequency regulation," in *IFAC World Congress Proceedings Volumes*, vol. 47, no. 3. Elsevier, 2014, pp. 4024–4029. 43, 57, 58

[70] H. Chan, "A new battery model for use with battery energy storage systems and electric vehicles power systems," in *Proc. IEEE Power Engineering Society Winter Meeting*, vol. 1, 2000, pp. 470–475. 44

[71] J. Wang, K. Zou, C. Chen, and L. Chen, "A high frequency battery model for current ripple analysis," in *Proc. IEEE Applied Power Electronics Conference and Exposition*, 2010, pp. 676–680. 46

[72] C. Chenghui, D. Dong, G. Jingtian, L. Zhiyu, and Z. Hua, "Battery-charging model to study transient dynamics of battery at high frequency," in *Proc. IEEE Region 10 Conference on Computers, Communications, Control and Power Engineering*, vol. 3, 2002, pp. 1843–1846. 46

[73] O. Tremblay, L.-A. Dessaint, and A.-I. Dekkiche, "A generic battery model for the dynamic simulation of hybrid electric vehicles," in *Proc. IEEE Vehicle Power and Propulsion Conference*, 2007, pp. 284–289. 47, 48, 49

[74] O. Tremblay and L.-A. Dessaint, "Experimental validation of a battery dynamic model for EV applications," *World Electric Vehicle Journal*, vol. 3, no. 1, pp. 1–10, May 2009. 47, 48, 49, 50, 65, 85

[75] C. M. Shepherd, "Design of primary and secondary cells II. an equation describing battery discharge," *Journal of the Electrochemical Society*, vol. 112, no. 7, pp. 657–664, 1965. 48

[76] Battery. The MathWorks, Inc. [Online]. Available: https://www.mathworks.com/help/physmod/sps/powersys/ref/battery.html 50

[77] X. Li, Y. Huang, J. Huang, S. Tan, M. Wang, T. Xu, and X. Cheng, "Modeling and control strategy of battery energy storage system for primary frequency regulation," in *Proc. IEEE International Conference on Power System Technology*, 2014, pp. 543–549. 50, 51, 57

[78] M. H. Li, T. Funaki, and T. Hikihara, "A study of output terminal voltage modeling for redox flow battery based on charge and discharge experiments," in *Proc. IEEE Power Conversion Conference - Nagoya*, 2007, pp. 221–225. 51

[79] X. Qiu, T. A. Nguyen, J. D. Guggenberger, M. L. Crow, and A. C. Elmore, "A field validated model of a vanadium redox flow battery for microgrids," *IEEE Transactions on Smart Grid*, vol. 5, no. 4, pp. 1592–1601, July 2014. 51

[80] M. Mohamed, H. Ahmad, M. A. Seman, S. Razali, and M. Najib, "Electrical circuit model of a vanadium redox flow battery using extended kalman filter," *Journal of Power Sources*, vol. 239, pp. 284–293, Oct. 2013. 51

[81] R. W. Erickson and D. Maksimovic, *Fundamentals of Power Electronics*. Springer Science & Business Media, 2007. 53, 54

[82] J. Servotte, E. Acha, and L. M. Castro, "Smart frequency control in power transmission systems using a BESS," in *IEEE Innovative Smart Grid Technologies-Asia (ISGT ASIA)*, 2015, pp. 1–7. 56, 57, 59

[83] N. Mahmud and A. Zahedi, "Review of control strategies for voltage regulation of the smart distribution network with high penetration of renewable distributed generation," *Renewable and Sustainable Energy Reviews*, vol. 64, pp. 582–595, Oct. 2016. 60

[84] T. Xu and P. Taylor, "Voltage control techniques for electrical distribution networks including distributed generation," in *Proc. IFAC World Congress Proceedings Volumes*, vol. 41, no. 2. Elsevier, 2008, pp. 11 967–11 971. 60

[85] Y. Yang, H. Li, A. Aichhorn, J. Zheng, and M. Greenleaf, "Sizing strategy of distributed battery storage system with high penetration of photovoltaic for voltage regulation and peak load shaving," *IEEE Transactions on Smart Grid*, vol. 5, no. 2, pp. 982–991, March 2014. 60

Vita

Jessica D. Boles was born in Murfreesboro, TN, where she graduated from Siegel High School in 2011. She began pursuing a degree in electrical engineering at the University of Tennessee (UT) the following fall and completed her B.S. as the College of Engineering Top Graduate in December 2015. As a Master's student, Jessica is now a Bodenheimer Fellow and works through the Center for Ultra-Wide-Area Resilient Electric Energy Transmission Networks (CURENT) as a Graduate Research Assistant. She has been involved with CURENT since her freshman year through various research and leadership opportunities, and her graduate work focuses on the development of a battery energy storage emulator for CURENT's converter-based power system testbed. Jessica has also conducted research on wireless charging for UAVs at the Oak Ridge National Laboratory, and she served as the electrical engineering team leader for UTs EcoCAR 3 competition team as her senior design project. Outside of power, Jessica has devoted herself to recruiting, mentoring, and retaining women in the engineering field as the former president of an organization named Systers in her department and by coordinating UT's first women in engineering conference, WomEngineers Day. Jessica looks forward to a career in research and will begin work towards a PhD in the fall of 2017.